Ligand-Coupled Conformational Changes in a Cyclic Nucleotide-Gated Ion Channel Revealed by Time-Resolved Transition Metal Ion FRET

Pierce Eggan

A dissertation
submitted in partial fulfillment of the
requirements for the degree of

Doctor of Philosophy

University of Washington
2025

Reading Committee:
William N. Zagotta, Chair
Abhinav Nath
Charles L. Asbury

Program Authorized to Offer Degree:
Molecular and Cellular Biology

University of Washington

Abstract

Ligand-Coupled Conformational Changes in a Cyclic Nucleotide-Gated Ion Channel Revealed by Time-Resolved Transition Metal Ion FRET

Pierce Eggan

Chair of the Supervisory Committee:

William N. Zagotta

Department of Physiology and Biophysics

The cyclic nucleotide binding domain (CNBD) channels are an important family of ion channels that regulate various physiological roles including sensory perception, cardiac activity, and neuronal cellular excitability. These channels are regulated by the binding of cyclic nucleotides, which causes conformational changes throughout the protein structure that ultimately open the channel's pore. However, the details of this allosteric process, particularly the heterogeneity of conformational states and the energetic coupling between domains, remain poorly understood.

This body of work utilizes time-resolved transition metal ion resonance energy transfer (tmFRET) techniques to investigate the conformational changes and energetics underlying ligand binding in a prokaryotic CNBD channel SthK. Time-resolved tmFRET involves the measurement of fluorescence lifetimes to determine the distance between a donor fluorophore and metal ion acceptor, enabling the detection of a protein's structural dynamics. The methodology was first validated here using the model protein maltose-binding protein (MBP) and then applied to SthK in first a C-terminal fragment ($SthK_{Cterm}$) and subsequently a full-length form ($SthK_{Full}$).

In $SthK_{Cterm}$ we have been able to make measurements of intramolecular distance distributions within SthK's CNBD to monitor the conformational changes of this domain when ligand binds.

These probability distributions were used to calculate the changes in Gibbs free energy (ΔG) for both full agonist cAMP and partial agonist cGMP, showing that cAMP drives the conformational transition more than cGMP. In measurements of $SthK_{Full}$, we have been able to compare distance distributions to those made in $SthK_{Cterm}$ and revealed the influence of interdomain coupling, with the presence of the pore domain enhancing the CNBD's conformational transition. This work highlights the use of time-resolved tmFRET for characterizing the conformational dynamics and energetics of allosteric proteins in general and provides valuable insights into the ligand-mediated allosteric mechanism of SthK specifically.

Acknowledgements

I would like to give special thanks to everyone who has helped me throughout the course of this research and in making this work possible. This investigation was carried out in the lab of William N. Zagotta, who has been an incredible mentor- not just in science, but in outlooks on life as well. His guidance has greatly shaped my scientific understanding, and his fostering of a supportive, enjoyable lab environment made this work a truly rewarding experience. I'm equally grateful to Dr. Sharona Gordon, who has been a profound influence on my growth, offering extensive mentorship in science, and personal development. Both of their support has been invaluable.

Special thanks also go to Drs. Chip Asbury, Abhinav Nath, and Frank DiMaio for their intellectual contributions and project guidance. I couldn't have completed this work without the support of all current and past Zagotta and Gordon lab members, including Drs. Galen Flynn, Eric Evans, Gucan Dai, James Morgan, Jill Jenson, Moshe Gordon, Demian Leibermann, Emerson Carmona, and Duk-Su Koh, as well as graduate students Jesse Huang and Charlie DeFreest, and our great lab manager Ken Garbutt. Your insights, guidance, and camaraderie have been tremendous and I greatly appreciate the supportive and fun lab environment that you've created.

I owe a huge thanks to my parents, Madeline and Peter Eggan, who have always been incredibly encouraging of my academic endeavors, pushing me to get where I am today, and always being patient ears for listening. Thanks to my brother Elliott, who I have always looked up to as a source of academic inspiration. None of this would have been possible without the support and encouragement of my partner, Dr. Samantha Schuster. Thank you for the amazingly insightful contributions to my science, your willingness to read my writing, and the countless adventures we've been on along the way. Finally, I'm very grateful to the MCB program for providing resources, financial support, and overall guidance through the process as well as the amazing colleagues and friends in the MCB program.

Table of Contents

Abstract 3
Acknowledgements 5
Table of Contents 6
Chapter1: Introduction 8
- **Cyclic Nucleotide Binding Domain channels** 9
- **Prokaryotic CNBD Channel SthK** 10
- **Protein Allostery and Conformational Energetics** 12
- **Transition Metal Ion Fluorescence Resonance Energy Transfer (tmFRET)** 14
- **Time Resolved FRET with Fluorescence Lifetimes** 15
- **Dissertation Overview** 17
- **References** 18

Chapter 2: Measuring Conformational Equilibria in Allosteric Proteins with Time-Resolved tmFRET 21
- **Abstract** 22
- **Introduction** 23
- **Materials and Methods** 25
- **Results** 30
- **Discussion** 42
- **References** 44
- **Supporting Material** 48
- **Supplemental Figures** 52

Chapter 3: Ligand-Coupled Conformational Changes in the Isolated C-terminal Domains of SthK 57
- **Abstract** 58
- **Introduction** 59
- **Results** 63
- **Discussion** 79
- **Materials and Methods** 82
- **References** 89
- **Supplemental Figures** 92

Chapter 4: Domain Coupling in Allosteric Regulation of SthK Measured Using Time-Resolved Transition Metal Ion FRET 97

Abstract **98**
Introduction **99**
Results **103**
Discussion **118**
Materials and Methods **121**
References **130**
Supplemental Figures **132**
Chapter 5: Conclusions **135**
References **140**

Chapter1: Introduction

Ion channels are membrane proteins that control the selective transport of ions such as Na^+, K^+, Ca^{2+}, and Cl^- across biological membranes (1, 2). They play critical roles in cellular processes including electrical excitability, signaling, and maintaining homeostasis. These dynamic molecular machines are composed of specialized domains that respond to various environmental signals, such as changes in membrane voltage, ligand binding, or mechanical forces. These external signals regulate the opening and closing of a central pore, which serves as a selective pathway for rapid ionic flow. This structural rearrangement and ionic flow not only alter the membrane's electrochemical gradient, but also trigger a range of signaling events and secondary protein interactions.

Despite their importance, the mechanisms by which ion channels sense environmental changes and undergo structural rearrangements to open, called gating, remain incompletely understood. Historically, research on ion channels has approached questions of gating from two primary perspectives: functional measurements, such as monitoring ion conductance through electrophysiology, and structural studies, such as resolving high-resolution channel structures. While both of these approaches have provided valuable insights into opening mechanisms, there is a growing need to integrate these strategies to achieve a more comprehensive understanding of how these proteins are regulated. Protein dynamics, encapsulating not only the heterogeneity and changes in molecular structures, but also the energetics that underlie different protein states, can bridge these functional and molecular perspectives.

This introduction will focus on what is known about the cyclic nucleotide-binding domain (CNBD) family of ion channels, an important family of ion channels in human physiology, which are significantly regulated by ligand binding. Subsequently, it will review the progress made in understanding their gating mechanisms and discuss how fluorescence-based tools have been applied to investigate their conformational heterogeneity and energetics. Lastly, it will serve to introduce the latest work that we have done in measuring protein dynamics of ligand activation in CNBD channels using these fluorescence tools. This work overall helps to shed light on the molecular mechanisms of CNBD channel gating and function.

Cyclic Nucleotide Binding Domain channels

Cyclic nucleotide binding domain (CNBD) channels are part of the voltage-gated K^+ ion channel superfamily, playing pivotal roles across sensory perception, cardiac activity, signal transduction, and cellular excitability in human physiology (3–5). The CNBD family includes three subgroups of channels: 1) cyclic nucleotide-gated (CNG) channels, 2) hyperpolarization-activated cyclic nucleotide-gated (HCN) channels and 3) the ether-á-gogo-type (KCNH) ion channels. These subgroups have unique gating properties, respond differently to changes in their local environment, and each play key physiological roles. For example, CNG channels are responsible for both visual and olfactory signal transduction, dramatically depolarizing rod and cone cells or olfactory sensory neurons in response to local changes in cyclic nucleotide concentration (3). While CNG channels are not voltage sensitive, HCN channels respond to hyperpolarizing membrane potentials and are known for spontaneous and rhythmic firing patterns in cells. They are found in the sinoatrial node where they regulate the pacemaker activity of the heart and are also important for regulating neuronal excitability throughout the central and peripheral nervous system. KCNH are not ligand activated and are activated by depolarizing potentials. These channels are best known for their role in repolarizing the cardiac action potential and regulating firing patterns throughout the brain (6, 7). Given their functional significance, pharmacological potential, susceptibility to off-target drug effects, and associations with disease-related mutations, understanding the molecular mechanisms of gating in CNBD channels is crucial.

Over the past decade, numerous high-resolution structures have added atomic-level spatial information for these channels, have revealed significant aspects of these channels' possible conformations, and have highlighted remarkable architectural similarities across the channels (3, 5, 8–11). Despite their diverse physiological roles, CNBD channels all possess a shared core tetrameric structure with four identical or similar subunits surrounding a central ion-conducting pore. Each subunit contains three regions: an N-terminal region, a transmembrane region with a voltage-sensor and pore domain, and a cytosolic C-terminal region that consist of a CNBD plus a C-linker connecting the CNBD to the pore (Figure 1A).

These channels are activated when cyclic nucleotides, which are important second messengers that include cyclic adenosine monophosphate (cAMP) and cyclic guanosine

monophosphate (cGMP), bind to the CNBD (3). Cyclic nucleotide binding to the CNBD induces conformational changes throughout the protein structure to ultimately open the pore. KCNH channels are the exception, where instead of a CNBD domain there is a CNBD homology domain (CNBHD) in which cyclic nucleotide binding is rendered obsolete due to part of its protein sequence acting as an 'intrinsic ligand' occupying the cyclic nucleotide binding pocket (6). Ultimately, the distal cytoplasmic CNBD region of the CNG and HCN channels cause various conformational and energetic changes to the channel structures to open the pore when cyclic nucleotides bind. This activity at a distance is commonly described as allostery where different parts of a protein are thermodynamically coupled, and the free-energy changes are interconnected.

This ligand-induced allosteric opening in CNBD channels is still poorly understood, and questions remain about the structural and energetic changes that occur in these proteins during this allosteric regulation. In particular, what are the energetics of the conformational changes in individual protein domains, how are these conformational changes coupled within and between subunits, and how do these processes differ for full and partial agonists? A deeper understanding of the energetics that describe this allosteric mechanism will allow for better understanding of how mutations may affect functionality, how other sensing domains or modulators (such as voltage regulation) modulates functionality, and how drugs may alter energetics to promote or inhibit coupled responses.

Prokaryotic CNBD Channel SthK

SthK is a prokaryotic ion channel belonging to the CNBD family, found from the bacteria *spirochete thermophilia*. Like other CNBD channels, it has the same structural architecture (Figure 1A) and functions through ligand-induced allosteric regulation, where binding of cyclic nucleotides to the intracellular CNBD triggers conformational changes that open the ion-conducting pore (10, 12–14). Binding of cyclic adenosine monophosphate (cAMP) strongly promotes opening of the channel, whereas cyclic guanosine monophosphate (cGMP) is a weak partial agonist and only minimally opens the channel (15). The channel is minimally voltage sensitive and it has been well characterized by macroscopic and single channel electrophysiology as well as flux assays (12, 15, 16). Structures of SthK have been obtained from both cryoEM and

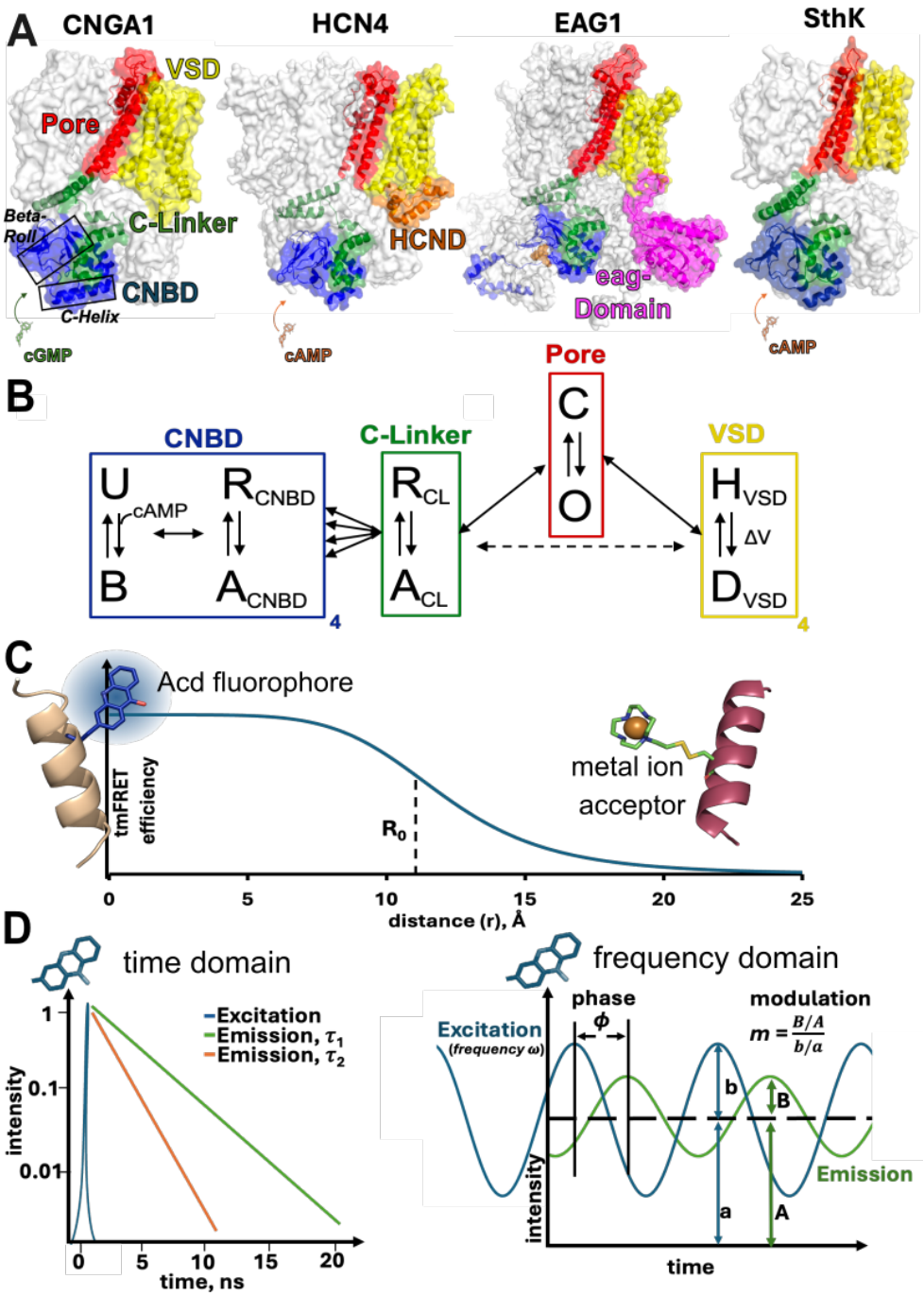

Figure 1. CNBD channels structures and methodologies for uncovering allosteric mechanisms. **(A)** Structures from left to right of human CNGA1 (PDB: 7lft), rabbit HCN4 (PDB: 7np3), EAG1 (PDB: 5k7l) and SthK (PDB: 6cjq), colored with common domains: cyclic nucleotide binding domain (CNBD, blue), C-Linker (green), Pore (red) and Voltage Sensor Domain (VSD, yellow). **(B)** Modular gating scheme for a CNBD channel with domain modules and verticle arrows for conformational transitions within domains. Modules are coupled together (horizontal arrows). **(C)** Depiction of tmFRET, with unnatural amino acid fluorophore, Acd, a metal ion acceptor molecule, Cu-TETAC, and the Förster relationship curve. **(D)** Time domain measurements of lifetimes (on the left), showing an excitation pulse (in blue) and log scale histogram of photon arrival times for two different single exponential decays (green and orange). Frequency domain showing sinusoidally varying excitation pulse in blue and corresponding emission with measures of phase delay and modulation ratio.

X-ray crystallography showing conformational changes under a range of experimental conditions, including bound to cAMP or cGMP (10, 13, 16, 17).

SthK stands out for its simple structure, accessible functional characteristics, and ease of protein expression in *E.coli*, which allows it to serve as a model system for understanding the fundamental mechanisms of ligand binding in CNBD channels and bridging structural and functional insights. Our lab has laid important groundwork for utilizing SthK as a model system by creating a cysteine-less version of the protein (cfSthK), for techniques requiring site-specific cysteine reaction chemistries, and by optimizing expression conditions in *E.coli* with an adenylyl-cyclase knock-out strain that produces robust quantities of SthK (15). Therefore, SthK offers the great potential for successfully characterizing the complete allosteric mechanism of pore opening within a single CNBD channel protein. The work described in this dissertation utilizes SthK to better understand how ligand binding translates into pore opening in CNBD channels in general.

Protein Allostery and Conformational Energetics

To describe protein allostery, the regulation of function through conformational changes distant from the active site, numerous quantitative models have been developed to describe the complex energetics involved in various proteins (18). Historically, two primary models have dominated from a functional perspective: the *induced fit* Koshland-Nemethy-Filmer, (KNF) model and the *concerted* Monod-Wyman-Changeux (MWC) model (19, 20). While these two phenomenological models effectively account for the energetics of ligand binding in many cases, they are inherently descriptive in their states and fail to describe the underlying mechanism of how allostery works on a molecular level. On the other hand, purely structural models that emphasize specific protein interactions and only structural rearrangements fail to address the importance of intrinsic heterogeneity of proteins both within and between structural states. They furthermore do not provide a full characterization of the number of states and the allowed transitions between them in the allosteric mechanism. The limitations from these two different perspectives highlights the need for frameworks that unite energetic and specific protein structures to fully elucidate allosteric mechanisms, applied generally to any protein and specifically to the changes in CNBD channels.

The *modular gating scheme*, proposed by Horrigan and Aldrich in the context of ion channels and generalized by Motlagh et al. as the *ensemble model*, offers a powerful framework for achieving this structure-function integration for allostery (18, 21, 22). This approach views allostery through a modular lens, where individual domains or functional units are treated as distinct energetic modules. Each module undergoes local conformational changes influenced by ligand binding, and these changes are coupled to neighboring modules through defined energetic relationships. This coupling allows for coordinated conformational transitions across multiple different domains, ultimately driving the allosteric process across the entire protein. A protein's energetic landscape can thus be illustrated by the number of modules involved in the allosteric transition, allowing for flexibility to include as many or as few modules as needed. This could be as simple as only two modules in some proteins or even down to the residue level in others, making this approach broadly applicable across proteins. Importantly, this framework accounts for energetic changes while retaining the structural description of proteins, providing a comprehensive model for understanding how specific residues, domains, and energetic couplings contribute to allosteric regulation. With this approach, we can begin to quantitatively dissect different structural contributions to ligand-dependent gating and to better understand the allosteric regulation in CNBD channels as a whole.

A proposed modular gating scheme is suggested for a CNBD channel, such as SthK, in Figure 1B (5). In SthK, it is thought that the ligand-induced conformational changes in the CNBD are energetically coupled to the transitions in the C-linker, which is subsequently coupled to pore opening, as seen by the separate module boxes and coupling arrows between them in the diagram. Within each of these domain modules, a simple four-state model can be used to provide a foundational framework, for describing the conformational states and energetics of individual domains. For example, the CNBD can be in either a resting or active conformational state both in the presence and absence of bound ligand. The transitions between these states are governed by equilibrium constants, with the presence of bound agonist shifting the equilibrium to favor the active state. The ultimate coupling of the CNBD to the pore, means that conformational changes in the CNBD can shift the equilibrium in the pore and likewise, the conformational energetics of the pore shifts the equilibrium of the conformational state in the CNBD. Similarly, voltage modulation in the voltage sensor domain would also be coupled with the pore, and potentially with the C-linker, to regulate channel opening. The equilibrium constants within domains enable

calculations of the Gibbs free energy changes (ΔG) and differences in energy change (ΔΔG) associated with ligand binding and conformational transitions. With this theoretical framework and a technique capable of measuring the proportion of molecules within relative conformational states of multiple different domains, a more complete allosteric model can be built for CNBD ligand gating.

Transition Metal Ion Fluorescence Resonance Energy Transfer (tmFRET)

One of the most powerful biophysical methods for making both structural and dynamic measurements within and between proteins is fluorescence resonance energy transfer (FRET) (23). In FRET experiments, a donor fluorophore is excited to a higher energetic level and in this state transfers some of its energy to an acceptor molecule. This relationship is defined by the Förster equation of: $E = \frac{{R_0}^6}{r^6 + {R_0}^6}$ where E is the FRET efficiency, R_0 is the distance at 50% FRET efficiency and r is the distance between donor and acceptor molecules (24). Due to the steep (r^6) distance dependence of the energy transferred, it can be used as a precise and high-resolution molecular ruler between the donor and acceptor molecules. Transition metal ion FRET is an adaptation of FRET in which a donor fluorophore is paired with a transition metal ion, such as Cu^{2+}, Fe^{2+}, or Ru^{2+}, as an acceptor molecule (Figure 1C) (25–28). Like fluorescence-based acceptor molecules, these metal ions will all accept energy transferred from the donor fluorophore and thus decrease the fluorescence intensity of the donor. Donor-acceptor pairs can then be incorporated in a protein at different residue positions close to the protein backbone to measure the dynamics of intramolecular distances in the protein (29–32).

Transition metal ion FRET has several advantages over classical two fluorophore FRET including: 1) multiple transition dipoles allowing for less dependence on donor-acceptor dipole orientations, 2) generally shorter R_0s for measuring shorter distances with steeper distance dependence, 3) different metals can be used with different absorptions to produce different R_0s, 4) metals can often be reversibly bound as acceptors, and 5) donor-acceptor labels can be incorporated closer to the backbone structure of proteins (26). On this last point, an often-overlooked disadvantage of traditional FRET techniques is the use of large fluorophores with long linkers that when attached to proteins do not accurately report the conformational movement of the protein. As a result, minimizing fluorophore size and proximity to the protein

backbone is important, and the tmFRET method that has gained the most traction is incorporating the donor fluorophore directly into the protein structure using genetic code expansion. Fluorophores, including Acridon-2-ylalanine (Acd) or L-ANAP, can be introduced as unnatural amino acids into the residue positions of interest as an amber (TAG) stop codon along with the specific tRNA and tRNA synthetase for incorporating the amino acid into the growing protein structure (29, 31–35). Likewise, a metal ion can be incorporated into a protein structure with a cysteine-reactive metal chelators, like TETAC or phenanthroline maleimide, or with an engineered di-histidine motif. With these advances to traditional FRET, tmFRET is well suited to make structural characterizations of protein conformational transitions.

In the subsequent chapters, we utilize tmFRET tools in both steady-state fluorescence intensity measurements and in time-resolved measurements with fluorescence lifetimes. Whereas steady-state FRET measurements make only a single average distance of all molecules in solution, time-resolved FRET can give information about the number of molecules at one distance relative to another.

Time Resolved FRET with Fluorescence Lifetimes

Time-resolved tmFRET measures changes in the fluorescence lifetime of a donor fluorophore to determine FRET efficiencies and molecular distances between donor and acceptor molecules. The fluorescence lifetime, generally on the order of nanoseconds, is the average time a fluorophore spends in its excited state before it returns to the ground state by emitting a photon (23). While photon emission from a fluorophore is a stochastic process, meaning that individual photons are released at different times rather than all at once, the fluorescence lifetime represents the average time for photons to be released. In the simplest case, the photon emission from the excited state is a single exponential decay rate, with $\frac{1}{e}$ photons being released by the lifetime (τ), although the distribution of excited state decay rates could be more complicated as double or multi-exponentials. In the presence of an acceptor molecule, the donor fluorophore spends less time in the excited state, reducing its apparent fluorescence lifetime, as energy is transferred to the acceptor. The distribution of excited-state lifetimes is a weighted average of all molecules in solution and thus the change in lifetime due to FRET can be used to determine the relative proportion of molecules with one lifetime relative to another lifetime (31, 36–38). Thus, unlike in

intensity-based FRET experiments, time-resolved measurements of FRET can give nanosecond snapshots of the donor fluorophore, and the distribution of FRET efficiencies in a sample of molecules. This enables the resolution of heterogeneity in donor-acceptor distances, where lifetime data can be fit to distributions of distances that account for the measured FRET between donor and acceptor molecules (36, 38). When donor and acceptor molecules are incorporated into a protein, this distance distribution therefore describes the heterogeneity of the protein itself, both the heterogeneity within protein conformational states and between conformational states. As mentioned earlier, the proportion of molecules between states allows for the calculation of free energy differences (ΔG) between states.

Fluorescence lifetimes can be assessed using either time-domain or frequency-domain methods (Figure 1D) (23). In the time domain, photon arrival times are measured from a fluorophore sample relative to an extremely short excitation pulse by utilizing time-correlated single photon counting (TCSPC). To ensure that individual photons and their arrival times can be detected, measurement conditions in TCSPC are adjusted to receive photons from, on average, less than one fluorophore at a time in the sample (a photon from ~1:100 laser pulses). Over thousands of repetitions, these individual photon arrival times can be tallied and used to build a histogram of photon arrival times that describe the distribution of photon emission rates leaving the excited state. Comparatively, in the frequency domain, lifetimes are measured by quantifying the phase shift (phase delay, ϕ) and decrease in amplitude of response (modulation ratio, m) of the donor's emission as a function of the modulation frequency of a sinusoidally-varying excitation light (23, 39). These phase and modulation values are dependent on the frequency of the excitation light and thus when measured across a range of excitation frequencies, the complex intensity decay rates from the fluorophore's excited state can be obtained. Both methods for quantifying lifetimes are used in this work and have been described more in depth in other reviews (23, 39–41) and in subsequent chapters, starting with frequency domain measurements in chapters 2 and 3 and moving to TCSPC measurements in chapter 4. The FRET model used to obtain distance distributions from fluorescence lifetime data from each method is discussed further, for frequency domain in chapter 2 and for time domain in chapter 4.

Dissertation Overview

In the following chapters, I will describe the progression of our use of time-resolved tmFRET to explore conformational dynamics of allosteric proteins. First, in Chapter 2, we tested the principle of this technique using maltose-binding protein (MBP) as a simple model system and as a proof of principle with the acceptor metal ion complexes $[Ru(bpy)_2phenM]^{2+}$ and $[Fe(phenM)_3]^{2+}$. Next, in Chapter 3, we applied the same approach to CNBD channels, focusing on detecting the conformational change associated with the CNBD's C-helix relative to the β-roll in the absence and presence of ligand. To simplify our system, we first measured the distance distributions of this transition in a soluble fragment of SthK with only the C-terminal domains. Lastly, in Chapter 4, we moved to the full-length SthK channel, making distance distribution measurements of the conformational energetics and ultimately comparing these to the previous measurements in the isolated C-terminal fragment. We have been able to make conclusions about the differences between full and partial agonists of these channels, as well as regarding the effect of coupling on the CNBD energetics when attached to the pore domain. These results provide a more complete understanding of the structural and energetic changes in the CNBD with ligand binding.

References

1. B. Hille, *Ion channels of excitable membranes*, 3rd ed. (Sunderland (Mass.) : Sinauer associates, 2001).
2. J. Zheng, M. C. Trudeau, *Handbook of ion channels* , 1st ed. (CRC Press, 2015).
3. K. B. Craven, W. N. Zagotta, CNG and HCN channels: Two peas, one pod. *Annu Rev Physiol* **68**, 375–401 (2006).
4. K. Matulef, W. N. Zagotta, Cyclic Nucleotide-Gated Ion Channels. *Annu Rev Cell Dev Biol* **19**, 23–44 (2003).
5. Z. M. James, W. N. Zagotta, Structural insights into the mechanisms of CNBD channel function. *Journal of General Physiology* **150**, 225–244 (2018).
6. J. H. Morais-Cabral, G. A. Robertson, The Enigmatic Cytoplasmic Regions of KCNH Channels. *J Mol Biol* **427**, 67–76 (2015).
7. B. Ganetzky, G. A. Robertson, G. F. Wilson, M. C. Trudeau, S. A. Titus, The eag family of K+ channels in Drosophila and mammals. *Ann N Y Acad Sci* **868**, 356–369 (1999).
8. J. R. Whicher, R. MacKinnon, Structure of the voltage-gated K+ channel Eag1 reveals an alternative voltage sensing mechanism. *Science (1979)* **353**, 664–669 (2016).
9. J. Xue, Y. Han, W. Zeng, Y. Wang, Y. Jiang, Structural mechanisms of gating and selectivity of human rod CNGA1 channel. *Neuron* **109**, 1302-1313.e4 (2021).
10. X. Gao, *et al.*, Gating intermediates reveal inhibitory role of the voltage sensor in a cyclic nucleotide-modulated ion channel. *Nat Commun* **13** (2022).
11. A. Saponaro, *et al.*, Gating movements and ion permeation in HCN4 pacemaker channels. *Mol Cell* **81**, 2929-2943.e6 (2021).
12. M. Brams, J. Kusch, R. Spurny, K. Benndorf, C. Ulens, Family of prokaryote cyclic nucleotide-modulated ion channels. *Proc Natl Acad Sci U S A* **111**, 7855–7860 (2014).
13. D. Kesters, *et al.*, Structure of the SthK carboxy-terminal region reveals a gating mechanism for cyclic nucleotide-modulated ion channels. *PLoS One* **10**, 1–12 (2015).
14. E. G. B. Evans, J. L. W. Morgan, F. DiMaio, W. N. Zagotta, S. Stoll, Allosteric conformational change of a cyclic nucleotide-gated ion channel revealed by DEER spectroscopy. *Proc Natl Acad Sci U S A* **117**, 10839–10847 (2020).
15. J. L. W. Morgan, E. G. B. Evans, W. N. Zagotta, Functional characterization and optimization of a bacterial cyclic nucleotide-gated channel. *Journal of Biological Chemistry* **294**, 7503–7515 (2019).
16. P. A. M. Schmidpeter, X. Gao, V. Uphadyay, J. Rheinberger, C. M. Nimigean, Ligand binding and activation properties of the purified bacterial cyclic nucleotide-gated channel SthK. *Journal of General Physiology* **150**, 821–834 (2018).
17. P. A. M. Schmidpeter, J. Rheinberger, C. M. Nimigean, Prolyl isomerization controls activation kinetics of a cyclic nucleotide-gated ion channel. *Nat Commun* **11**, 1–16 (2020).
18. H. N. Motlagh, J. O. Wrabl, J. Li, V. J. Hilser, The ensemble nature of allostery. *Nature* **508**, 331–339 (2014).
19. J. Monod, J. Wyman, J.-P. Changeux, On the nature of allosteric transitions: A plausible model. *J Mol Biol* **12**, 88–118 (1965).
20. D. E. Jr. Koshland, G. Némethy, D. Filmer, Comparison of Experimental Binding Data and Theoretical Models in Proteins Containing Subunits*. *Biochemistry* **5**, 365–385 (1966).

21. F. T. Horrigan, R. W. Aldrich, Coupling between voltage sensor activation, Ca2+ binding and channel opening in large conductance (BK) potassium channels. *J Gen Physiol* **120**, 267–305 (2002).
22. V. J. Hilser, J. O. Wrabl, H. N. Motlagh, Structural and energetic basis of allostery. *Annu Rev Biophys* **41**, 585–609 (2012).
23. J. R. Lakowicz, *Principles of fluorescence spectroscopy* (2006).
24. L. Stryer, R. P. Haugland, Energy transfer: a spectroscopic ruler. *Proc Natl Acad Sci U S A* **58**, 719–726 (1967).
25. J. W. Taraska, M. C. Puljung, W. N. Zagotta, Short-distance probes for protein backbone structure based on energy transfer between bimane and transition metal ions. *Proc Natl Acad Sci U S A* **106**, 16227–16232 (2009).
26. S. E. Gordon, E. N. Senning, T. K. Aman, W. N. Zagotta, Transition metal ion FRET to measure short-range distances at the intracellular surface of the plasma membrane. *Journal of General Physiology* **147**, 189–200 (2016).
27. J. W. Taraska, M. C. Puljung, N. B. Olivier, G. E. Flynn, W. N. Zagotta, Mapping the structure and conformational movements of proteins with transition metal ion FRET. *Nat Methods* **6**, 532–537 (2009).
28. S. E. Gordon, *et al.*, Long-distance tmFRET using bipyridyl- and phenanthroline-based ligands. *Biophys J* 2023.10.09.561591 (2024). https://doi.org/10.1016/j.bpj.2024.01.034.
29. G. Dai, W. N. Zagotta, Molecular mechanism of voltage- dependent potentiation of KCNH potassium channels. *Elife* **6**, 1–18 (2017).
30. G. Dai, T. K. Aman, F. DiMaio, W. N. Zagotta, The HCN channel voltage sensor undergoes a large downward motion during hyperpolarization. *Nat Struct Mol Biol* **26**, 686–694 (2019).
31. W. N. Zagotta, *et al.*, An improved fluorescent noncanonical amino acid for measuring conformational distributions using time-resolved transition metal ion FRET. *Elife* **10** (2021).
32. C. M. Jones, *et al.*, Genetic Encoding of a Highly Photostable, Long Lifetime Fluorescent Amino Acid for Imaging in Mammalian Cells. *bioRxiv* 2021.04.05.438526 (2021). https://doi.org/10.1101/2021.04.05.438526.
33. G. Dai, T. K. Aman, F. DiMaio, W. N. Zagotta, Electromechanical coupling mechanism for activation and inactivation of an HCN channel. *Nat Commun* **12** (2021).
34. C. M. Jones, Y. Venkatesh, E. J. Petersson, Protein labeling for FRET with methoxycoumarin and acridonylalanine. *Methods Enzymol* **639**, 37–69 (2020).
35. I. Sungwienwong, *et al.*, Improving the fluorescent probe acridonylalanine through a combination of theory and experiment. *J Phys Org Chem* **31**, 1–18 (2018).
36. E. Haas, M. Wilchek, E. Katchalski-Katzir, I. Z. Steinberg, Distribution of end-to-end distances of oligopeptides in solution as estimated by energy transfer. *Proc Natl Acad Sci U S A* **72**, 1807–1811 (1975).
37. A. Grinvald, E. Haas, I. Z. Steinberg, Evaluation of the Distribution of Distances Between Energy Donors and Acceptors by Fluorescence Decay. *Proceedings of the National Academy of Sciences* **69**, 2273–2277 (1972).
38. W. N. Zagotta, *et al.*, Measuring conformational equilibria in allosteric proteins with time-resolved tmFRET. *Biophys J* 2023.10.09.561594 (2024). https://doi.org/10.1016/j.bpj.2024.01.033.

39. L. Malacrida, S. Ranjit, D. M. Jameson, E. Gratton, The Phasor Plot: A Universal Circle to Advance Fluorescence Lifetime Analysis and Interpretation. *Annu Rev Biophys* **50**, 575–593 (2021).
40. S. Liao, Y. Sun, U. Coskun, FLIM Analysis using the Phasor Plots. *ISS Technical Note* 1–13 (2014).
41. M. Y. Berezin, S. Achilefu, Fluorescence lifetime measurements and biological imaging. *Chem Rev* **110**, 2641–2684 (2010).

Chapter 2: Measuring Conformational Equilibria in Allosteric Proteins with Time-Resolved tmFRET

Preface

This chapter is adapted from the following published work:

Zagotta, W. N., Evans, E. G. B., Eggan, P., Tessmer, M. H., Shaffer, K. D., Petersson, E. J., Stoll, S., & Gordon, S. E. (2024). Measuring conformational equilibria in allosteric proteins with time-resolved tmFRET. *Biophysical journal*, *123*(14), 2050–2062. https://doi.org/10.1016/j.bpj.2024.01.033

It is included in this dissertation as it provides a conceptual and experimental foundation for the work in the subsequent chapters on time-resolved tmFRET, and illustrates its application to a model protein, maltose binding protein.

Author Contributions

Direct contribution to this work by P. Eggan, myself, include: conducting preliminary tests on the use of $[Fe(PhenM)_3]^{2+}$ and $[Ru(bpy)_2phenM]^{2+}$ as long-distance acceptors for Acd, data analysis using the frequency-domain lifetime model, and providing feedback and editing of the manuscript. The entire χ^2 analysis of the lifetime model fits and supplemental figures S2 and S3 were produced by me.

W.N. Zagotta and S.E. Gordon designed and conducted most experiments for this work and wrote the paper. E.Evans conducted experiments involving electron paramagnetic resonance (EPR) spectroscopy and wrote the sections of the paper on these experiments. M.H. Tessmer, E.J. Petersson and S. Stoll helped analyze data, contributed tools and edited the manuscript. K.D. Shaffer contributed tools.

Abstract

Proteins are the workhorses of biology, orchestrating a myriad of cellular functions through intricate conformational changes. Protein allostery, the phenomenon where binding of ligands or environmental changes induce conformational rearrangements in the protein, is fundamental to these processes. We have previously shown that transition metal Förster resonance energy transfer (tmFRET) can be used to interrogate the conformational rearrangements associated with protein allostery and have recently introduced novel FRET acceptors utilizing metal-bipyridyl derivatives to measure long (>20 Å) intramolecular distances in proteins. Here, we combine our tmFRET system with fluorescence lifetime measurements to measure the distances, conformational heterogeneity, and energetics of maltose binding protein (MBP), a model allosteric protein. Time-resolved tmFRET captures near-instantaneous snapshots of distance distributions, offering insights into protein dynamics. We show that time-resolved tmFRET can accurately determine distance distributions and conformational heterogeneity of proteins. Our results demonstrate the sensitivity of time-resolved tmFRET in detecting subtle conformational or energetic changes in protein conformations, which are crucial for understanding allostery. In addition, we extend the use of metal-bipyridyl compounds, showing $Cu(phen)^{2+}$ can serve as a spin label for pulse dipolar electron paramagnetic resonance (EPR) spectroscopy, a method which also reveals distance distributions and conformational heterogeneity. The EPR studies both establish $Cu(phen)^{2+}$ as a useful spin label for pulse dipolar EPR and validate our time-resolved tmFRET measurements. Our approach offers a versatile tool for deciphering conformational landscapes and understanding the regulatory mechanisms governing biological processes.

Introduction

Protein allostery plays a pivotal role in the regulation of virtually all biological processes. In response to the binding of specific molecules or changes in environmental conditions, allosteric proteins undergo distinct changes in structure that regulate the protein's activity or interaction with other molecules. This dynamic behavior allows proteins to function as molecular switches, orchestrating a wide range of biological functions such as enzymatic catalysis, signal transduction, gene regulation, and cellular motility.

The mechanism of allostery involves a choreography of the protein's structure and energetics. A stereotypical allosteric protein might have two conformations, a resting state and an active state (Figure 1A). Whereas the active state might be energetically unfavorable (positive ΔG) in the absence of ligand, it becomes more favorable (negative ΔG) in the presence of ligand. In this way, the conformation of the protein, and therefore its activity, is coupled to the binding of a ligand.

One general way to determine this ΔG is to measure conformational equilibria based on distance distributions between a pair of probes, attached to the protein of interest, which undergo a change in separation between resting and active states (Figure 1A). The hypothetical distance distributions in Figure 1A show that, in the absence of ligand, or "apo" condition, the resting conformation (longer distance) dominates, and, in saturating ligand or "holo" condition, the active conformation (shorter distance) dominates. The relative occupancy of the two conformations can be quantified by the relative area of the probability distribution for each conformational state. The ratio of the areas reveals the equilibrium constant and therefore the ΔG for the transition between the apo and holo states. These distance distributions reveal two types of heterogeneity that must be considered for any allosteric protein: 1) heterogeneity in functional state, as both resting and active conformations are present in both the absence and presence of ligand, and 2) for any given state, heterogeneity in the protein backbone and probe rotameric ensembles produce a distribution of distances between probes.

While Förster resonance energy transfer (FRET) has been used as a "molecular ruler" to measure distances in proteins, standard steady-state FRET experiments provide just a single

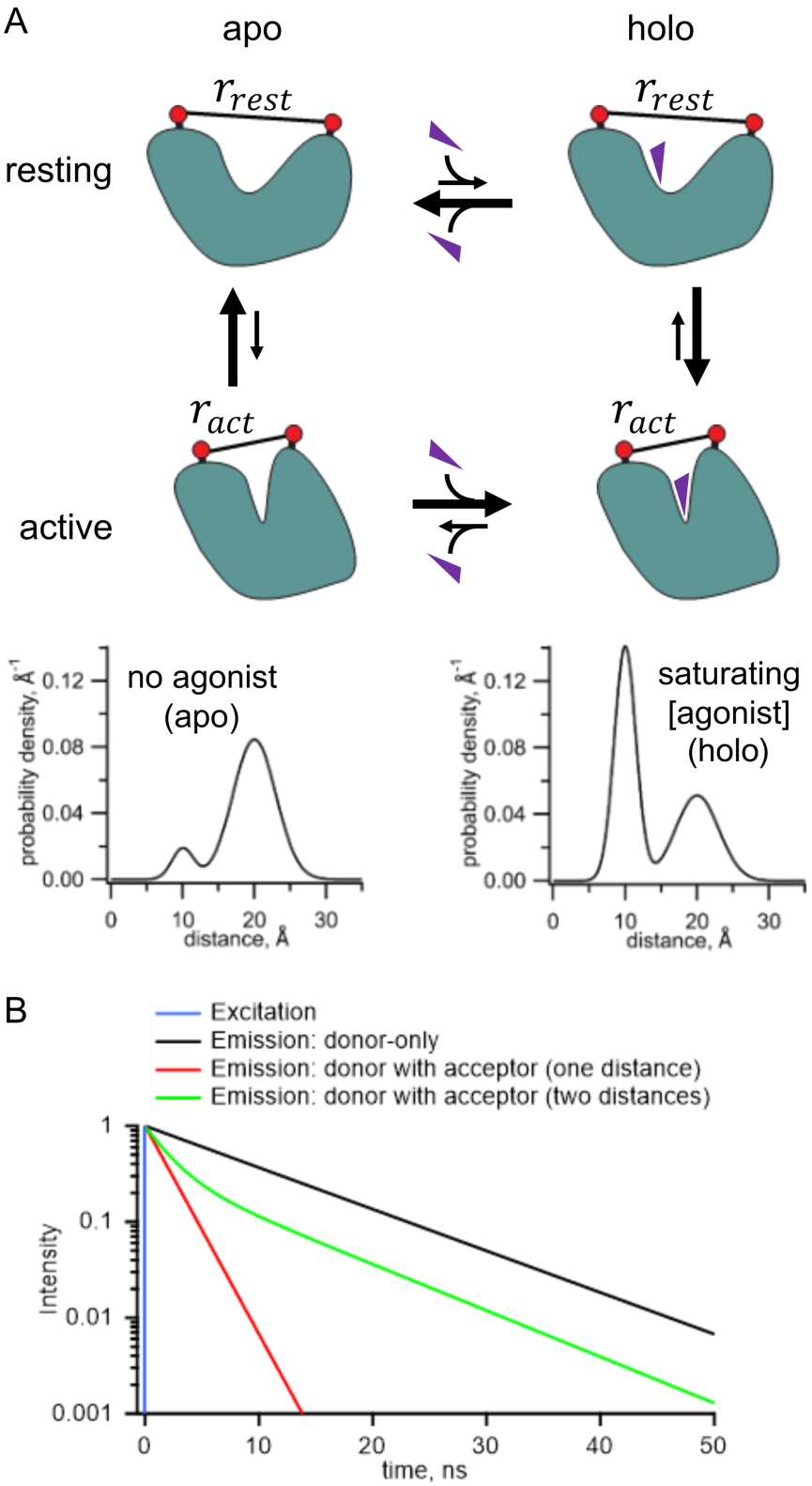

Figure 1. Measurement of distance distributions for an allosteric protein. (**A**) Conformational states (top) and distance distributions (bottom) for a stereotypical allosteric protein. The red circles represent the FRET probes and the purple triangles the ligand. (**B**) Theoretical effect of FRET with one or two distances on the fluorescent lifetimes in the time domain.

average distance (1,2). Time-resolved FRET experiments, however, generate richer data, from which the distribution of distances can be recovered (2-11). Time-resolved FRET utilizes fluorescence lifetimes, the latencies between absorption and emission of photons from a fluorophore. In the simplest cases, fluorescence lifetimes are single exponentially distributed with a time constant of a few nanoseconds. The presence of a FRET acceptor accelerates the fluorescence decay of the donor fluorophore in a manner that is highly dependent on the distance between the donor and acceptor (Figure 1B). If, for example, there are two states with different distances between the donor and acceptor, the decay will be double exponential with the fraction of each component representing the prevalence of that state. Importantly the interconversion among states is generally slower than the nanosecond fluorescence lifetime, so time-resolved FRET captures a near-instantaneous snapshot of the distance distribution without the averaging of distances, in contrast to steady-state or single-molecule fluorescence methods.

The utility of time-resolved FRET for deciphering protein dynamics has been limited by several experimental factors: 1) Labeling proteins site-specifically with donor and acceptor fluorophores can be a challenge. 2) The large size of most visible-light fluorophores and the length of the linkers that connect the fluorophores to the protein make it difficult to discriminate backbone dynamics and energetics from those of the fluorophore/linker. 3) Most fluorophores demonstrate multi-exponential lifetimes, which makes analysis of FRET data more complicated. 4) The fluorescence lifetimes of most dyes in common use are in the few-nanosecond range, giving a limited dynamic range for measuring time-resolved FRET. We recently developed a novel system for time-resolved FRET that overcomes these limitations by combining a noncanonical amino acid fluorophore donor and a transition metal ion acceptor (12). Here we employ this novel system with metal-bipyridyl acceptors, developed in a companion paper in this issue (13), to measure longer distance distributions in a model protein, maltose binding protein (MBP). We show that time-resolved FRET can quantify both the heterogeneity of a given conformational state and the energetics that govern the distribution of a protein among conformational states, collectively referred to as protein dynamics.

Materials and Methods

Expression and purification of MBP. For transition metal (tmFRET) experiments, the expression and purification of MBP was done as described previously (13). Briefly, MBP TAG

constructs with a C-terminal twin-strep tag were cotransfected with a plasmid containing the AcdA9 aminoacyl tRNA synthetase and its cognate tRNA (14) in BL-21(DE3) cells. Cultures were induced in the presence of 0.6 mM Acd in the media, and MBP was purified on a Streptactin column (IBA Life Sciences, Göttingen, Germany) column.

For relaxation-induced dipolar modulation enhancement (RIDME) experiments, dual cysteine constructs of MBP-295C-211C and MBP-322C-278C with N-terminal 6×His tags were expressed from a pETM11 vector in *E. coli* C43(DE3) and subsequently purified by Co^{2+} affinity chromatography as previously described (15). The 6xHis tag was removed by incubation with a 1:50 (TEV:MBP) weight ratio of TEV protease (4 h at room temperature, then 12 h at 4 °C) in K^+-Tris buffer (130 mM KCl, 30 mM Tris, pH 7.4) containing 0.5 mM EDTA and 1 mM TCEP. The reaction was desalted into K^+-Tris buffer (pH 7.4) plus 5 mM imidazole and 50 μM TCEP and further purified by reverse IMAC over TALON resin. Flow through containing cleaved MBP was supplemented with 1 mM TCEP and 5 mM EDTA, concentrated (30 kDa MWCO), and stored at 4 °C.

Labeling reagents. Phenanthroline maleimide (PhenM) and $[Ru(bpy)_2phenM]^{2+}$ were prepared as stocks in DMSO and used within minutes of final dilution into aqueous solution. 2 M hydroxylamine hydrochloride in water was prepared for use in Fe^{2+} experiments and used for only one day. $FeCl_2$ was prepared as a 100 mM stock with 1 M hydroxylamine hydrochloride in water and made fresh for each experiment day. $CuCl_2$ was prepared as a 100 mM stock in water.

$[Ru(bpy)_2phenM]^{2+}$ labeling. Time-resolved fluorescence measurements required a higher protein concentration (i.e., higher concentration of donor) and therefore a higher concentration of $[Ru(bpy)_2phenM]^{2+}$ was required for labeling. To reduce background absorption due to $[Ru(bpy)_2phenM]^{2+}$ in solution, we first labelled with $[Ru(bpy)_2phenM]^{2+}$ and then column purified the protein. Specifically, 100 mM $[Ru(bpy)_2phenM]^{2+}$ stock in DMSO was diluted to 1 mM in the concentrated protein in K^+-Tris buffer (pH 7.4). After 10 minutes, the solution was passed over a Bio-Rad Micro Bio-Spin 6 column that had been equilibrated with K^+-Tris buffer (pH 7.4) to remove unreacted label. K^+-Tris buffer (pH 7.4) was also used to elute the protein.

$[Fe(phenM)_3]^{2+}$ labeling. For $[Fe(phenM)_3]^{2+}$ experiments, a solution of 920 μM $FeCl_2$ in 9.2 mM hydroxylamine hydrochloride with 2.3 mM phenM was prepared in water. After recording the donor-only fluorescence lifetime, this $[Fe(phenM)_3]^{2+}$ solution was added to the protein drop

to a final concentration of 76.8 µM Fe^{2+}, 768 µM hydroxylamine hydrochloride, and 192 µM phenM. For these brief experiments, additional hydroxylamine hydrochloride was not required to prevent oxidation of Fe^{2+} to Fe^{3+}.

[Fe(phenM)]$^{2+}$ labeling. For [Fe(phenM)]$^{2+}$ experiments, a 20 mM phenM stock in K^+-Tris buffer (130 mM KCl, 30 mM Tris, pH 8.3) was added to MBP protein to achieve a final concentration of 2 mM phenM. After 10 minutes, the solution was passed over a Bio-Rad Micro Bio-Spin 6 column that had been equilibrated with K^+-Tris buffer (pH 8.3) to remove unreacted phenM label. K^+-Tris buffer (pH 8.3) was also used to elute the protein. After measuring the lifetime of the purified protein in the absence Fe^{2+}, we added Fe^{2+} (with a 10-fold excess of hydroxylamine hydrochloride) to a final concentration of 800 µM.

Measurement of fluorescence lifetime using FLIM. The theory underlying our FRET measurements with fluorescence lifetimes is well described elsewhere (2). Briefly, FRET decreases the fluorescence lifetime of a donor fluorophore by providing an additional path by which an excited state electron can lose its energy. When using a pulse excitation source and measuring fluorescence in the time domain, the decrease in lifetime is readily apparent as a faster decay in fluorescence intensity after excitation (Figure 1B). When using a frequency (ω) modulated excitation source, the lifetimes of donor in the absence and presence of acceptor are determined from the phase delays (the phase shift between the excitation and emission, φ_ω) and modulation ratios (the fractional decrease in the amplitude of the emission, m_ω) at each frequency (c.f. Figure 2A). With our frequency domain instrument, the frequency dependence of both φ_ω and m_ω are required to resolve complex lifetimes. A similar analysis can be performed using a time domain instrument (2).

Frequency domain fluorescence lifetime data were collected using a Q2 laser scanner and A320 FastFLIM system (ISS, Inc., Champaign, IL, USA) mounted on a Nikon TE2000U microscope (Melville, NY, USA) and VistaVision software (ISS, Inc.). Acd or Atto 425 (the standard for calibration of the fluorescence lifetime) were excited using a 375 nm pulse diode laser (ISS, Inc.), driven by FastFLIM at the repetition rate of 10 MHz, with a 387 nm long-pass dichroic mirror, and emission was collected using a 451/106 nm band-pass emission filter and Hamamatsu model H7422P PMT detector. Affinity purified protein was used after about a 1:10 dilution in K^+-Tris buffer. For each experiment, 11 µl of fluorescent sample was pipetted onto an

ethanol-cleaned #1.5 glass coverslip mounted directly above the 10x 0.5 NA objective. Other reagents (maltose, $[Ru(bpy)_2phenM]^{2+}$, $[Fe(phenM)_3]^{2+}$, Fe^{2+}, or EDTA) were pipetted directly into the sample drop and mixed at the final concentrations indicated in the text. For each condition, 256x256 confocal images were collected with a pinhole of 200 μm and a pixel dwell time of 1 ms. The pixels were averaged together for analysis, except as described for the phasor plot.

The experimental phase delays (φ_ω) and the modulation ratios (m_ω) of the fluorescence signal in response to an oscillatory stimulus with frequency ω were obtained using VistaVision software from the sine and cosine Fourier transform of the phase histogram *H(p)*, subject to the instrument response function (IRF) calibrated with 2 μM Atto 425 in water with a lifetime of 3.6 ns (2,16,17). These data were fit with the Gaussian model described in the Supporting Material to obtain distance distributions.

In silico labeling and distance distribution simulations. Computational modeling of Acd and metal-phenM labels, as well as distance distribution predictions, were performed using chiLife (18) with the accessible-volume sampling method (19,20). Acd, and cysteine conjugates of $[Ru(bpy)_2phenM]^{2+}$, $[Fe(phenM)_3]^{2+}$, $[Fe(phenM)]^{2+}$, and $[Cu(phenM)]^{2+}$ were added as custom labels in chiLife. Briefly, starting label structures were constructed in PyMOL and energy minimized with the GFN force field (GFN-FF) in xTB (21). Custom labels were superimposed onto labeling sites of the target pdb structure, and mobile dihedral angles were uniformly sampled. Rotamers with internal clashes (< 2 Å) were discarded. External clashes were evaluated using a modified, repulsive-only Lennard-Jones potential and used to weight rotamers as previously described (19). The lowest weighted rotamers cumulatively accounting for a fraction of 0.005 of the total rotamer weights were discarded. Sampling was terminated once 10,000 samples had been attempted, generating between 400 and 2,500 rotamers, depending on the specific label and protein site. To calculate a simulated distance distribution between two rotamer ensembles, a weighted histogram was made for pairwise distances between the spin or fluorescent centers of each pair of rotamers from the two ensembles. For Acd, the center coordinates were defined by the mean position of all atoms in the central acridone ring. For the metal-phenM labels, the center coordinates were on the transition metal ion. Histograms were

then convolved with gaussian distributions with a 1 Å standard deviation, and the resulting distributions were normalized.

[Cu(phenM)]$^{2+}$ spin-labeling and EPR sample preparation. Purified MBP-295C-211C and MBP-322C-278C (~ 50 μM) were desalted (G-25) into K^+-Tris buffer (pH 7.4) and immediately reacted with 0.5 mM phenM, freshly prepared from DMSO stock as a 5 mM solution in K^+-Tris buffer with 1 mM EDTA. The reaction was nutated at 4 °C for 1 h, desalted (G-25) into K^+-Tris buffer (pH 7.4), and concentrated (5 kDa MWCO). phenM-labeled MBP solutions were then incubated with 1 mM $CuSO_4$ for 10 minutes at room temperature and loaded into 10 kDa MWCO microdialysis units (Thermo) and dialyzed against K^+-Tris buffer prepared in deuterium oxide (D_2O). Dialysis was carried out for ~ 18 h, replacing dialysis buffer with fresh deuterated K^+-Tris buffer twice. RIDME samples were prepared with ~ 10 μM labeled MBP supplemented with 30 % (v/v) d8-glycerol. Holo MBP samples were additionally supplemented with 5 mM maltose from a stock solution in D_2O. Samples were loaded into 1.5 mm OD/1.1 mm ID quartz tubes (Sutter) with flame-sealed bottoms and flash frozen in liquid nitrogen (LN2). Samples were stored at −80 °C until measurement. Samples for CW EPR were prepared similarly, but without use of deuterated buffers and with 25 % (v/v) glycerol. CW EPR samples were loaded into 4 mm OD quartz EPR tubes (Wilmad), frozen in LN2, and measured on the same day.

EPR measurements. Continuous-wave EPR spectra were recorded at 112 K on a Bruker EMX spectrometer operating at X-band frequency (~9.3 GHz) with a Bruker ER 4102SHQE resonator. Spectra were recorded with 100 kHz field modulation with a sweep rate of 3.6 G/s and a modulation amplitude of 5 G. Spectra were background subtracted and baseline corrected in LabVIEW™. For visual comparison between samples (Figure S4), spectra were normalized by the double integral of the respected field-modulated spectrum. Magnetic parameters g and A were determined by least-squares fitting spectra using EasySpin 6.0 (22), assuming axial g and A tensors and including anisotropic line broadenings as additional fit parameters (Figure S4).

Pulse EPR experiments were performed at Q-band frequency (~34 GHz) using a Bruker EleXsys E580 spectrometer with an overcoupled Bruker EN 5107D2 resonator. Pulses were amplified with a 300 W TWT amplifier (Applied Systems Engineering) and sample temperatures of 20 K or 10 K were maintained using a variable-temperature cryogen-free system (Bruker/ColdEdge). RIDME was performed using the established 5-pulse sequence ($\pi/2$) — τ_1

— (π) — $\tau_1 + t$ — (π/2) — T_R — (π/2) — ($\tau_2 - t$) — (π) — τ_2 — (echo) (23). π /2 and π pulses were 12 and 24 ns, respectively, and were applied at frequency and magnetic field values corresponding to the maximum of the Cu^{2+} echo-detected field swept spectrum. To avoid dynamic decoupling artifacts in the RIDME time-trace, τ_1 was chosen to be longer than τ_2, with values of 4 μs and 3.5 μs for τ_1 and τ_2, respectively (24). Echo modulations due to solvent deuterium were suppressed by averaging over τ_1 and τ_2 with 16 ns increments over 8 steps. The relaxation interval T_R was 195 μs and was selected to be ~ 0.75 that of the spin-lattice relaxation time (T_{1e}) of the Cu^{2+} spin label at 20 K determined by inversion recovery experiments. Echo crossings were removed with a 32-step phase cycle (25); however, a small echo crossing artifact at $t \approx 0$ could not be removed by phase cycling. This artifact, along with residual ESEEM contributions, were removed by recording a second RIDME time-trace with identical pulse lengths and delays at 10 K, where $T_R \approx 0.04 T_{1e}$. Division of the 20 K data sets by the 10 K data sets gave the artifact-free dipolar evolution time traces used in all distance distribution analyses (Figure S5).

Divided and phase-corrected RIDME time-traces were analyzed with DeerLab version 1.1 (26) using Tikhonov regularization and compactness regularization (27). Residual intermolecular background was simultaneously modeled with the RIDME foreground using a homogenous 3-dimensional background model. The dipolar kernel was modified by replacing the default free electron g-value with an effective g-value of 2.1203 for each Cu^{2+} ion, which was determined from fits to the dual labeled MBP-$[Cu(phenM)]^{2+}$ CW EPR spectra. Uncertainty estimations were determined by the asymptotic method in DeerLab and 95% confidence intervals were plotted as error bands on the RIDME probability distributions. All plots were generated in KaleidaGraph version 5.0 (Synergy Software) and visualized with KaleidaGraph and Inkscape version 1.2.

Results

Time-resolved FRET can be measured in either the time domain, usually with time correlated single-photon counting (TCSPC), or in the frequency domain, with both approaches yielding equivalent information (2). Here, we measured fluorescence lifetimes using a

frequency-domain lifetime instrument (see Materials and Methods). For frequency-domain measurements, the lifetime data are visualized with a Weber plot that shows the phase shift of the response (phase delay) and the decrease in the amplitude of the response (modulation ratio) as a function of the modulation frequency of the excitation light (Figure 2A). These data can then be fit with models for the lifetimes that assume that they have single-exponential, multiexponential, or nonexponential decays.

To investigate the utility of time-resolved FRET to measure distance distributions, we incorporated the fluorescent noncanonical amino acid acridon-2-ylalanine (Acd) into MBP using amber codon suppression in bacteria as previously described (13,14,28). MBP is a clamshell-shaped protein that undergoes a significant closure of the clamshell upon binding maltose. For these experiments, we used two donor sites for specific incorporation of Acd, amino acid 295 at the outer lip of the clamshell and 322 on the back side of the clamshell. These donor fluorophore sites were then paired with single cysteine mutations for incorporation of transition metal chelates as FRET acceptors. Using MBP allowed us to test if time-resolved tmFRET could measure distances, distance distributions, and state energetics over a range of distances in a protein with a well-characterized structure and conformational rearrangement.

Acd incorporated at both donor sites (MBP-322Acd and MBP-295Acd) exhibited long, single-exponential fluorescence lifetimes similar to free Acd (Figure 2A and 5A, gray symbols). For Acd at 295 in wildtype MBP, the lifetime was nonexponential due to quenching by proximal Y307; therefore, all of our MBP-295Acd constructs also contain a Y307S mutation (referred to here as MBP-295Acd) (12,29). For both sites, the lifetimes were slightly longer in the presence of maltose (MBP-295Acd: apo, 14.7 ± 0.02 ns (n=13); holo 15.3 ± 0.1 ns (n=6); MBP-322Acd: apo, 15.4 ± 0.01 ns (n=20); holo 15.7 ± 0.01 ns (n=9)). This is likely due to a small change in the environment of the incorporated Acd in the presence of maltose and was factored into our subsequent analysis.

Time-resolved FRET with $[Ru(bpy)_2phenM]^{2+}$ and $[Fe(phenM)_3]^{2+}$produce accurate average distances and narrow distance distributions

In the previous paper, we have shown that the cysteine-reactive metal chelate [Ru(2,2′-bpy)$_2$(1,10-phenanthroline-5-maleimide)]$^{2+}$ ([Ru(bpy)$_2$phenM]$^{2+}$) can act as a long-distance tmFRET acceptor for Acd (13). [Ru(bpy)$_2$phenM]$^{2+}$ exhibits a substantial absorption in the

visible range that overlaps with the emission spectrum of Acd, giving an R_0, the distance producing 50% FRET efficiency, of 43.5 Å. Consistent with its R_0, labeling of MBP-322Acd-278C with $[Ru(bpy)_2phenM]^{2+}$ produced a substantial maltose-dependent decrease in steady-state Acd fluorescence indicating the presence of FRET between Acd and $[Ru(bpy)_2phenM]^{2+}$ (13). These steady-state FRET measurements, however, do not reveal the conformational heterogeneity in the sample.

To determine if time-resolved FRET could be used to measure distance distributions, we measured the fluorescence lifetimes of MBP-322Acd-278C labelled with $[Ru(bpy)_2phenM]^{2+}$. As shown in Figure 2A, labeling with $[Ru(bpy)_2phenM]^{2+}$ caused a substantial decrease in the average lifetime (manifesting as a shift in the phase delay and modulation ratio curves to *higher* frequencies in the Weber plot). Furthermore, subsequent addition of maltose increased the average lifetime (shifting the phase delay and modulation ratio curves to *lower* frequencies) reflecting an increase in the average distance between Acd at 322 and $[Ru(bpy)_2phenM]^{2+}$ at 278C, as predicted from structural modeling (see below). No change in lifetime was observed for MBP-322Acd without the cysteine mutation (data not shown; no native cysteines are present in MBP). These data suggest that time-resolved tmFRET could be used to reveal the intramolecular distance distributions in our samples.

To quantify the distance distributions from the fluorescence lifetime data, we fit the data with a model that predicts the lifetimes for a distribution of distances. The model assumes the following: 1) The fluorescence lifetimes of the donor-only protein (i.e., in the absence of acceptor) is single-exponentially distributed with a time constant τ_D (though τ_D can be different in the resting and active states). 2) The decrease in lifetime in the presence of the attached acceptor is due to a FRET mechanism with a known R_0. 3) Donor and acceptor dipoles are randomly oriented relative to each other ($\kappa^2 = 2/3$), a reasonable assumption when one member of the FRET pair is a metal ion (30). 4) There is only a single acceptor for each donor. 5) The distance distribution for each state can be approximated by a Gaussian distribution with a distinct mean distance and standard deviation. And 6) the distances do not change appreciably on the time scale of the fluorescence lifetime. Most of these assumptions can be experimentally verified in our sample. This Gaussian model was globally fit to the phase delay and modulation ratio data across multiple conditions in the same experiment (apo, holo, and intermediate concentrations of

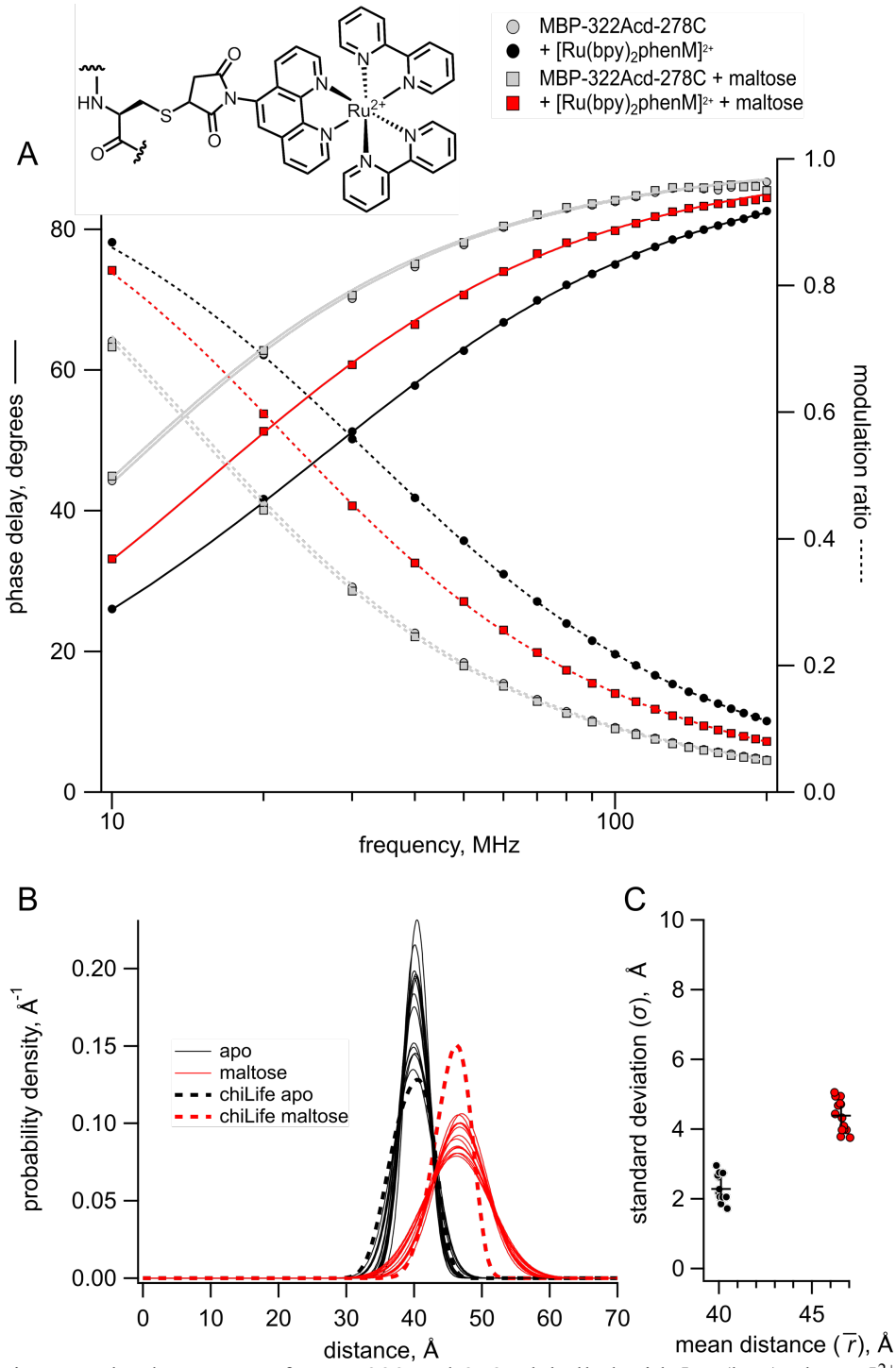

Figure 2. Time-resolved tmFRET of MBP-322Acd-278C labelled with $[Ru(bpy)_2phenM]^{2+}$. Structure of $[Ru(bpy)_2phenM]^{2+}$ label on the protein and legend for all panels are shown at the top. (**A**) Weber plot of the fluorescence lifetimes with 0 and 3 mM maltose in the presence and absence of $[Ru(bpy)_2phenM]^2$. (**B**) Spaghetti plot of the distance distributions measured by time-resolved tmFRET (thin solid curves) with 0 and 3 mM maltose (n=14) compared to the predicted distributions from chiLife for the resting and active state (dashed curves). (**C**) Scatter plot of the standard deviation vs. the mean distance for the Gaussian distributions with 0 and 3 mM maltose (n=14). The average values are shown as black +.

ligand). The values of 10 to 12 free parameters for each experiment were determined using χ^2 minimization. Because of how the distributions were parameterized, the fits generally had fewer free parameters than fitting with a sum of exponentials. This approach was pioneered in the 1970s, primarily by Steinberg and coworkers (31,32).

Global fits of the Gaussian model to the fluorescence lifetime data of MBP-322Acd-278C labelled with $[Ru(bpy)_2phenM]^{2+}$ in the apo and holo states are shown in Figure 2A. The values of the mean distances and standard deviations in the apo and holo states for 14 different experiments are shown in a spaghetti plot in Figure2B and a scatter plot in Figure 2C and were very reproducible. To compare our data to the predictions of structural modeling, rotameric ensembles of Acd and $[Ru(bpy)_2phenM]^{2+}$ were modelled onto crystal structures of apo and holo MBP (33,34) using the accessible-volume approach in chiLife (18), and used to predict distance distributions for MBP-322Acd-278C labeled with $[Ru(bpy)_2phenM]^{2+}$ (Figure 2B). In both the absence and presence of maltose, the distance distributions were remarkably similar to those predicted by chiLife. The average experimental distances and maltose-dependent delta distance were within 1 Å of those predicted by chiLife, and the widths of the distributions were also similar (though the experimentally determined width was consistently larger for the holo state). This similarity suggests that specific interactions between the probes and the protein (not accounted for by chiLife) do not play a significant role at these sites. Both the experimentally determined and predicted distance distributions between Acd and $[Ru(bpy)_2phenM]^{2+}$ were surprisingly narrow, indicating that $[Ru(bpy)_2phenM]^{2+}$ did not add appreciably to the measured heterogeneity under these conditions.

To determine the ability of tmFRET between Acd and $[Ru(bpy)_2phenM]^{2+}$ to resolve probability distributions that are a mixture of resting and active states, we performed lifetime experiments with subsaturating maltose concentrations applied to MBP-322Acd-278C labelled with $[Ru(bpy)_2phenM]^{2+}$, one just below the K_D and another just above the K_D. The intermediate concentrations produced intermediate curves on the Weber plot (Figure 3A). To analyze the lifetimes in a model-independent way, we graphed the data on a phasor plot, a plot of the out of-phase versus the in-phase components of the fluorescence in frequency domain experiments (16). This plot revealed that the data for these intermediate concentrations fall on a line between the zero and saturating maltose concentrations, indicating that these intermediate maltose

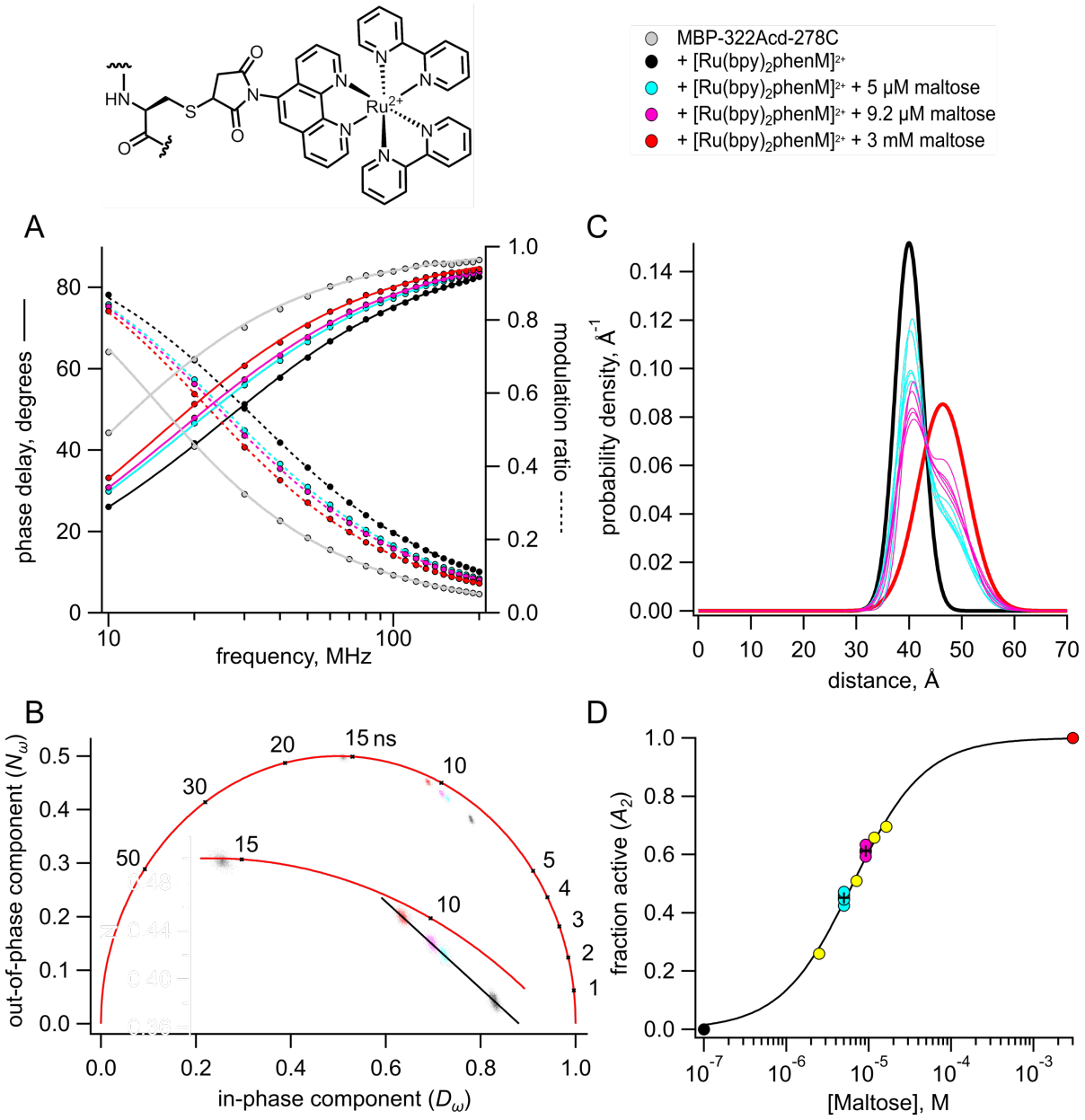

Figure 3. Time-resolved tmFRET of MBP-322Acd-278C labelled with $[Ru(bpy)_2phenM]^{2+}$ across a range of maltose concentrations. Structure of $[Ru(bpy)_2phenM]^{2+}$ and legend for all panels are shown at the top. (**A**) Weber plot of the fluorescence lifetimes with 0, 5 µM, 9.2 µM, and 3 mM maltose, in the presence and absence $[Ru(bpy)_2phenM]^{2+}$ (**B**) Phasor plot of the fluorescence lifetimes with 0, 5 µM, 9.2 µM, and 3 mM maltose, in the presence and absence of $[Ru(bpy)_2phenM]^{2+}$. The markers and numbers on the universal circle indicate time constants (in nanoseconds) for single exponential decays. A blowup of the region containing spots is shown in the inset. (**C**) Spaghetti plot of the distance distributions measured by time-resolved tmFRET with 5 µM, 9.2 µM (thin solid curves) and 0 and 3 mM (thick solid curves) maltose (n=5). (**D**) Scatter plot of maltose dose-response relation (n=5 for 5 µM and 9.2 µM maltose). The average values are shown as black +. A separate experiment with 5 different maltose concentrations is shown in yellow. Fit is with a Langmuir isotherm with a K_D of 6.3 µM maltose.

concentrations are a mixture of the same resting and active states produced by zero and saturating maltose (Figure 3B). We therefore performed global fits of the Gaussian model to the data on the Weber plot at all four maltose concentrations (0, 5 μM, 9.2 μM, and 3 mM), constraining the mean distance and standard deviation for each state to be the same for all conditions and allowing the fraction in the active state to vary (Fig 3C). The maltose dependence of the fraction of the active state nicely conformed to a binding isotherm, yielding an affinity of 6.3 μM, consistent with that previously measured using steady-state fluorescence (13) (Figure 3D). This is remarkable given that the difference in the average distance between the resting and active states is only about 6 Å.

We also performed similar time-resolved FRET experiments on MBP-322Acd-278C with $[Fe(\text{phen maleimide})_3]^{2+}$ ($[Fe(\text{phenM})_3]^{2+}$). Like Ru^{2+}, Fe^{2+} forms complexes with three bipyridyls or phenanthrolines that are highly absorbent in the visible range and can be used as FRET acceptors with visible fluorophores (13). The R_0 of Acd with $[Fe(\text{phenM})_3]^2$ is 41.8 Å. The addition of $[Fe(\text{phenM})_3]^{2+}$ caused a dramatic decrease in the average fluorescence lifetime of MBP-322Acd-278C as expected for FRET between Acd and $[Fe(\text{phenM})_3]^{2+}$ (Figure 4A). Furthermore, the average lifetime systematically increased upon addition of increasing concentrations of maltose, consistent with the maltose-dependent increase in distance predicted for MBP-322Acd-278C. No change in lifetime was observed for MBP-322Acd without the cysteine mutation (data not shown). Global fits of the Gaussian model to the data on the Weber plot at five different maltose concentrations (0, 5 μM, 9.2 μM, 12.9 μM, and 3 mM) yielded mean distances and standard deviations similar to those for $[Ru(bpy)_2\text{phenM}]^{2+}$, even though the R_0 was somewhat smaller (Figure 4D). The phasor plot (Figure 4B) and average distributions (Figure 4C) display a gradual shift in the equilibrium between the resting and active state with increasing maltose concentrations. Finally, the maltose dependence of the fraction of the active state nicely conformed to a binding isotherm, yielding an affinity of 9.2 μM for maltose (Figure 4E). These experiments demonstrate that both $[Ru(bpy)_2\text{phenM}]^{2+}$ and $[Fe(\text{phenM})_3]^{2+}$ make good acceptors when using time-resolved tmFRET to determine distance distributions among conformational states and the free energy difference between conformational states.

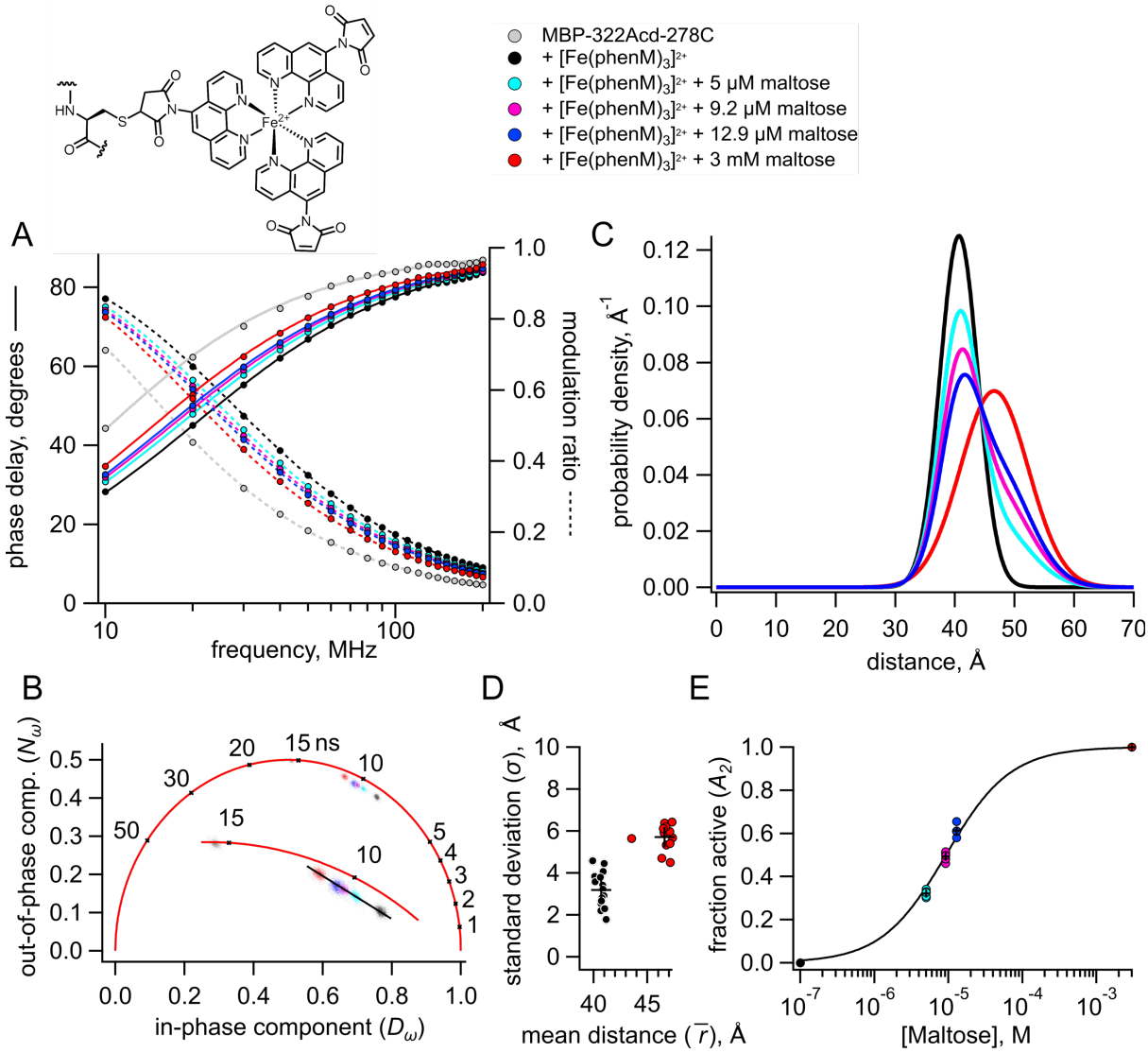

Figure 4. Time-resolved tmFRET of MBP-322Acd-278C labelled with $[Fe(phenM)_3]^{2+}$ across a range of maltose concentrations. Structure of $[Fe(phenM)_3]^{2+}$ and legend for all panels are shown at the top. (**A**) Weber plot of the fluorescence lifetimes with 0, 5 µM, 9.2 µM, 12.9 µM, and 3 mM, in the presence and absence of $[Fe(phenM)_3]^{2+}$. (**B**) Phasor plot of the fluorescence lifetimes with 0, 5 µM, 9.2 µM, 12.9 µM, and 3 mM, in the presence and absence of $[Fe(phenM)_3]^{2+}$. The markers and numbers on the universal circle indicate time constants (in nanoseconds) for single exponential decays. A blowup of the region containing spots is shown in the inset. (**C**) Plot of the average distance distributions measured by time-resolved tmFRET with 0, 5 µM, 9.2 µM, 12.9 µM, and 3 mM maltose (n=5). (**D**) Scatter plot of the standard deviation vs. the mean distance for the Gaussian distributions with 0 (n=16) and 3 mM (n=13) maltose. The average values are shown as black +. (**E**) Scatter plot of maltose dose-response relation (n=5 for 5 µM, 9.2 µM, 12.9 µM). The average values are shown as black +. Solid curve is a fit with a Langmuir isotherm with a K_D of 9.2 µM maltose.

Time-resolved FRET with $[Fe(phenM)]^{2+}$

For MBP-295Acd-211C, the predicted donor-acceptor distances are shorter (on the order of 30 Å) and, instead of maltose increasing the donor-acceptor distance like for MBP-322Acd-278C, maltose decreases the distance. At these distances, the FRET efficiency with $[Ru(bpy)_2phenM]^{2+}$ and $[Fe(phenM)_3]^{2+}$ is nearly one, making these acceptors inadequate for detecting distance changes in MBP-295Acd-211C (13). However, we have found that Fe^{2+} bound to a single phenanthroline maleimide ($[Fe(phenM)]^{2+}$) exhibits a much lower absorption and therefore a much lower R_0 (24.4 Å), making it ideal for the donor-acceptor distances in MBP-295Acd-211C (13).

The addition of Fe^{2+} caused a dramatic decrease in the average fluorescence lifetime of MBP-295Acd-211C-phenM as expected for FRET between Acd and $[Fe(phenM)]^{2+}$ (Figure 5A). The decrease in lifetime was even greater in the presence of saturating concentrations of maltose, as expected from the maltose-dependent decrease in distance between the donor and acceptor in MBP-295Acd-211C. For $[Fe(phenM)]^{2+}$, but not for $[Ru(bpy)_2phenM]^{2+}$ or $[Fe(phenM)_3]^{2+}$, the FRET was fully reversible with EDTA, as seen by the open symbols in the Weber plot surrounding the original donor-only points (Figure 5A). Fitting the Gaussian model to the lifetime data revealed that MBP-295Acd-211C-phenM had a somewhat broader distance distribution than MBP-322Acd-278C, but with a maltose-dependent decrease in average distance (Figure 5B and C). Once again, the distance distributions were similar to those predicted by chiLife, albeit with a somewhat shorter distance than predicted for the apo state. These data indicate that $[Fe(phenM)]^{2+}$ can be used as an effective FRET acceptor for lifetime measurements of distance distributions with mid-range donor-acceptor distances.

Pulse dipolar EPR with $[Cu(phenM)]^{2+}$

To further explore the heterogeneity contributed by the phenM side chain, we turned to pulse dipolar EPR spectroscopy. Pulse dipolar EPR methods such as double electron-electron resonance (DEER) and relaxation-induced dipolar modulation enhancement (RIDME) measure distance distributions between unpaired electrons introduced into proteins via site-directed spin labeling (35). These data are typically analyzed using non-parametric models and therefore place no underlying assumptions on the shape of the distance distributions, only that they are smooth.

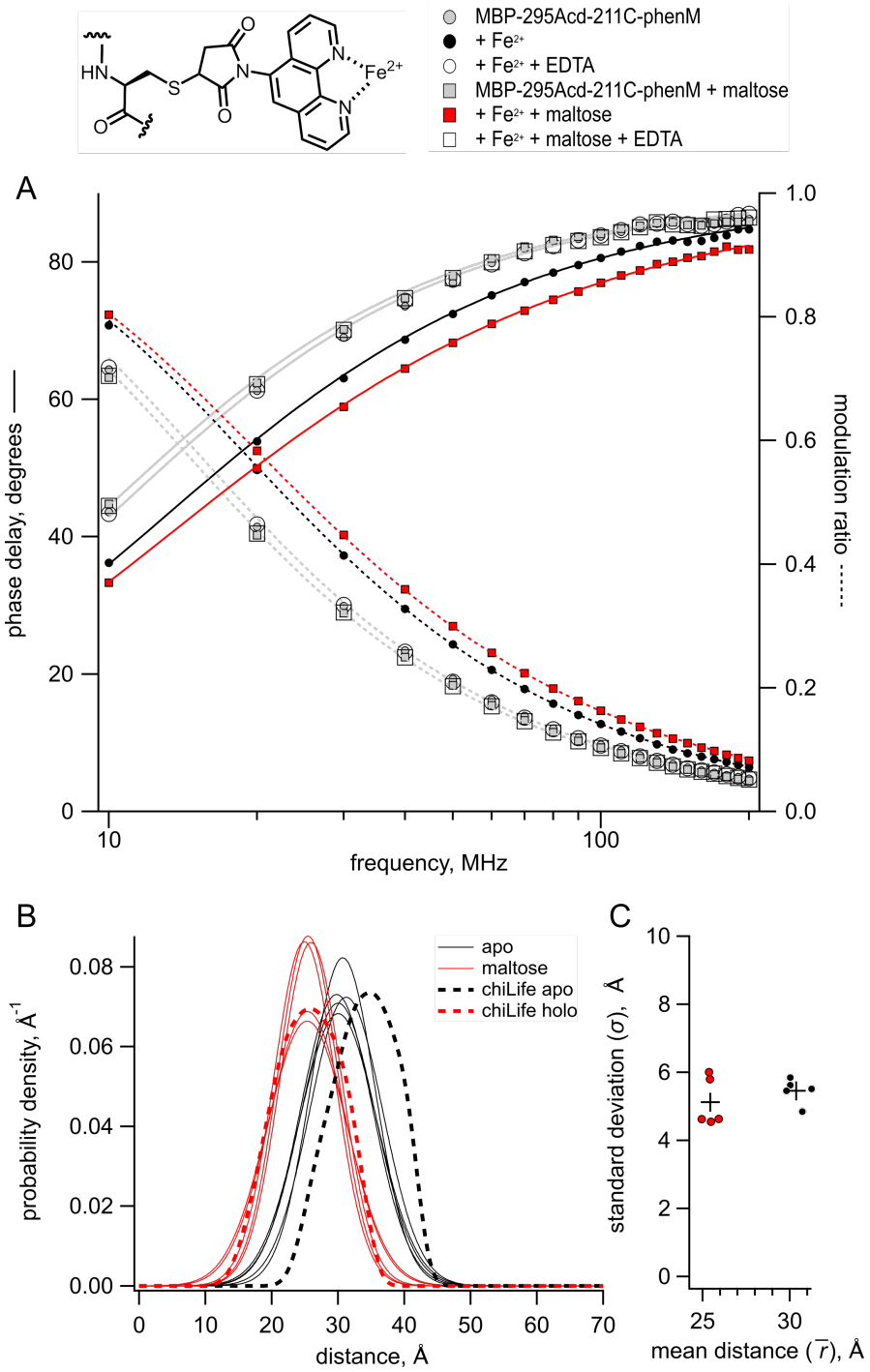

Figure 5. Time-resolved tmFRET of MBP-295Acd-211C labelled with $[Fe(phenM)]^{2+}$. Structure of $[Fe(phenM)]^{2+}$ and legend for all panels are shown at the top. (**A**) Weber plot of the fluorescence lifetimes of MBP-295Acd-211C-phenM with 0 and 3 mM maltose and in the presence and absence of Fe^{2+} and EDTA. (**B**) Spaghetti plot of the distance distributions measured by time-resolved tmFRET (thin solid curves) with 0 and 3 mM maltose (n=5) compared to the predicted distributions from chiLife for the resting and active state (dashed curves). (**C**) Scatter plot of the standard deviation vs. the mean distance for the Gaussian distributions with 0 and 3 mM maltose (n=5). The average values are shown as black +.

For these experiments, we introduced cysteine substitutions at both donor and acceptor sites in our previous MBP constructs, generating MBP-295C-211C and MBP-322C-278C. Nitroxide spin labels introduced at these site pairs have previously been employed to detect maltose-dependent conformational changes in MBP using DEER (15). To examine distance distributions obtained using the phenM label, MBP-295C-211C and MBP-322C-278C were labelled with phenM and subsequently labelled with Cu^{2+} (Figure 6A). Cu^{2+} is a d^9 transition metal ion containing one unpaired electron ($S = 1/2$) and can therefore be used as a spin label for EPR experiments. Indeed, both MBP-295C-211C and MBP-322C-278C dual labeled with $[Cu(phenM)]^{2+}$ displayed continuous-wave EPR spectra consistent with each Cu^{2+} coordinated by a single phenanthroline, indicating specific labeling of the phenM side chains with Cu^{2+} (Figure S4).

To determine distance distributions between $[Cu(phenM)]^{2+}$ labels on MBP directly, we performed RIDME experiments in the absence and presence of saturating maltose (Figure 6B, S5). For MBP-295C-211C labeled with $[Cu(phenM)]^{2+}$, RIDME in the absence of maltose reveals a broad distance distribution centered at 35.1 Å, which narrowed and shifted to a most probable distance of 28.6 Å in saturating maltose (Figure 6B). These distances are in excellent agreement with those predicted by chiLife (36.1 Å and 28.4 Å for apo and holo, respectively) (Figure 6B dashed line). RIDME data on MBP-322C-278C labeled with $[Cu(phenM)]^{2+}$, positioned on the backside of the clamshell, reveal the expected increase in Cu^{2+}–Cu^{2+} distance upon addition of maltose, with distance distributions centered at 43.5 Å and 49.5 Å for apo and holo conditions, respectively (Figure 6C). Again, these distances are within 1 Å of the chiLife predictions (43.1 Å and 49.8 Å for apo and holo, respectively). These results establish $[Cu\text{-}phenM]^{2+}$ as a useful and commercially available spin label for determining conformational distributions in proteins using pulse dipolar EPR spectroscopy. Moreover, the similarity of both the RIDME distributions (Figure 6B,C) and the tmFRET distributions (Figure 2B and 5B) to their respective chiLife predictions, and to each other, suggests the distributions at room temperature are well captured by the rapid freezing of the sample in the RIDME experiments. Overall, these experiments support the accuracy of RIDME, tmFRET, and chiLife for estimating the rotameric ensembles and resulting distance distributions involving $[metal(phenM)]^{2+}$ labels.

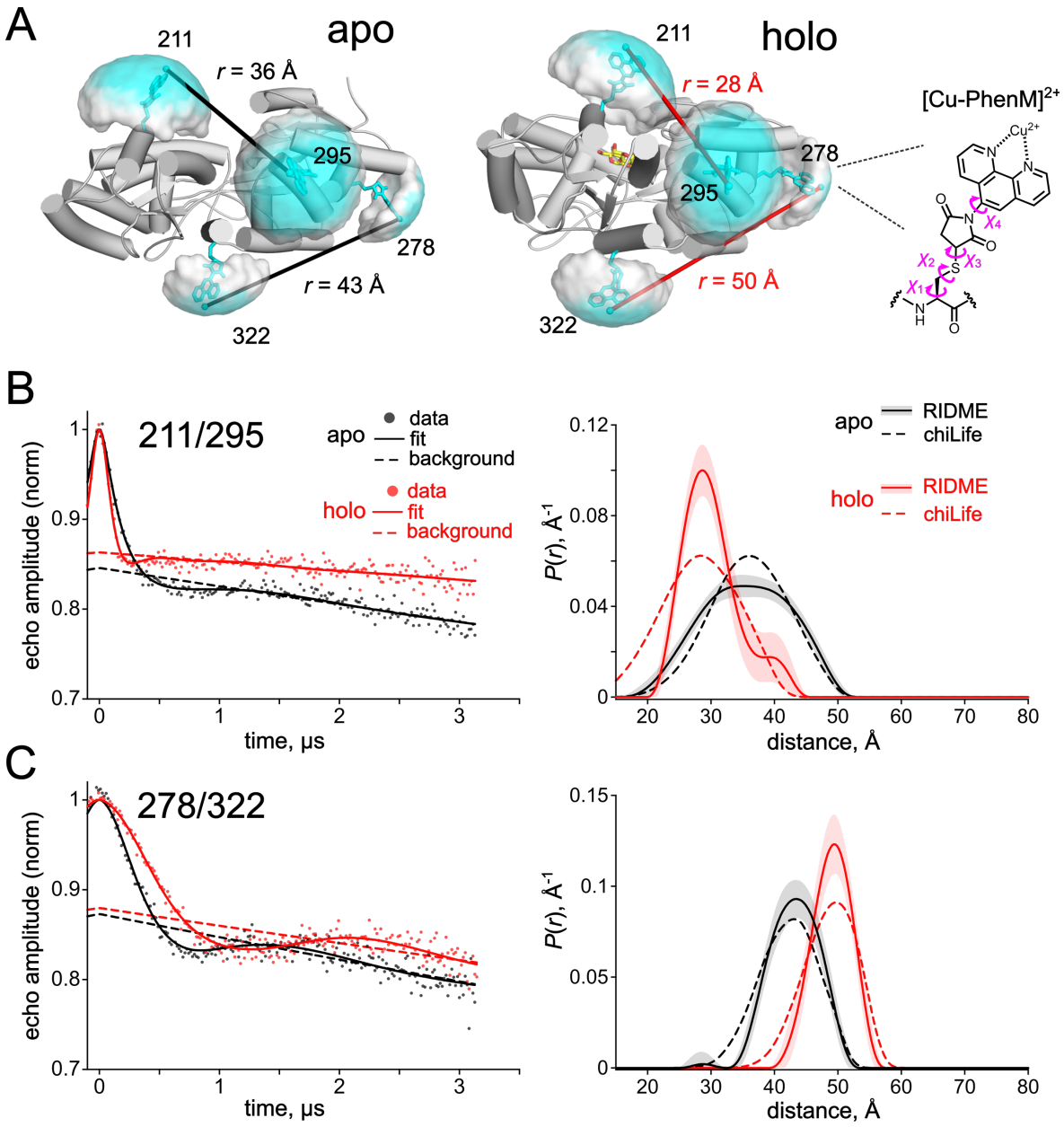

Figure 6. Pulse dipolar EPR distance distributions with the $[Cu(phenM)]^{2+}$ spin label. (**A**) Cartoon representations of resting state (pdb 1omp) (34) and active state (pdb 1anf) (33) of MBP labeled *in silico* with $[Cu(phenM)]^{2+}$ at 295C, 322C, 211C, and 278C using chiLife. Rotameric clouds are represented as surfaces and colored on a gradient from low (white) to high (cyan) probability. Predicted most probable distances determined by chiLife for the MBP-295C-211C and MBP-322C-278C site pairs are indicated. The structure of the spin-labeled $[Cu(phenM)]^{2+}$ side chain is shown at right. (**B, C**) 5-pulse RIDME time-traces and calculated distance distributions for $[Cu(phenM)]^{2+}$-labeled MBP-295C-211C (B) and MBP-322C-278C (C) in the absence of maltose (apo, black) and in the presence of 5 mM maltose (holo, red). Dashed curves on the distance distribution plot are predicted distributions calculated with chiLife. Shaded error bands on the RIDME distance distributions represent 95% confidence intervals determined from the DeerLab fits.

Discussion

This paper applies time-resolved tmFRET to study protein allostery and conformational dynamics. tmFRET utilizes a fluorescent noncanonical amino acid as the donor and our new metal-bipyridyl derivatives as the acceptor to overcome limitations of traditional FRET methods (13). We applied this method to MBP and demonstrated it can accurately determine distances, conformational heterogeneity, and energetics. The results highlight the utility of time-resolved tmFRET in characterizing protein dynamics and conformational changes, offering valuable insights into the mechanisms of allosteric regulation.

In addition to its utility in tmFRET, we showed that the cysteine-reactive bipyridyl derivative phenM can be used with Cu^{2+} as a spin label in pulse dipolar EPR spectroscopy. Distance distributions from pulsed dipolar EPR are commonly determined using non-parametric models which have the advantage of requiring no underlying assumptions about the shape of the distance distribution. Using the same sites on MBP to which we introduced the donor and acceptor for tmFRET, we show that the distance distributions produced by RIDME were similar to the predictions of chiLife and also to the distance distributions measured with time-resolved tmFRET. These results both establish $[Cu(phenM)]^{2+}$ as a spin label for pulse dipolar EPR spectroscopy and validate the distance distributions measured with time-resolved tmFRET.

The determination of distance distributions directly from the lifetime data is an ill-posed problem and, therefore, we needed to parameterize the distance distributions for our time-resolved tmFRET experiments. For our model, the heterogeneous distances between the donor and acceptor for each state were described by a Gaussian distribution with a distinct mean distance and standard deviation, although other distance distributions such as Lorentzians have also been used (36-38). Given these assumptions, values for the parameters were well determined from an analysis of the χ^2 surfaces (Figure S2A-D) and were fairly consistent across multiple experiments (Figures 2C, 4D, 5C). In addition, the distances, conformational heterogeneity, and energetics determined from the Gaussian model were consistent with molecular modeling (chiLife, Figure 2B, 5B) and EPR spectroscopy (RIDME, Figure 6), and subsaturating maltose concentrations (Figure 3 and 4).

Despite our promising results, correlation of some parameters was observed and overfitting the data was a concern. For example, the value of standard deviations of the Gaussian distance distributions covaried with the fraction of donor only (Figure S2E,F), making it important that the amount of donor only is small (<20%) and is verified with independent experiments (see Figure S6 of (13)). Fitting a single condition (e.g., apo and holo) assuming two Gaussian components (two conformational states) did not always yield consistent results across experiments. For that reason, we assumed the apo and holo conditions contained only a single Gaussian component (a single conformation) for each condition. This is a reasonable assumption for MBP where the protein is thought to be largely in a single conformational state in apo and holo conditions (39). However, for many other proteins, we expect that apo and holo conditions will contain a mixture of resting and active states (Figure 1A) (40). Some future modifications that might help improve the fitting under these conditions include: 1) global fitting of the fluorescence lifetime and steady-state FRET efficiency under the same condition, 2) global fitting of the data across multiple similar FRET pairs with different R_0 values, and 3) constraining one or more of the Gaussian components to the predictions of molecular modeling or molecular dynamics calculations. Ultimately, a Bayesian inference analysis of the Gaussian model is needed to characterize the uncertainties and correlations among the parameters, as has been done with DEER (41).

Acknowledgements

We thank the Oregon State University GCE4ALL (Center for Genetic Code Expansion for All) for their long-standing collaboration, Dr. Shauna C. Otto (University of Washington) and Dr. Chloe Jones (University of Pennsylvania) for excellent technical support, and Richard W. Aldrich for everything else. Research reported in this publication was supported by the National Institutes of Health under award numbers R35GM145225 (to S.E.G.), R35GM148137 and R03TR004135 (to W.N.Z.), R01GM125753 (to S.S.), T32EY007031 (to E.G.B.E), and T32GM008268 (to P.E.). This research was also supported in part by the National Science Foundation under grant DGE-1747486 (E.J.P.).

References

1. Stryer, L., and R. P. Haugland. 1967. Energy transfer: a spectroscopic ruler. *Proc Natl Acad Sci U S A*. 58(2):719-726, http://www.ncbi.nlm.nih.gov/pubmed/5233469.
2. Lakowicz, J. R. 2006. Principles of fluorescence spectroscopy. Springer, New York.
3. Eis, P. S., and D. P. Millar. 1993. Conformational distributions of a four-way DNA junction revealed by time-resolved fluorescence resonance energy transfer. *Biochemistry*. 32(50):13852-13860, doi: 10.1021/bi00213a014, https://www.ncbi.nlm.nih.gov/pubmed/8268160.
4. Hochstrasser, R. A., S. M. Chen, and D. P. Millar. 1992. Distance distribution in a dye-linked oligonucleotide determined by time-resolved fluorescence energy transfer. *Biophys Chem*. 45(2):133-141, doi: 10.1016/0301-4622(92)87005-4, https://www.ncbi.nlm.nih.gov/pubmed/1286148.
5. Yang, M., and D. P. Millar. 1996. Conformational flexibility of three-way DNA junctions containing unpaired nucleotides. *Biochemistry*. 35(24):7959-7967, doi: 10.1021/bi952892z, https://www.ncbi.nlm.nih.gov/pubmed/8672499.
6. Gryczynski, I., W. Wiczk, M. L. Johnson, H. C. Cheung, C. K. Wang, and J. R. Lakowicz. 1988. Resolution of end-to-end distance distributions of flexible molecules using quenching-induced variations of the Forster distance for fluorescence energy transfer. *Biophys J*. 54(4):577-586, doi: 10.1016/S0006-3495(88)82992-8, https://www.ncbi.nlm.nih.gov/pubmed/3224143.
7. Lakowicz, J. R., I. Gryczynski, H. C. Cheung, C. K. Wang, and M. L. Johnson. 1988. Distance distributions in native and random-coil troponin I from frequency-domain measurements of fluorescence energy transfer. *Biopolymers*. 27(5):821-830, doi: 10.1002/bip.360270509, https://www.ncbi.nlm.nih.gov/pubmed/3382720.
8. Lakowicz, J. R., I. Gryczynski, W. Wiczk, G. Laczko, F. C. Prendergast, and M. L. Johnson. 1990. Conformational distributions of melittin in water/methanol mixtures from frequency-domain measurements of nonradiative energy transfer. *Biophys Chem*. 36(2):99-115, doi: 10.1016/0301-4622(90)85014-w, https://www.ncbi.nlm.nih.gov/pubmed/2207280.
9. Lakowicz, J. R., J. Kuśba, W. Wiczk, I. Gryczynski, H. Szmacinski, and M. L. Johnson. 1991. Resolution of the conformational distribution and dynamics of a flexible molecule using frequency-domain fluorometry. *Biophys Chem*. 39(1):79-84, doi: 10.1016/0301-4622(91)85008-e, https://www.ncbi.nlm.nih.gov/pubmed/2012836.
10. Lakowicz, J. R., I. Gryczynski, G. Laczko, W. Wiczk, and M. L. Johnson. 1994. Distribution of distances between the tryptophan and the N-terminal residue of melittin in its complex with calmodulin, troponin C, and phospholipids. *Protein Sci*. 3(4):628-637, doi: 10.1002/pro.5560030411, https://www.ncbi.nlm.nih.gov/pubmed/8003981.
11. Cheung, H. C., I. Gryczynski, H. Malak, W. Wiczk, M. L. Johnson, and J. R. Lakowicz. 1991. Conformational flexibility of the Cys 697-Cys 707 segment of myosin subfragment-1. Distance distributions by frequency-domain fluorometry. *Biophys Chem*. 40(1):1-17, doi: 10.1016/0301-4622(91)85025-l, https://www.ncbi.nlm.nih.gov/pubmed/1873469.
12. Zagotta, W. N., B. S. Sim, A. K. Nhim, M. M. Raza, E. G. Evans, Y. Venkatesh, C. M. Jones, R. A. Mehl, E. J. Petersson, and S. E. Gordon. 2021. An improved fluorescent noncanonical amino acid for measuring conformational distributions using time-resolved

transition metal ion FRET. *Elife*. 10, doi: 10.7554/eLife.70236, https://www.ncbi.nlm.nih.gov/pubmed/34623258.
13. Gordon, S. E., E. G. B. Evans, S. C. Otto, M. H. Tessmer, K. D. Shaffer, M. T. Gordon, E. J. Petersson, S. Stoll, and W. N. Zagotta. 2024. Long-distance tmFRET using bipyridyl- and phenanthroline-based ligands. *Biophys J*. In press.
14. Sungwienwong, I., Z. M. Hostetler, R. J. Blizzard, J. J. Porter, C. M. Driggers, L. Z. Mbengi, J. A. Villegas, L. C. Speight, J. G. Saven, J. J. Perona, R. M. Kohli, R. A. Mehl, and E. J. Petersson. 2017. Improving target amino acid selectivity in a permissive aminoacyl tRNA synthetase through counter-selection. *Org Biomol Chem*. 15(17):3603-3610, doi: 10.1039/c7ob00582b, https://www.ncbi.nlm.nih.gov/pubmed/28397914.
15. Jana, S., E. G. B. Evans, H. S. Jang, S. Zhang, H. Zhang, A. Rajca, S. E. Gordon, W. N. Zagotta, S. Stoll, and R. A. Mehl. 2023. Ultrafast Bioorthogonal Spin-Labeling and Distance Measurements in Mammalian Cells Using Small, Genetically Encoded Tetrazine Amino Acids. *J Am Chem Soc*. doi: 10.1021/jacs.3c00967, https://www.ncbi.nlm.nih.gov/pubmed/37364003.
16. Digman, M. A., V. R. Caiolfa, M. Zamai, and E. Gratton. 2008. The phasor approach to fluorescence lifetime imaging analysis. *Biophys J*. 94(2):L14-16, doi: 10.1529/biophysj.107.120154, https://www.ncbi.nlm.nih.gov/pubmed/17981902.
17. Colyer, R. A., C. Lee, and E. Gratton. 2008. A novel fluorescence lifetime imaging system that optimizes photon efficiency. *Microsc Res Tech*. 71(3):201-213, doi: 10.1002/jemt.20540, https://www.ncbi.nlm.nih.gov/pubmed/18008362.
18. Tessmer, M. H., and S. Stoll. 2023. chiLife: An open-source Python package for in silico spin labeling and integrative protein modeling. *PLoS Comput Biol*. 19(3):e1010834, doi: 10.1371/journal.pcbi.1010834, https://www.ncbi.nlm.nih.gov/pubmed/37000838.
19. Tessmer, M. H., E. R. Canarie, and S. Stoll. 2022. Comparative evaluation of spin-label modeling methods for protein structural studies. *Biophys J*. 121(18):3508-3519, doi: 10.1016/j.bpj.2022.08.002, https://www.ncbi.nlm.nih.gov/pubmed/35957530.
20. Hagelueken, G., R. Ward, J. H. Naismith, and O. Schiemann. 2012. MtsslWizard: In Silico Spin-Labeling and Generation of Distance Distributions in PyMOL. *Appl Magn Reson*. 42(3):377-391, doi: 10.1007/s00723-012-0314-0, https://www.ncbi.nlm.nih.gov/pubmed/22448103.
21. Spicher, S., and S. Grimme. 2020. Robust Atomistic Modeling of Materials, Organometallic, and Biochemical Systems. *Angew Chem Int Ed Engl*. 59(36):15665-15673, doi: 10.1002/anie.202004239, https://www.ncbi.nlm.nih.gov/pubmed/32343883.
22. Stoll, S., and A. Schweiger. 2006. EasySpin, a comprehensive software package for spectral simulation and analysis in EPR. *J Magn Reson*. 178(1):42-55, doi: 10.1016/j.jmr.2005.08.013, https://www.ncbi.nlm.nih.gov/pubmed/16188474.
23. Milikisyants, S., F. Scarpelli, M. G. Finiguerra, M. Ubbink, and M. Huber. 2009. A pulsed EPR method to determine distances between paramagnetic centers with strong spectral anisotropy and radicals: the dead-time free RIDME sequence. *J Magn Reson*. 201(1):48-56, doi: 10.1016/j.jmr.2009.08.008, https://www.ncbi.nlm.nih.gov/pubmed/19758831.
24. Abdullin, D., M. Suchatzki, and O. Schiemann. 2022. Six-Pulse RIDME Sequence to Avoid Background Artifacts. *Appl. Magn. Reson.* 53:539–554, doi: 10.1007/s00723-021-01326-1.

25. Ritsch, I., H. Hintz, G. Jeschke, A. Godt, and M. Yulikov. 2019. Improving the accuracy of Cu(ii)-nitroxide RIDME in the presence of orientation correlation in water-soluble Cu(ii)-nitroxide rulers. *Phys Chem Chem Phys*. 21(19):9810-9830, doi: 10.1039/c8cp06573j, https://www.ncbi.nlm.nih.gov/pubmed/31025988.
26. Fábregas Ibáñez, L., G. Jeschke, and S. Stoll. 2020. DeerLab: a comprehensive software package for analyzing dipolar electron paramagnetic resonance spectroscopy data. *Magn Reson (Gott)*. 1(2):209-224, doi: 10.5194/mr-1-209-2020, https://www.ncbi.nlm.nih.gov/pubmed/34568875.
27. Fábregas-Ibáñez, L., G. Jeschke, and S. Stoll. 2022. Compactness regularization in the analysis of dipolar EPR spectroscopy data. *J Magn Reson*. 339:107218, doi: 10.1016/j.jmr.2022.107218, https://www.ncbi.nlm.nih.gov/pubmed/35439683.
28. Jones, C. M., Y. Venkatesh, and E. J. Petersson. 2020. Protein labeling for FRET with methoxycoumarin and acridonylalanine. *Methods Enzymol*. 639:37-69, doi: 10.1016/bs.mie.2020.04.008, https://www.ncbi.nlm.nih.gov/pubmed/32475410.
29. Speight, L. C., A. K. Muthusamy, J. M. Goldberg, J. B. Warner, R. F. Wissner, T. S. Willi, B. F. Woodman, R. A. Mehl, and E. J. Petersson. 2013. Efficient synthesis and in vivo incorporation of acridon-2-ylalanine, a fluorescent amino acid for lifetime and Förster resonance energy transfer/luminescence resonance energy transfer studies. *J Am Chem Soc*. 135(50):18806-18814, doi: 10.1021/ja403247j, https://www.ncbi.nlm.nih.gov/pubmed/24303933.
30. Haas, E., E. Katchalski-Katzir, and I. Z. Steinberg. 1978. Effect of the orientation of donor and acceptor on the probability of energy transfer involving electronic transitions of mixed polarization. *Biochemistry*. 17(23):5064-5070, doi: 10.1021/bi00616a032, https://www.ncbi.nlm.nih.gov/pubmed/718874.
31. Haas, E., M. Wilchek, E. Katchalski-Katzir, and I. Z. Steinberg. 1975. Distribution of end-to-end distances of oligopeptides in solution as estimated by energy transfer. *Proc Natl Acad Sci U S A*. 72(5):1807-1811, doi: 10.1073/pnas.72.5.1807, https://www.ncbi.nlm.nih.gov/pubmed/1057171.
32. Grinvald, A., E. Haas, and I. Z. Steinberg. 1972. Evaluation of the distribution of distances between energy donors and acceptors by fluorescence decay. *Proc Natl Acad Sci U S A*. 69(8):2273-2277, doi: 10.1073/pnas.69.8.2273, https://www.ncbi.nlm.nih.gov/pubmed/16592008.
33. Quiocho, F. A., J. C. Spurlino, and L. E. Rodseth. 1997. Extensive features of tight oligosaccharide binding revealed in high-resolution structures of the maltodextrin transport/chemosensory receptor. *Structure*. 5(8):997-1015, doi: 10.1016/s0969-2126(97)00253-0, https://www.ncbi.nlm.nih.gov/pubmed/9309217.
34. Sharff, A. J., L. E. Rodseth, J. C. Spurlino, and F. A. Quiocho. 1992. Crystallographic evidence of a large ligand-induced hinge-twist motion between the two domains of the maltodextrin binding protein involved in active transport and chemotaxis. *Biochemistry*. 31(44):10657-10663, doi: 10.1021/bi00159a003, https://www.ncbi.nlm.nih.gov/pubmed/1420181.
35. Goldfarb, D. 2022. Exploring protein conformations in vitro and in cell with EPR distance measurements. *Curr Opin Struct Biol*. 75:102398, doi: 10.1016/j.sbi.2022.102398, https://www.ncbi.nlm.nih.gov/pubmed/35667279.
36. Wu, P., and L. Brand. 1994. Conformational flexibility in a staphylococcal nuclease mutant K45C from time-resolved resonance energy transfer measurements. *Biochemistry*.

33(34):10457-10462, doi: 10.1021/bi00200a029, https://www.ncbi.nlm.nih.gov/pubmed/8068683.
37. Amir, D., and E. Haas. 1986. Determination of intramolecular distance distributions in a globular protein by nonradiative excitation energy transfer measurements. *Biopolymers*. 25(2):235-240, doi: 10.1002/bip.360250205, https://www.ncbi.nlm.nih.gov/pubmed/2420384.
38. Amir, D., S. Krausz, and E. Haas. 1992. Detection of local structures in reduced unfolded bovine pancreatic trypsin inhibitor. *Proteins*. 13(2):162-173, doi: 10.1002/prot.340130210, https://www.ncbi.nlm.nih.gov/pubmed/1377825.
39. Tang, C., C. D. Schwieters, and G. M. Clore. 2007. Open-to-closed transition in apo maltose-binding protein observed by paramagnetic NMR. *Nature*. 449(7165):1078-1082, doi: 10.1038/nature06232, https://www.ncbi.nlm.nih.gov/pubmed/17960247.
40. DeBerg, H. A., P. S. Brzovic, G. E. Flynn, W. N. Zagotta, and S. Stoll. 2016. Structure and Energetics of Allosteric Regulation of HCN2 Ion Channels by Cyclic Nucleotides. *J Biol Chem*. 291(1):371-381, doi: 10.1074/jbc.M115.696450, https://www.ncbi.nlm.nih.gov/pubmed/26559974.
41. Sweger, S. R., S. Pribitzer, and S. Stoll. 2020. Bayesian Probabilistic Analysis of DEER Spectroscopy Data Using Parametric Distance Distribution Models. *J Phys Chem A*. 124(30):6193-6202, doi: 10.1021/acs.jpca.0c05026, https://www.ncbi.nlm.nih.gov/pubmed/32614584.

Supporting Material

Analysis of Frequency Domain Lifetime Data The theoretical estimates for φ_ω and m_ω were calculated from a model for fluorescence lifetime and FRET that assumes a single-exponential donor fluorescence lifetime with one or two Gaussian-distributed distances between the donor and acceptor as previously described with some modification (2,9,32,33). The phase delays (φ_ω) and modulation ratios (m_ω) were calculated as a function of the modulation frequency (ω) using the following equations:

$$\varphi_\omega = \arctan\left(\frac{N_\omega}{D_\omega}\right) + \omega t_0 \qquad \text{Equation 1}$$

$$m_\omega = \sqrt{(N_\omega^2 + D_\omega^2)} \qquad \text{Equation 2}$$

where the N_ω corresponds to the out-of-phase component and D_ω corresponds to the in-phase component of fluorescence and t_0 is the time shift of the IRF (Figure S1E). The two components for the fluorescence response with a contaminating background fluorescence were calculated using the following equations:

$$N_\omega = \left(1 - \frac{f_B}{k}\right)\frac{1}{J}\int_0^\infty \sum_{i=1}^2 \frac{P_i(r)\omega\tau_{DA_i}^2}{1+\omega^2\tau_{DA_i}^2} dr + \frac{f_B}{k} m_{\omega B}\sin(\varphi_{\omega B}) \qquad \text{Equation 3}$$

$$D_\omega = \left(1 - \frac{f_B}{k}\right)\frac{1}{J}\int_0^\infty \sum_{i=1}^2 \frac{P_i(r)\tau_{DA_i}}{1+\omega^2\tau_{DA_i}^2} dr + \frac{f_B}{k} m_{\omega B}\cos(\varphi_{\omega B}) \qquad \text{Equation 4}$$

where $f_B$is the fraction of the fluorescence intensity due to background (Figure S1D), and $\varphi_{\omega B}$ and $m_{\omega B}$ are the phase delay and modulation ratio of the background fluorescence measured from samples of K^+-Tris Buffer without or with maltose. (Figure S1A). The normalization factor J is given by:

$$J = \int_0^\infty \sum_{i=1}^2 P_i(r)\tau_{DA_i}\, dr \qquad \text{Equation 5}$$

The decay time constant of the ith component of the donor lifetime in the presence of acceptor (τ_{DAi}) is given by:

$$\frac{1}{\tau_{DA_i}} = \frac{1}{\tau_{D_i}} + \frac{1}{\tau_{D_i}}\left(\frac{R_0}{r}\right)^6 \qquad \text{Equation 6}$$

where τ_{D_i} is the decay time constant of the donor in the absence of acceptor (Figure S1A), r is the distance between the donor and acceptor, and R_0 is the characteristic distance for the donor-acceptor pair (Figure S1B).

The apparent FRET efficiency based on the donor quenching of the acceptor (E) was calculated using the following equation:

$$E = 1 - J/\sum_{i=1}^{2} A_i \tau_{DA_i} \qquad \text{Equation 7}$$

The correction factor for the fraction of background for the decrease in intensity due to FRET (k) was given by the following equation:

$$k = 1 - E(1 - f_B) \qquad \text{Equation 8}$$

The distribution of donor-acceptor distances ($P(r)$) was assumed to be the sum of up to two Gaussians:

$$P_i(r) = A_i \left\{ (1 - f_D) \frac{1}{\sigma_i \sqrt{2\pi}} exp\left[-\frac{1}{2} \left(\frac{r - \bar{r}_i}{\sigma_i} \right)^2 \right] + \frac{f_D}{\sigma_i \sqrt{2\pi}} exp\left[-\frac{1}{2} \left(\frac{r - 150\ \text{Å}}{0.1\ \text{Å}} \right)^2 \right] \right\} \qquad \text{Equation 9}$$

where A_i, $\bar{r}_i$, and σ_i are the amplitude, mean, and standard deviation of the ith Gaussian respectively, and $A_1 + A_2 = 1$ (Figure S1C). The fraction of donor only (f_D) was modeled as a narrow Gaussian with a mean distance of 150 Å and a standard deviation of 0.1 Å, too far to exhibit any detectable FRET.

The phase delay and modulation ratios displayed were corrected for the background fluorescence and time shift in the IRF using the following equations:

$$\varphi_\omega^{corr.} = \arctan\left(\frac{m_\omega \sin(\varphi_\omega - \omega t_0) - \frac{f_B}{k} m_{\omega B} \sin(\varphi_{\omega B})}{m_\omega \cos(\varphi_\omega - \omega t_0) - \frac{f_B}{k} m_{\omega B} \cos(\varphi_{\omega B})} \right) \qquad \text{Equation 10}$$

$$m_\omega^{corr.} = \sqrt{\left[\frac{m_\omega \sin(\varphi_\omega - \omega t_0) - \frac{f_B}{k} m_{\omega B} \sin(\varphi_{\omega B})}{1 - \frac{f_B}{k}} \right]^2 + \left[\frac{m_\omega \cos(\varphi_\omega - \omega t_0) - \frac{f_B}{k} m_{\omega B} \cos(\varphi_{\omega B})}{1 - \frac{f_B}{k}} \right]^2} \qquad \text{Equation 11}$$

This Gaussian model for fluorescence lifetimes and FRET was implemented in Igor Pro v8 (Wavemetrics, Lake Oswego, OR) (code available at https://github.com/zagotta/FDlifetime_program_v2). The Gaussian model was globally fit, with χ^2 minimization, to the phase delay and modulation ratio for donor+acceptor fluorescence in the absence of maltose and in the presence of various concentrations of maltose as indicated in the text. There are 11 parameters in the parameter vector ($f_D, \tau_{D1}, \tau_{D2}, R_0, \bar{r}_1, \sigma_1, A_2, \bar{r}_2, \sigma_2, t_0, f_B$) (Figure S1, blue variables). For the global fits. τ_{D1}, τ_{D2}, and R_0 were constrained to previously determined values, $f_D, \bar{r}_1, \sigma_1, \bar{r}_2, \sigma_2, f_B$ were varied but constrained to be the same across all maltose concentrations, and A_2 and t_0 were varied separately for each maltose concentration. Occasionally, if f_D,was inconsistent between individual fits of the same experiment, it was held at 0.1 as previously determined (11). Our donor fluorophore was determined to have a single exponential decay lifetime in our MBP constructs. However, the lifetime varied slightly in the absence and presence of maltose. The apo donor-only data were fit with $f_D = 1 \; and \; A_2 = 0$ and three free parameters (τ_{D1}, t_0, f_B), and the holo donor-only data were fit with $f_D = 1 \; and \; A_2 = 1$ and three free parameters (τ_{D2}, t_0, f_B) with. The τ_{D_i} values for the $[Ru(bpy)_2phenM]^{2+}$ and $[Fe(phenM)_3]^{2+}$ experiments were averaged for 6-20 different samples and the average values used in the analysis for all experiments.

To assess the resolvability of parameters and the robustness of non-linear least squares fitting of our above Gaussian distance model to the data, we prepared χ^2 plots for individual parameters (Figure S2A-D). In our χ^2 plots, we held one chosen parameter fixed and systematically varied its value across a suitable range, while allowing all other free parameters in our model to vary. In these plots across all parameters, the χ^2 became minimized around a single value, which always corresponded to our overall minimized model fits. Visually we were able to determine from these plots the range of values for each parameter that still produced reasonable fits, thus providing some confidence range on each parameter. We made these plots for the parameters $f_D, \bar{r}_1, \sigma_1, \bar{r}_2, \sigma_2$, and fraction A_2 under apo and ligand conditions for a representative frequency lifetime dataset. Additionally, we prepared χ^2 surface plots between parameters by systematically varying two fixed parameter values, to get an idea of how certain parameters might be correlated, in particular between f_D and σ_1 and between $f_D$and σ_2 (Figure S2E-F). To ensure that the fits for our model all converge on the same minimized parameter values, we

generated random initial parameter value sets to test as starting points for our fits (Figure S3). In all cases, either the fits could not converge at all (in <10% of starting values), or all converged to nearly identical parameter values. This gave us confidence that the model consistently yields the same minimized values regardless of the initial starting parameter.

Supplemental Figures

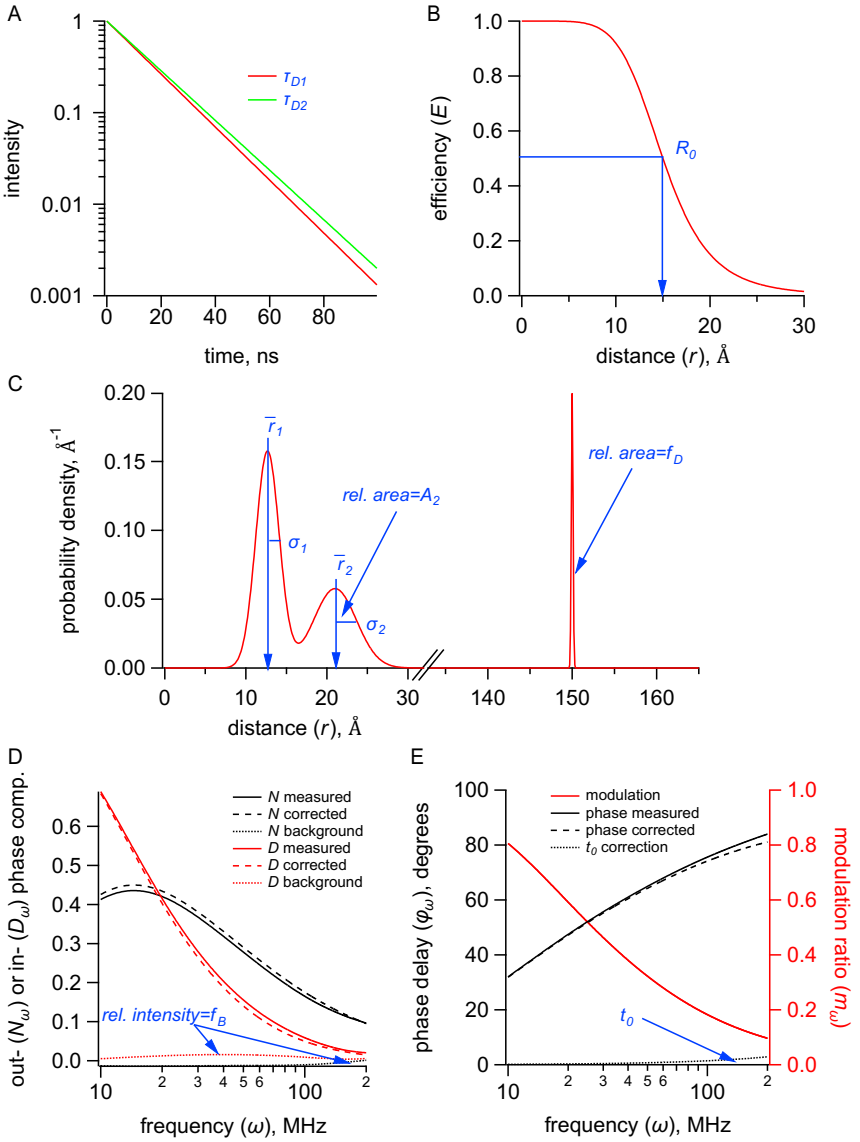

Figure S1. Gaussian model for time-resolved tmFRET. Parameters are in blue. (**A**) Plot of fluorescence lifetimes in the time domain for a single exponential donor fluorophore with time constants τ_{D_1} and τ_{D_2} in the resting and active states respectively. (**B**) Plot of the FRET efficiency (E) as a function of distance (r) showing the characteristic distance for the donor-acceptor pair (R_0). (**C**) Plot of a distribution of donor-acceptor distances ($P(r)$) with two Gaussian components with means ($\bar{r}_1$ and $\bar{r}_2$), standard deviations (σ_1 and σ_2), and fraction active (A_2). The fraction donor only (f_D) was modeled as a narrow Gaussian with a mean distance of 150 Å and a standard deviation of 0.1 Å, too far to exhibit any detectable FRET. (**D**) Plot of the out-of-phase (N_ω) and in-phase (D_ω) components of the measured, corrected, and background fluorescence response as a function of the modulation frequency (ω) where f_B is the fraction of the fluorescence intensity due to background. (**E**) Plot of the phase delay (φ_ω) and modulation ratio (m_ω) of the measured and corrected fluorescence response as a function of the modulation frequency (ω) where t_0. is the time shift of the IRF.

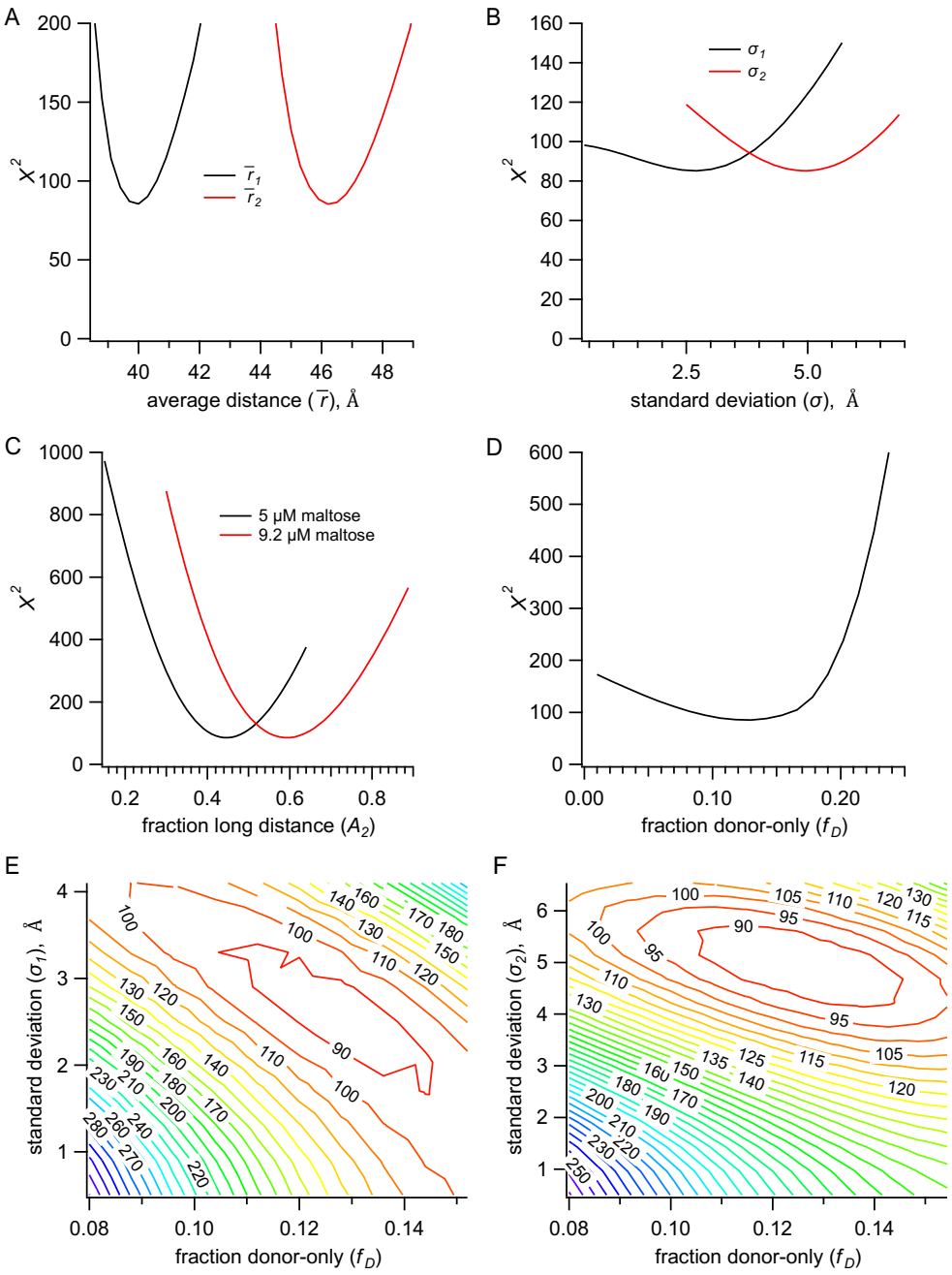

Figure S2. Identifiability of parameters in Gaussian model. (**A-D**) Plots of χ^2 vs Gaussian means ($\bar{r}_1$ and $\bar{r}_2$) (A) and standard deviations (σ_1 and σ_2) (B), fraction active (A_2) in 5 µM and 9.2 µM maltose (C), and fraction donor only (f_D) (D). For each plot, minimum χ^2 was determined by global fitting with the single parameter at different fixed values, while all remaining parameters varied. Results are for a representative dataset from MBP-322Acd-278C with $[Ru(bpy)_2phenM]^{2+}$. (**E,F**) χ^2 surfaces for standard deviations (σ_1 (E) and σ_2 (F)) vs. fraction donor only (f_D) showing some correlation between these parameters in the model. For each plot the standard deviation and fraction donor only were fixed at a range of values and the minimum χ^2 was determined by global fitting. Contour lines are labeled with the minimized χ^2.

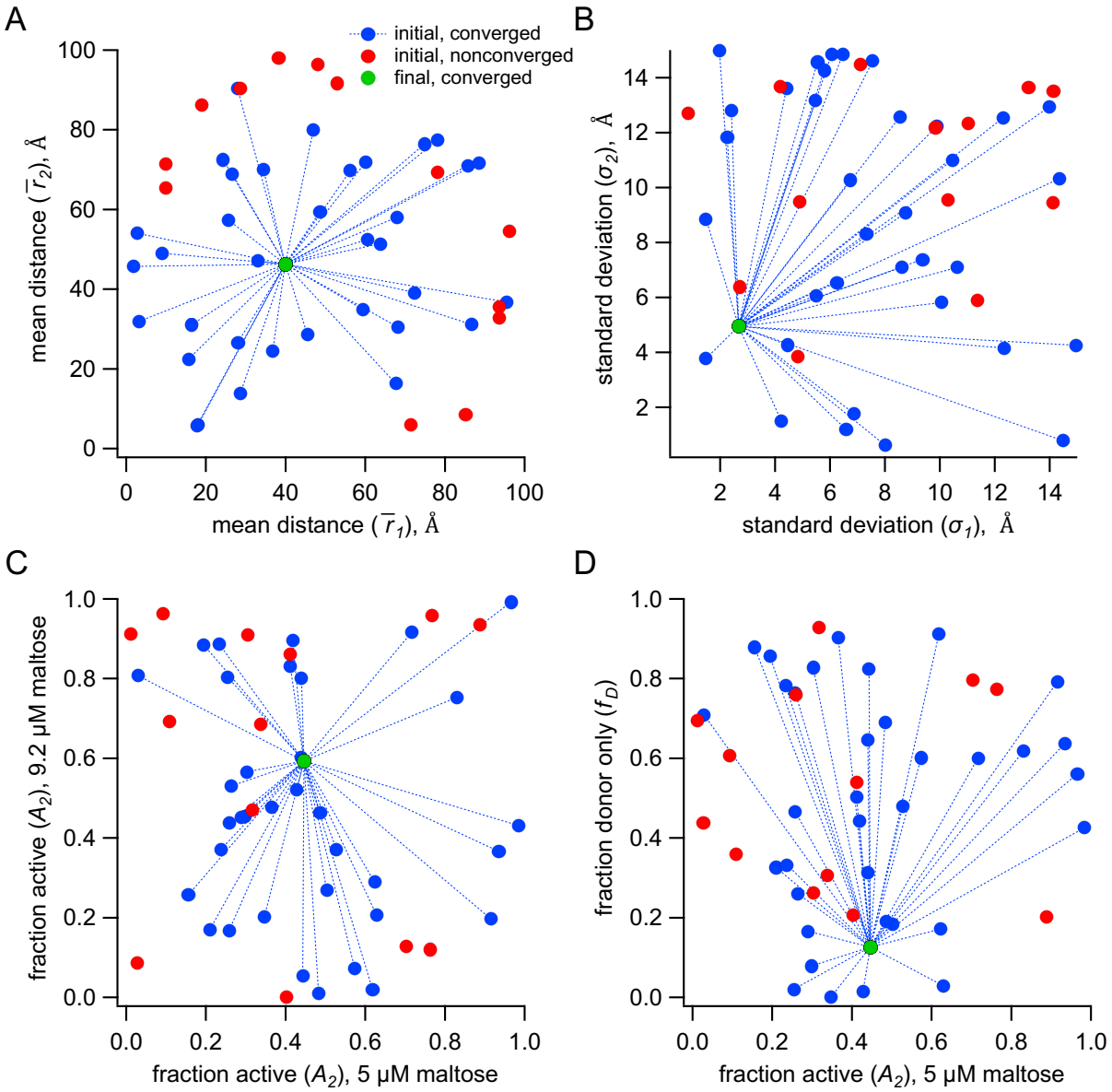

Figure S3. Convergence of the Gaussian model with different initial parameter values. (**A-D**) Plots of the initial values of parameters; $\bar{r}_1$ and $\bar{r}_2$ (A), σ_1 and σ_2 (B), A_2 in 5 µM and 9.2 µM maltose (C), and A_2 in 5 µM and f_D (D); before convergence (blue circles) and after convergence (green circles) for different pairs of parameters. Initial conditions that did not converge or attain a minimum χ^2 less than 3000 are shown in red. For these calculations, the initial values for the shown parameters were varied randomly between the limits indicated by the axes, and global fitting was performed allowing all of the parameters to vary. All initial values in blue converged to nearly identical values for the parameters. Results are for a representative dataset from MBP-322Acd-278C with $[Ru(bpy)_2phenM]^{2+}$.

A

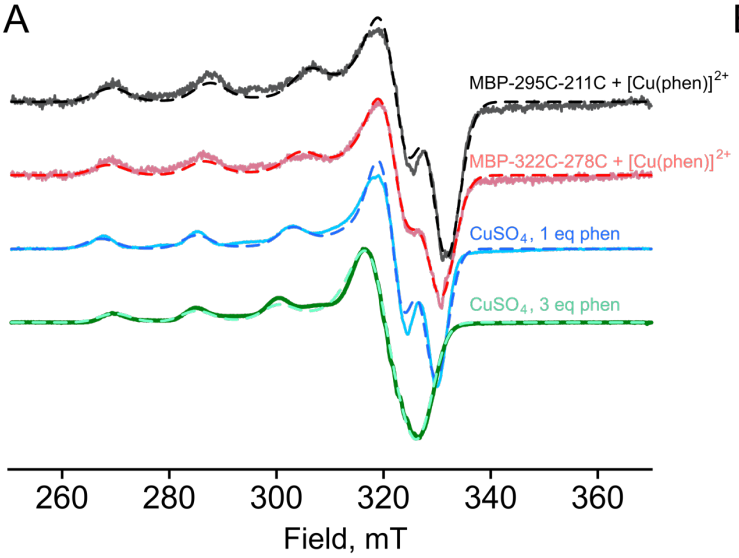

B

	g⊥	A⊥ (MHz)	g‖	A‖ (MHz)
MBP-295C-211C + $[Cu(phen)]^{2+}$	2.059	29	2.239	565
MBP-322C-278C + $[Cu(phen)]^{2+}$	2.060	21	2.249	552
Cu^{2+}:phen (1:1)	2.062	20	2.259	551
Cu^{2+}:phen (1:3)	2.070	21	2.271	473

Figure S4. Cu^{2+} CW EPR. (**A**) X-band CW EPR spectra recorded at 112 K. Spectra are normalized by spectral intensity. Best fit simulations for each spectrum, performed in EasySpin, are shown as dashed curves. (**B**) Table of fitted magnetic parameters g and A from simulations shown in panel A.

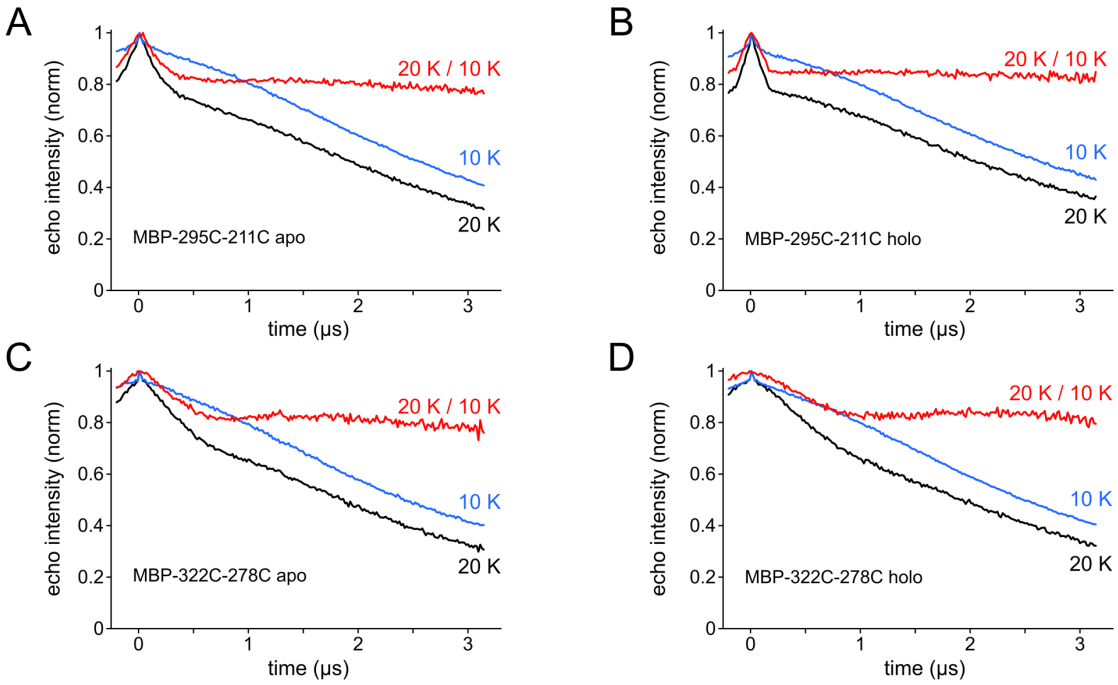

Figure S5. RIDME zero-time artifact removal by division. 5-pulse RIDME time-traces measured at 20 K (black) contained a sharp echo-crossing artifact at $t \approx 0$ that was not removable through phase cycling. RIDME time-traces measured at 10 K (blue) also contain the zero-time artifact, but lack significant dipolar modulation, as the relaxation interval, T_R, is only ~ 4% of the Cu^{2+} T_{1e} at this temperature. Division of the 20 K data set by the 10 K data set removes the zero-time artifact, as well as much of the intermolecular background decay, but preserves the RIDME dipolar modulation (red trace). Data are shown for $[Cu(phenM)]^{2+}$ labeled MBP-295C-211C apo (A), MBP-295C-211C holo (B), MBP-322C-278C apo (C), and MBP-322C-278C holo (D).

Chapter 3: Ligand-Coupled Conformational Changes in the Isolated C-terminal Domains of SthK

Preface

With the success of determining the energetics of MBP using time-resolved tmFRET described in the previous chapter, we wanted to apply this technique to the ligand-mediated allosteric mechanism in the SthK ion channel. This chapter is adapted from the following published work, where I, Pierce Eggan, am the first author:

Eggan, P., Gordon, S. E., & Zagotta, W. N. (2024). Ligand-coupled conformational changes in a cyclic nucleotide-gated ion channel revealed by time-resolved transition metal ion FRET. *eLife*, *13*, RP99854. https://doi.org/10.7554/eLife.99854

Author Contributions

Direct contribution to this work by P. Eggan, myself, include: designing and conducting all experiments, all data analysis, figure preparation, manuscript writing, and data curation.

W.N. Zagotta and S.E. Gordon contributed towards experimental design, conceptualization, data analysis, paper organization, and paper editing.

Abstract

Cyclic nucleotide-binding domain (CNBD) ion channels play crucial roles in cellular-signaling and excitability and are regulated by the direct binding of cyclic adenosine- or guanosine-monophosphate (cAMP, cGMP). However, the precise allosteric mechanism governing channel activation upon ligand binding, particularly the energetic changes within domains, remains poorly understood. The prokaryotic CNBD channel SthK offers a valuable model for investigating this allosteric mechanism. In this study, we investigated the conformational dynamics and energetics of the SthK C-terminal region using a combination of steady-state and time-resolved transition metal ion Förster resonance energy transfer (tmFRET) experiments. We engineered donor-acceptor pairs at specific sites within a SthK C-terminal fragment by incorporating a fluorescent noncanonical amino acid donor and metal ion acceptors. Measuring tmFRET with fluorescence lifetimes, we determined intramolecular distance distributions in the absence and presence of cAMP or cGMP. The probability distributions between conformational states without and with ligand were used to calculate the changes in free energy (ΔG) and differences in free energy change ($\Delta\Delta G$) in the context of a simple four-state model. Our findings reveal that cAMP binding produces large structural changes, with a very favorable $\Delta\Delta G$. In contrast to cAMP, cGMP behaved as a partial agonist and only weakly promoted the active state. Furthermore, we assessed the impact of protein oligomerization and ionic strength on the structure and energetics of the conformational states. This study demonstrates the effectiveness of time-resolved tmFRET in determining the conformational states and the ligand-dependent energetics of the SthK C-terminal region. Time-resolved tmFRET revealed structural and energetic changes induced by ligand binding with full agonist cAMP and partial agonist cGMP in the cyclic nucleotide-binding domain of the bacterial ion channel SthK.

Introduction

CNBD channels, part of the voltage-gated ion channel superfamily, play pivotal roles in sensory perception, signal transduction and cellular excitability (1). The CNBD family includes cyclic nucleotide-gated (CNG) channels, which are responsible for visual and olfactory signal transduction, and hyperpolarization-activated cyclic nucleotide-gated (HCN) channels, which regulate the pacemaker activity of the heart (2–4). Despite their diverse physiological roles, CNBD channels all possess a shared tetrameric structure with four identical or similar subunits surrounding a central ion-conducting pore. Each subunit contains three regions: an N-terminal region, a transmembrane region with a voltage-sensor and pore domain, and a cytosolic C-terminal region that consist of a CNBD plus a C-linker connecting the CNBD to the pore (5). These channels are activated by the binding of cyclic nucleotides (such as cAMP or cGMP) to the CNBD, which induces conformational changes throughout the protein structure to ultimately open the pore. This ligand-induced allosteric opening is still poorly understood, and questions remain about the structural and energetic changes that occur during this allosteric regulation. In particular, what are the energetics of the conformational changes in individual domains, how are these conformational changes coupled within and between subunits, and how do these processes differ for full and partial agonists?

SthK is a prokaryotic member of the CNBD family from *Spirochaeta thermophila,* which has considerable sequence and structural similarity to eukaryotic CNBD channels and offers a powerful model for better understanding the allosteric regulation in these channels (6). It is easily expressed in *E.coli*, has established biochemical purification methods, and its physiological properties have been studied with ion flux assays and patch-clamp electrophysiology (7, 8). We have also characterized a cysteine-free version of the protein (cfSthK) and found it to behave nearly identically to wild-type channels, making it amenable to thiol-based site-specific labeling (7). As previously shown, binding of cAMP to SthK causes robust channel currents in *E.coli* spheroplasts (Figure 1A) with a high degree of cooperativity (Figure 1B; Hill slope, h: 2.9 ± 0.2) (7). In contrast, cGMP appears to be a poor partial agonist for SthK, and its binding to the same structural pocket is only weakly coupled to conformational changes that increase channel open probability (Figure 1B).

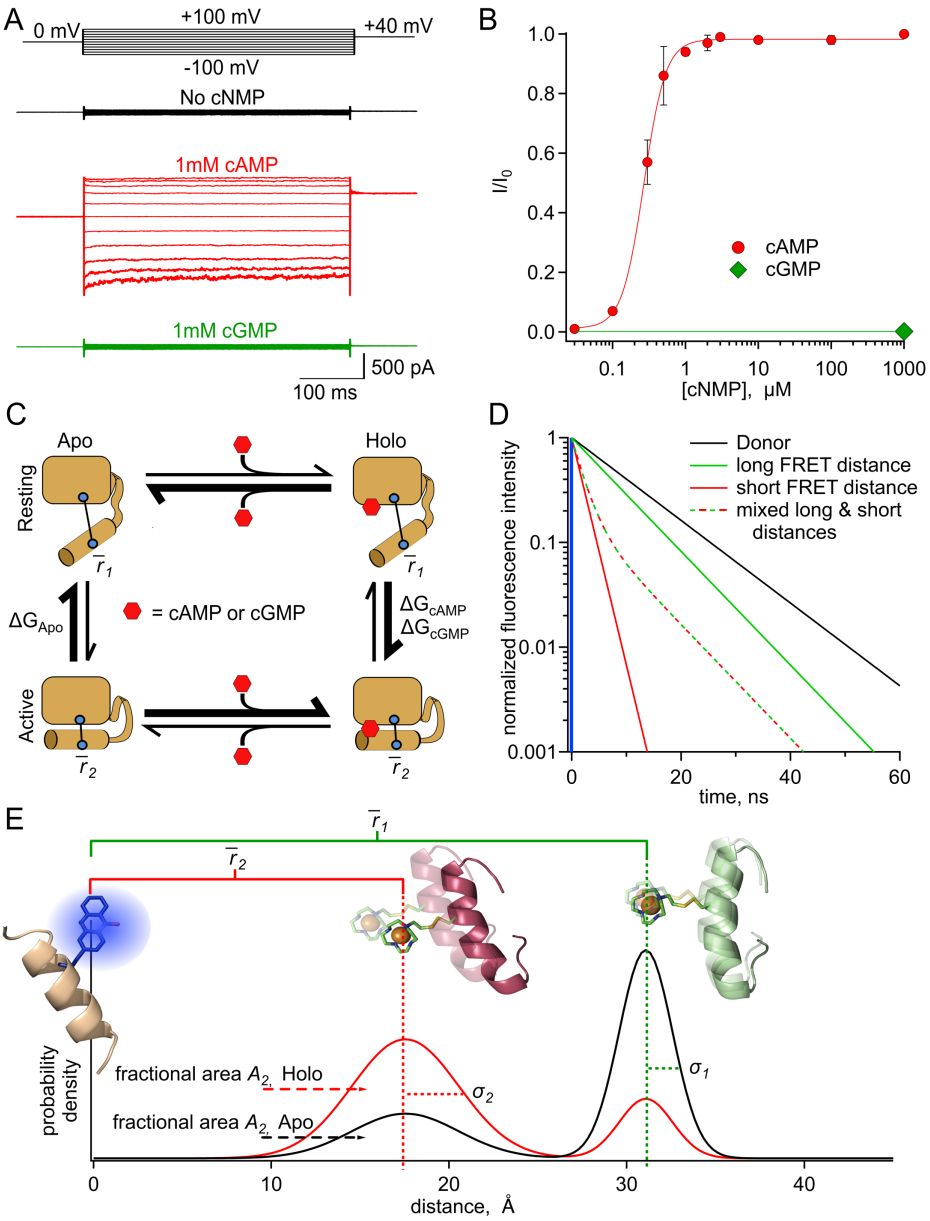

Figure 1. SthK as a model protein for characterizing the allosteric regulation in CNBD channels. **(A)** Representative macroscopic A208V-cfSthK currents in inside-out patches from bacterial spheroplasts in response to voltage steps shown at the top, in the absence of cyclic nucleotide (top black trace), in saturating 1 mM cAMP (middle red trace), and in saturating 1 mM cGMP (bottom green trace). **(B)** Dose-response relation of A208V-cfSthK to cAMP at +80 mV (red circles, n=6), fit with the Hill Equation (in red, $K_{1/2}$: 0.27 ± 0.01 µM, slope: 2.9 ± 0.2, ± SD). Fractional activation by 1 mM cGMP was 0.002 ± 0.003 (± SD) (green diamond, n=6). **(C)** State diagram showing four states (either apo or holo, and either resting or active) of the CNBD and the associated ΔG's for the transitions between states. **(D)** Theoretical fluorescence lifetime decays of a donor fluorophore in the time-domain showing basis of time-resolved tmFRET. A single exponential donor and mixtures of two single tmFRET distances (short and long) are shown. **(E)** Theoretical distance distributions showing two states with average distances, $\bar{r}$, heterogeneity within each conformational state as standard deviation, σ, and heterogeneity between conformational states as fractional area A_2 for apo (black) and holo (red).

X-ray crystallography and cryo-EM structures of SthK reveal notable ligand-induced structural changes throughout the protein, particularly in the CNBD (9–11). These differences include a rotation of the CNBD C-helix towards the β-roll upon binding of cyclic nucleotide. This important conformational change is thought to be coupled to a rearrangement of the C-linker, and ultimately to the opening of the pore. However, structures alone have not been able to fully characterize the energetic landscape of the allosteric regulation, especially in determining the structural heterogeneity within conformational states and the energetics between states.

To link structural information to the mechanism of allostery, we used a simple four-state model to describe the conformational states and energetics in the C-terminal of SthK (Figure 1C). This framework has been used previously to describe allosteric proteins generally and the ligand-binding domains of CNBD channels in particular (12–17). In this model, the CNBD can exist in either resting or active conformational states, both of which can be ligand free (apo) or ligand bound (holo). Whereas in the absence of ligand the transition from resting to active is unfavorable, the presence of agonist (either full or partial) makes the active state more favorable. The equilibrium constants, and therefore energetics, that describe the transitions between states determine the steady-state fraction of molecules in each given state. Using the four-state energetic model as a framework and an experimental method for determining the fraction of molecules in each state, we can calculate the changes in free energy (ΔG) and differences in energy change (ΔΔG) between the conformational states of the CNBD upon binding of ligands like cAMP and cGMP.

A complex protein, such as an ion channel, consists of multiple domains, each of which can undergo conformational changes that are coupled to ligand binding, transmembrane voltage, or the state of a neighboring domain (18, 19). For example, allostery in CNBD channels can be modeled as a cyclic nucleotide-dependent conformational change in each subunit CNBD that is coupled to a concerted conformational change in the C-linker, which in turn is coupled to a opening conformational change in the pore (1, 12). In this context, to truly understand the allosteric mechanism in CNBD channels, we would need to know ΔG and ΔΔG for each of these domains. Therefore, we need a method that can measure the conformational energetics in each protein domain.

In this study, we utilized our recently described steady-state and time-resolved tmFRET methods to measure the energetics in an isolated C-terminal fragment of SthK (20–22). In tmFRET, a donor fluorophore is paired with a transition metal ion, such as Cu^{2+}, Fe^{2+}, or Ru^{2+}, as an acceptor. Donor-acceptor pairs can then be incorporated in a protein at different residue positions. As in classical FRET with two fluorophores, the efficiency of energy transferred between the donor fluorophore and acceptor metal ion is steeply distance dependent and can be used as a molecular ruler to measure distances between sites on a protein, and therefore conformational changes (23).

In time-resolved tmFRET, changes in fluorescence lifetimes of the donor fluorophore are quantified to report FRET efficiencies, and therefore molecular distances between the donor and acceptor. The fluorescence lifetime is the time, in nanoseconds, between excitation of the donor fluorophore and emission of a photon (23). Unlike steady-state FRET, time-resolved FRET can provide nanosecond snapshots of the distribution of FRET efficiencies in a sample (20, 22). In the time-domain, a histogram of photon latencies for the simplest lifetimes appears as a single exponential decay (Figure 1D, black line). FRET resulting from a single donor-acceptor distance also produces lifetimes described by a single exponential decay, but with a time constant that decreases in proportion to the FRET efficiency (Figure 1D, solid green and red lines). However, in the case of two donor-acceptor distances, such as from two protein conformations, the intensity decay will be double exponential, with contributions from both donor-acceptor distances. The average distance of each component and the fraction among components can be determined by fitting the decay with a double-exponential decay model. The fractional contribution of each lifetime represents the prevalence of each distance, and thus conformational state, in the sample population (Figure 1D, green-red dashed lifetime is a mix of 20% solid green and 80% solid red lifetimes) (23). Time-resolved tmFRET, therefore, resolves the structural distances and relative abundance of multiple conformational states in a protein sample.

Under physiological conditions, donor-acceptor distances in proteins will typically be heterogeneous and fluorescence lifetime data will reflect this heterogeneity. Thus, we have fit lifetime data with a FRET model that assumes Gaussian distributions of donor-acceptor distances within each state. This heterogeneity can arise from both: 1) backbone and rotameric variations within a given state (the width of each peak, Figure 1E) and 2) differences between

conformational states (relative fraction of the resting, black, and active, red, peaks, Figure 1E). Heterogeneity between conformational states reflects the proportion of molecules in the resting and active states of the protein, which can then be used to calculate the free energy difference between the states (ΔG). In this study, we used various donor-acceptor pairs in the CNBD of SthK to measure distance distributions of the C-helix relative to the β-roll in the absence and presence of ligand. Distance distributions were used to determine the energetics for the transitions between conformational states of the four-state model described above. These results provide a more complete understanding of the structural and energetic changes in the CNBD with ligand binding.

Results

We engineered three donor sites for tmFRET experiments into a C-terminal fragment of SthK ($SthK_{C\text{-}term}$), comprised of the C-linker and CNBD domains (9). At these sites (359, 361 and 364), we introduced the unnatural amino acid acridon-2-ylalanine (Acd) as a donor fluorophore using amber codon suppression with a previously described tyrosyl tRNA synthetase (22, 24). Incorporation of Acd into stop-codon containing $SthK_{C\text{-}term}$ constructs occurred only in the presence of both the amino-acyl tRNA synthetase/tRNA plasmid (RS/tRNA) and the Acd amino acid. SDS-PAGE followed by in-gel fluorescence imaging ($SthK_{C\text{-}term}$-S361-TAG) indicated that Acd was site-specifically incorporated into our $SthK_{C\text{-}term}$ constructs and the incorporated product was readily purified for use in tmFRET experiments (Figure 2A).

We introduced metal ion acceptor binding sites for tmFRET using cysteine mutations in $SthK_{C\text{-}term}$ for modification with cysteine-reactive metal chelators (TETAC and phenanthroline maleimide (phenM)) bound to different transition metals (Cu^{2+}, Fe^{2+}, and Ru^{2+}). The three different metal ion-acceptor complexes used in this study, $[Cu(TETAC)]^{2+}$, $[Fe(phenM)_3]^{2+}$, and $[Ru(bpy)_2phenM]^{2+}$, are shown in Figure 2B. The distance dependence of energy transfer between donor and acceptor is described by the Förster equation and is dependent on the overlap between the absorbance spectrum of the acceptor and the emission spectrum of the donor, among other factors (23, 25). Paired with Acd, these transition metal acceptor complexes resulted in distances with 50% energy transfer (R_0) at 15.6 Å, 41.8 Å, 43.5 Å for $[Cu(TETAC)]^{2+}$, $[Fe(phenM)_3]^{2+}$, and $[Ru(bpy)_2phenM]^{2+}$, respectively. Thus, with Acd as a donor, these acceptors

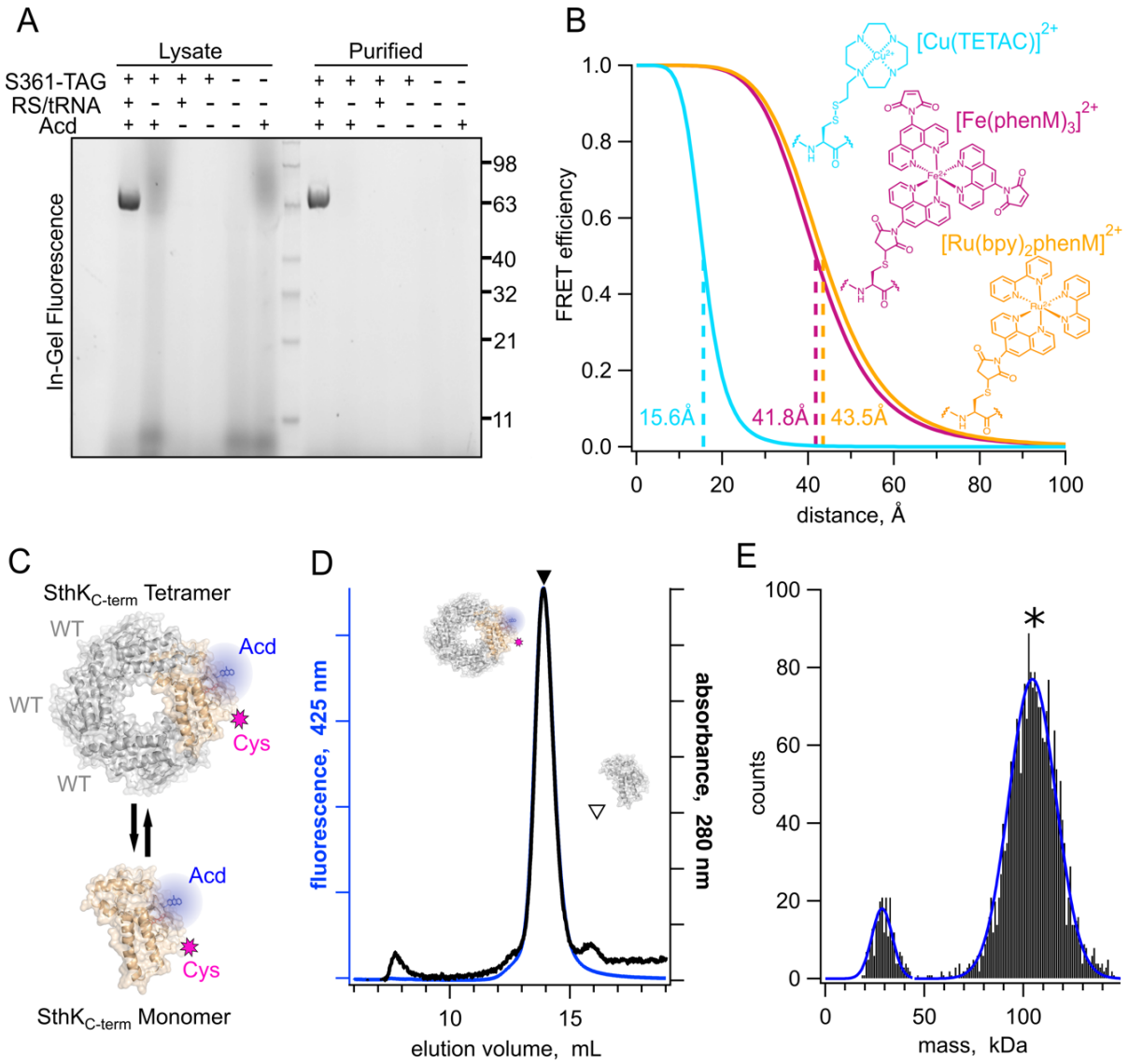

Figure 2. Expression, purification, and tetrameric analysis of $SthK_{C\text{-}term}$. **(A)** In-gel protein fluorescence showing selective Acd incorporation into $SthK_{C\text{-}term}$ in the absence and presence of S361Acd TAG site, Acd aminoacyl tRNA synthetase/tRNA (RS/tRNA), and unnatural amino acid Acd. **(B)** Structures of cysteine modified by acceptor compounds $[Cu(TETAC)]^{2+}$ (cyan), $[Fe(phenM)_3]^{2+}$ (magenta), and $[Ru(bpy)_2phenM]^{2+}$ (orange) along with their corresponding Förster curves of FRET efficiency as a function of distance from Acd, and their R_0 values specified and marked with dashed lines. **(C)** $SthK_{C\text{-}term}$ cartoon as tetramer and monomer showing WT subunits in gray and cysteine-containing Acd-labeled subunits in orange. **(D)** SEC traces (absorbance at 280 nm in black and 425 nm fluorescence emission for Acd in blue) of isolated WT-Acd-heterotetrameric protein (closed triangle) vs monomeric WT protein (open triangle). **(E)** Mass photometry histogram data showing primarily tetramers, with single Gaussian fits (blue, 29 kDa ± 7.3 and 104.5 kDa ± 16.8, ± SD).

allowed us to measure both short (10-20 Å) and long distances (25-50 Å) across $SthK_{C\text{-}term}$ (Figure 2B) (21).

The $SthK_{C\text{-}term}$ fragment tetramerizes in solution at higher protein concentrations, even though the transmembrane domains are absent. Although the tetrameric structure is the physiologically relevant state for the channel, tetramerization introduces challenges in minimizing the contribution of inter-subunit FRET measurements where only intra-subunit donor-acceptor pairs are desired. Using tmFRET, which is sensitive to relatively short distances, mitigates but does not eliminate this concern. To avoid potential contributions from inter-subunit FRET, Acd-labeled protein was tetramerized with an excess (at least a 3:1 molar ratio) of wild-type $SthK_{C\text{-}term}$ protein (WT; Figure 2C). WT protein had neither Acd incorporation nor cysteine mutations. This approach ensured that, on average, only one (or fewer) Acd-cysteine-containing subunit was present in each tetramer, and our FRET efficiency measurements would be almost exclusively from donor-acceptor pairs within the same subunit.

Tetrameric $SthK_{C\text{-}term}$ was efficiently separated from monomeric protein using size exclusion chromatography (SEC), where tetrameric protein eluted primarily as a single monodispersed peak at 14 mL, as observed by both absorbance at 280 nm and Acd fluorescence (Figure 2D, closed triangle). We confirmed this large SEC peak corresponded to tetramers of $SthK_{C\text{-}term}$ using mass photometry, which reported a mass of ~105 kDa, compared to a predicted mass of 101 kDa (Figure 2E). At the low concentrations (~10nM) used for mass photometry, a second small peak was observed of ~30kDa, which is below the analytical range for this method. All tmFRET experiments used higher protein concentrations to ensure tetramerization.

Steady-State tmFRET for Determining Weighted-Average Distance Changes

To resolve the structural changes in tetrameric $SthK_{C\text{-}term}$, we characterized steady-state tmFRET using $SthK_{C\text{-}term}$-S361Acd-V416C, with a long-distance donor-acceptor pair (Figure 3A), and $SthK_{C\text{-}term}$-Q364Acd-R417C, with a shorter distance pair (Figure 3C). We used the metal ion acceptors $[Fe(phenM)_3]^{2+}$ and $[Ru(bpy)_2phenM]^{2+}$ for the long-distance pair and $[Cu(TETAC)]^{2+}$ for the short-distance pair. We measured time courses of Acd fluorescence intensity of the cysteine-containing construct, upon addition of the acceptor, relative to protein without the cysteine mutation, measured separately as a negative control. We plotted the ratio of the normalized fluorescence intensity for the two protein samples as $F_{Cys}/F_{No\ Cys}$. The addition of

metal acceptor produced pronounced quenching specifically in the cysteine-containing constructs (Figure 3A,B,C). This fluorescence decrease is indicative of FRET-based quenching of the donor by the metal acceptor, with the FRET efficiency given by $E = 1- F_{Cys}/F_{No\ Cys}$. The addition of a saturating concentration of cAMP (160 μM) further increased quenching, indicating a greater FRET efficiency in the presence of agonist compared to the apo state. The increased FRET is consistent with a cAMP-induced decrease in donor-acceptor distance as the C-helix moves towards the β-roll. The dependence of the apparent FRET efficiency change on the cAMP concentration was measured for each donor-acceptor pair, then normalized for comparison and fit with the Hill equation (Figure 3D). The Hill fits obtained from different sites and acceptor metals are in close agreement with one another, suggesting similar binding affinities and that our previous measurements were obtained at saturating concentrations. Additionally, the three Hill fits with slopes, *h*, ~1 suggest that the cooperativity observed in full-length channel electrophysiology is not observed in the isolated C-terminal fragment. These steady-state tmFRET results across different donor-acceptor sites and acceptor complexes underscore the large conformational change of the C-helix induced by cAMP.

In addition to measuring the conformational rearrangement with the full agonist cAMP, we also used the partial agonist cGMP. Like cAMP, cGMP increased quenching by our transition metal labels (i.e., increased FRET); however, the increase was much smaller than that produced by cAMP. As discussed above, cGMP is a poor partial agonist of SthK which elicits only a small fraction of the channel current elicited by cAMP (Figure 1A). The cGMP-induced increase in FRET we observed provides further evidence that cGMP indeed binds to SthK and that cGMP binding causes a conformational change that moves the C-helix closer to the β-roll. These data do not, however, distinguish between 1) cGMP producing a smaller movement relative to cAMP (a distinct state), and 2) cGMP producing the same size movement but with a lower fraction in the active state (different energetics).

At lower protein concentrations, monomeric $SthK_{C\text{-}term}$ protein can be separated from tetrameric protein on SEC. Interestingly, for multiple donor-acceptor sites, steady-state tmFRET measurements consistently revealed higher FRET efficiencies (shorter distances) for monomers than for tetramers, particularly in the apo state (Figure 3—figure supplement 1). These experiments suggest that tetramerization destabilizes the resting-to-active transition of the

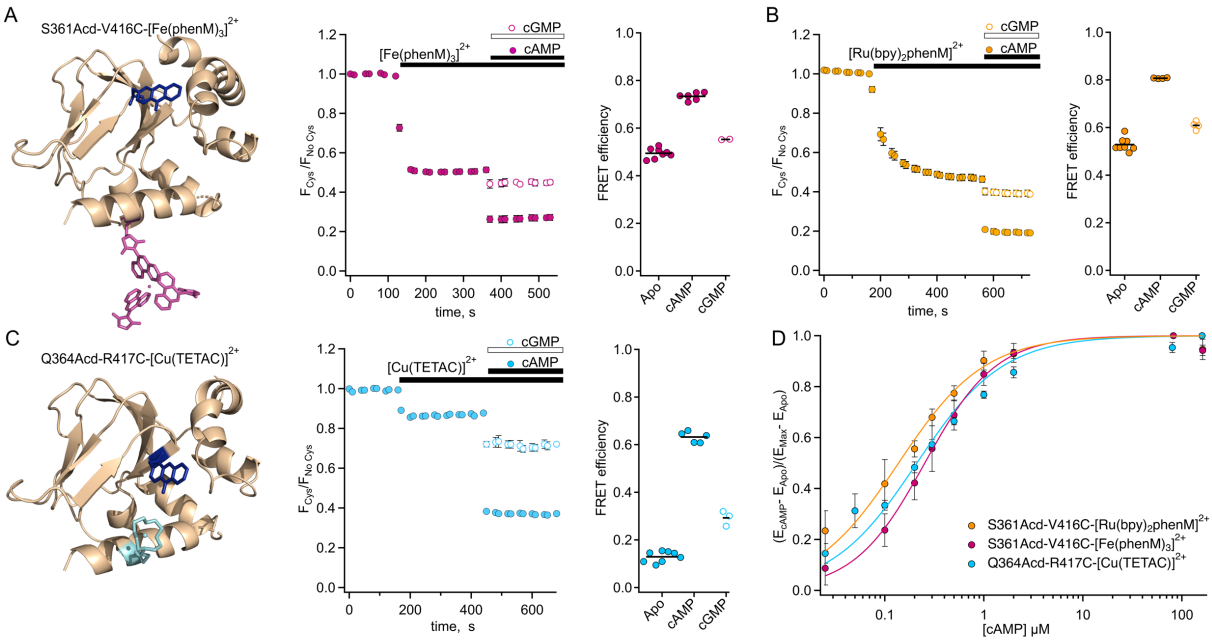

Figure 3. Steady-state tmFRET data from tetrameric $SthK_{C\text{-}term}$. **(A)** Left: structure of one subunit of $SthK_{C\text{-}term}$-S361Acd with $[Fe(phenM)_3]^{2+}$ acceptor incorporated at V416C (adapted from PDB: 4D7T) (9). Middle: averaged fluorescence time course upon addition of $[Fe(phenM)_3]^{2+}$ and then cAMP or cGMP (apo, n=8; cAMP n=6; and cGMP, n=2). Right: summary of the FRET efficiencies from individual experiments, with mean values as horizontal lines. **(B)** Left: Average fluorescence time course for same site upon addition of $[Ru(bpy)_2phenM]^{2+}$ acceptor and then cAMP or cGMP (apo, n=8; cAMP, n=4; and cGMP, n=4). Right: summary of FRET efficiencies, with mean values as horizontal lines. **(C)** Left: structure of one subunit of $SthK_{C\text{-}term}$-Q364Acd-417C with $[Cu(TETAC)]^{2+}$ acceptor incorporated at R417C. Middle: averaged fluorescence time course upon addition of $[Cu(TETAC)]^{2+}$ then cAMP or cGMP (apo, n= 8; cAMP, n=5; and cAMP, n=3). Right: summary of FRET efficiencies, with mean values as horizontal lines. **(D)** Dose response relations of FRET efficiency change as a function of cAMP concentration normalized for comparison and fit with Hill equations ($K_{1/2}$: 0.25 ± 0.01 µM , 0.14 ± 0.01 µM, 0.21 ± 0.02 µM, and h:1.2 ± 0.07, 1, and 1 for $[Fe(phenM)_3]^{2+}$, magenta; $[Ru(bpy)_2phenM]^{2+}$, orange; and $[Cu(TETAC)]^{2+}$, cyan respectively, ± SD).

$SthK_{C\text{-}term}$ protein. For our remaining experiments, we focused on the conformational changes in the tetrameric state of the protein, which is more physiologically relevant.

Predicted *In-Silico* Distance Distributions

To validate the accuracy of tmFRET in determining donor-acceptor distances and ligand-dependent changes in distances, we compared our data to predictions based on structural models. For each donor-acceptor pair, we modelled the donor and acceptor labels on the resting and active static structures of $SthK_{C\text{-}term}$ (PDB: 7RSH and 4D7T, respectively) to obtain *in-silico* weighted rotameric ensembles utilizing a previously described python package, chiLife (Figure 4A) (9, 11, 26). We then calculated the distance distributions between every Acd rotamer and every acceptor rotamer for both the resting and the active structures within subunits (intra-subunit) and between all other subunits (inter-subunit) (Figure 4B). The inter-subunit distances predicted by chiLife for these sites were longer than 50 Å, contributing less than 15% FRET efficiency to the intra-subunit FRET in either the resting or active states. This inter-subunit FRET is predicted to be negligible in our experiments with added WT $SthK_{C\text{-}term}$.

We compared the intra-subunit chiLife distributions with our measured weighted-average distances predicted from steady-state tmFRET experiments. We calculated the distances from our steady-state FRET experiments using the Förster equation (25) and superimposed them on the distributions from chiLife (Figure 4B, vertical solid black and red lines). Whereas the distance changes based on our tmFRET measurements were generally similar to the structural predictions, the absolute distances differed by as much as 5 Å. Steady-state tmFRET measurements combine several sources of heterogeneity from the protein into a single weighted average, including the presence of mixed populations of resting and active states. An additional source of uncertainty is the labeling efficiency. If, for example, we assume that 10% of the protein sample in steady-state experiments was not labeled with acceptor (e.g., due to cysteine oxidation), the adjusted weighted-average distances from our experimental data become more similar to predicted peak values (vertical dashed black and red lines). Although overall these average distances are close to the expected distances predicted by the structures, a method for measuring the distance distributions would be desirable.

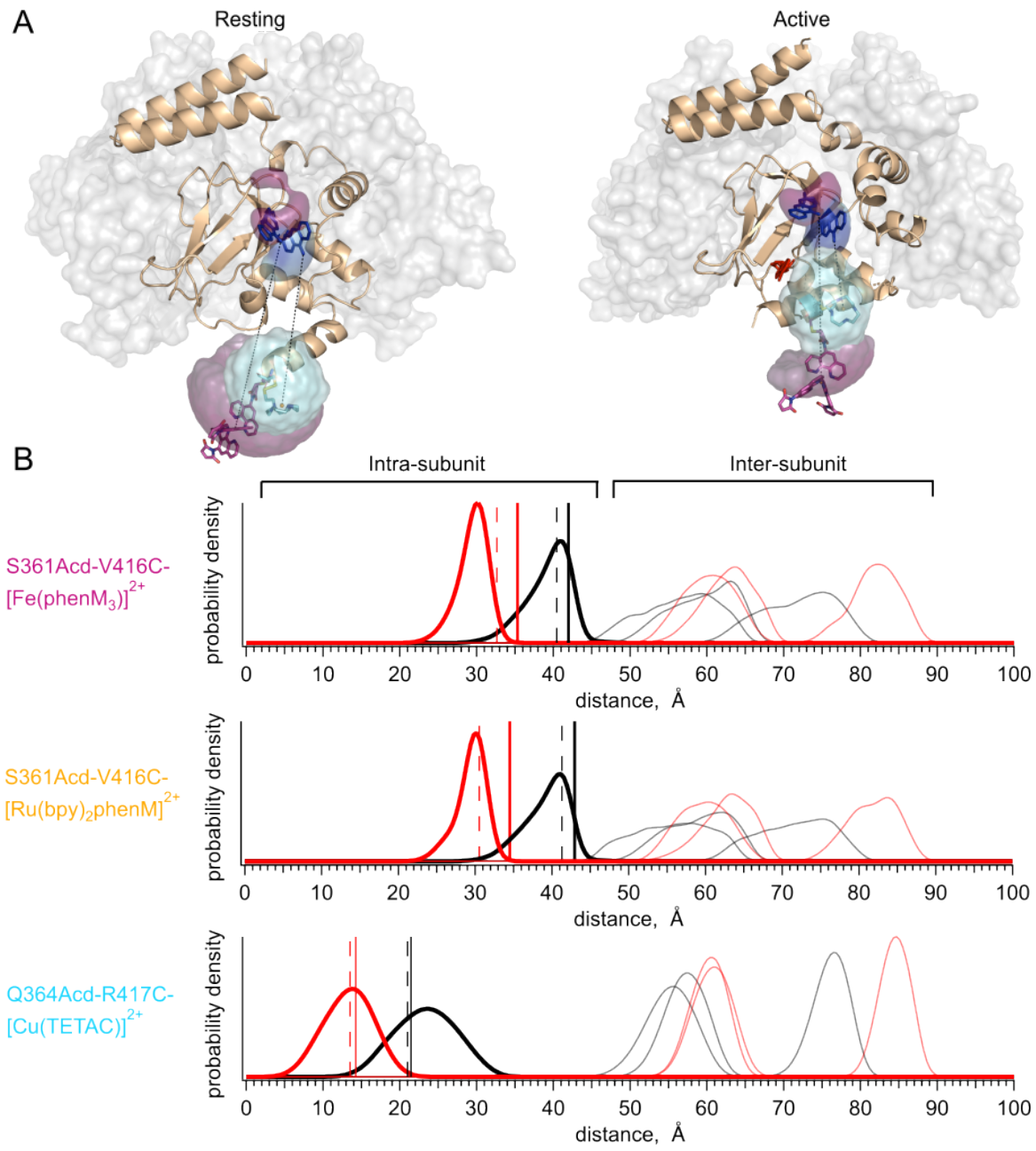

Figure 4. Distance distribution predictions with chiLife. **(A)** Structure of resting state (left, PDB:7RSH) (11), and cAMP-bound active state (right, PDB:4D7T) (9) with rotameric clouds predicted by chiLife for the labels (Acd, blue; $[Fe(phenM)_3]^{2+}$, magenta; and $[Cu(TETAC)]^{2+}$, cyan). Gray surface indicates location of adjacent WT subunits in tetramer. **(B)** Distance distributions predicted by chiLife for $SthK_{C\text{-}term}$-S361Acd-V416C-$[Fe(phenM)_3]^{2+}$, $SthK_{C\text{-}term}$-S361Acd-V416C-$[Ru(bpy)_2phenM]^{2+}$ and $SthK_{C\text{-}term}$-Q364Acd-R417C-$[Cu(TETAC)]^{2+}$ (intra-subunit distances: resting, black curves; active, red curves; and inter-subunit distances: resting, grey curves; active, pink curves). Average steady-state tmFRET distance measurements are overlayed as vertical lines for data from Figure 3 (apo, solid black, and cAMP, solid red) and adjusted assuming a 10% unlabeled protein (dashed black and red vertical lines).

Time-Resolved tmFRET for Determining Distance Distributions

While steady-state tmFRET shows an *average* FRET efficiency (and weighted-average distance) for all the molecules in the sample, time-resolved measurements of fluorescence lifetimes can be used to measure distance *distributions* in the sample. This approach can account for the two forms of heterogeneity in the protein mentioned earlier (within state and between state heterogeneity), as well as protein not labeled with acceptor. Here, we measured fluorescence lifetimes in the frequency-domain, which can obtain distance distributions utilizing the same principles discussed above for time-domain lifetime measurements (Figure 1D). Instead of measuring donor emission photons in response to an impulse of excitation light, lifetimes in the frequency-domain quantify the phase shift (phase delay) and decrease in amplitude of response (modulation ratio) of the donor emission as functions of the modulation frequency of a sinusoidally-varying excitation light (22).

We first measured the fluorescence lifetime of $SthK_{C\text{-}term}$-S361Acd-V416C in the absence of acceptor. The phase delay and modulation ratio as a function of the modulation frequency of the excitation light are shown as gray symbols in the Weber plot of Figure 5A. We fit these data with a model for a single exponential lifetime with a time constant of 17.2 ± 0.01 ns (n=8, Figure 5A, grey curves), comparable but a little longer than values seen previously for Acd (~16 ns) (22, 27). When $[Fe(phenM)_3]^{2+}$ was added to the protein sample, the average fluorescence lifetime decreased, illustrated by a shift in the phase delay and modulation ratios to higher frequencies in the Weber plot (Figure 5A, black circles). Adding a saturating concentration of cAMP (1.23 mM), further decreased the average lifetime, indicating increased FRET (Figure 5A, red circles). This change in lifetime is consistent with steady-state measurements and reflects a decreased distance between the C-helix and the β-roll. In contrast, adding a saturating concentration of cGMP (1.23 mM) instead of cAMP only moderately decreased the fluorescence lifetime, with phase delay and modulation ratio curves falling closer to the apo conditions (Figure 5A, green circles).

To further validate our lifetime measurements using a different acceptor with a different R_0, we repeated these experiments using $[Ru(bpy)_2phenM]^{2+}$ as the acceptor instead of $[Fe(phenM)_3]^{2+}$. $[Ru(bpy)_2phenM]^{2+}$ also decreased the average fluorescence lifetime in all three conditions (apo, cAMP and cGMP) relative to the donor-only lifetime (Figure 5B). As expected

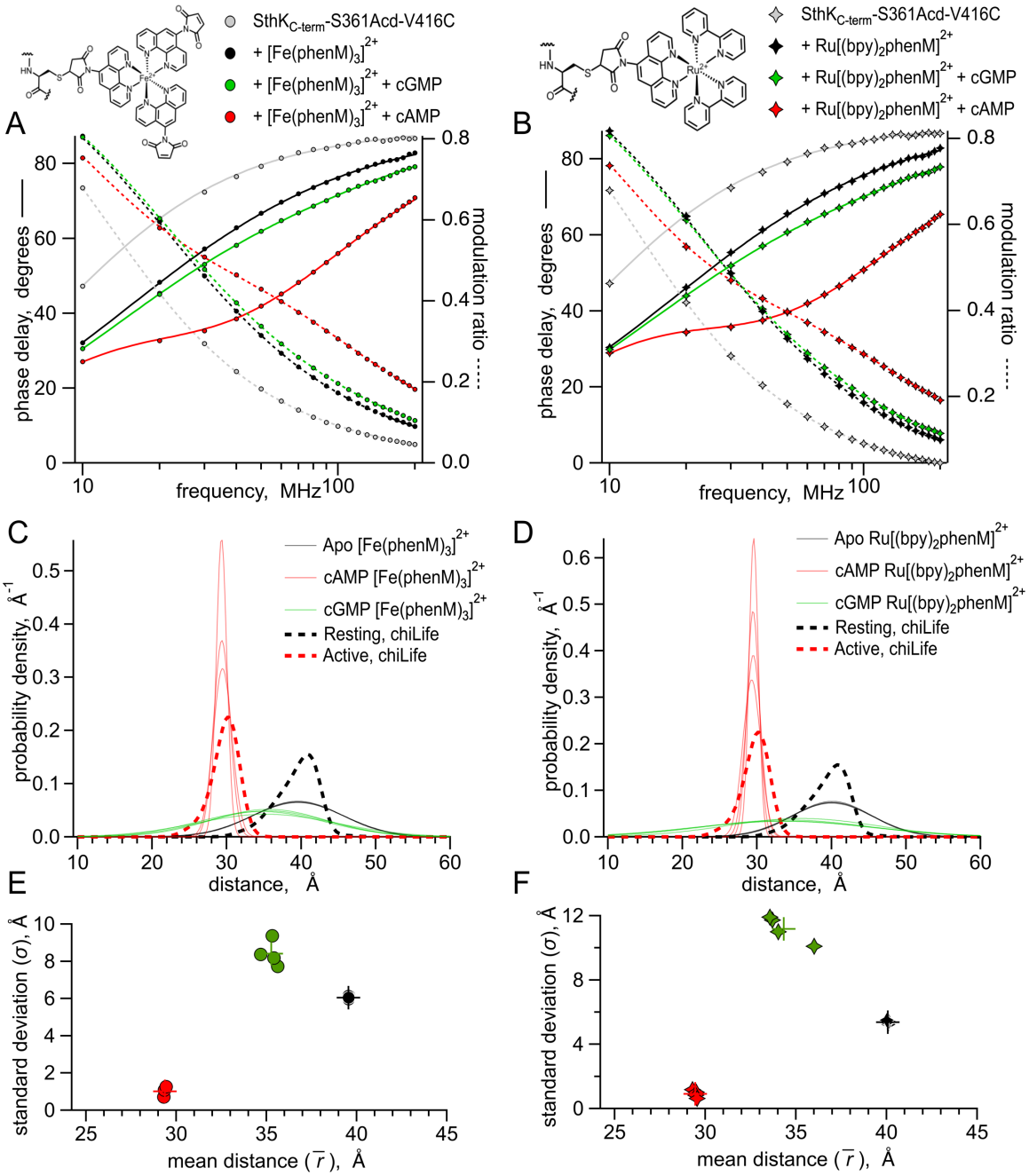

Figure 5. Lifetime measurements of SthK$_{C\text{-}term}$-S361Acd-V416C with [Fe(phenM)$_3$]$^{2+}$ and [Ru(bpy)$_2$phenM]$^{2+}$. Chemical structures of acceptors and legends for all plots shown on top. **(A-B)** Representative Weber plots of phase delay and modulation ratio for SthK$_{C\text{-}term}$-S361Acd-V416C labeled with [Fe(phenM)$_3$]$^{2+}$ (A) and [Ru(bpy)$_2$phenM]$^{2+}$(B). Fits of the data using the single Gaussian model are shown with phase delay as solid curves and modulation ratio as dashed curves. **(C-D)** Spaghetti plots showing distance distributions from the model fits with apo (thin black curves, n=4), with 1.23 mM cAMP (thin red curves, n=4) and 1.23 mM cGMP (thin green curves, n=4) for [Fe(phenM)$_3$]$^{2+}$ (C) and [Ru(bpy)$_2$phenM]$^{2+}$(D). Distributions predicted by chiLife are overlayed in dashed curves. **(E-F)** Summary of Gaussian fit standard deviations, σ, versus average distances, $\bar{r}$, for [Fe(phenM)$_3$]$^{2+}$ (E) and [Ru(bpy)$_2$phenM]$^{2+}$ (F), with average values as cross marks.

from the longer R_0 value for Acd-$[Ru(bpy)_2phenM]^{2+}$ compared to Acd-$[Fe(phenM)_3]^{2+}$, $[Ru(bpy)_2phenM]^{2+}$ produced an even greater shift in phase delay and modulation ratio towards higher frequencies compared to $[Fe(phenM)_3]^{2+}$ (Figure 5B, 6B). Neither $[Fe(phenM)_3]^{2+}$ nor $[Ru(bpy)_2phenM]^{2+}$ produced a change in lifetime for $SthK_{C\text{-}term}$-S361Acd (without the cysteine) used as a negative control (Figure 5—figure supplement 1). The decreases in lifetimes of $SthK_{C\text{-}term}$-S361Acd-V416C with the metal acceptors and ligands reflect measurable decreases in the donor-acceptor distances (i.e., conformational state) with the addition of cyclic nucleotide, as seen with the steady-state tmFRET measurements.

To obtain distance distributions and average distances that reflect individual conformational states, we fit our lifetime data to a previously described model that assumes each ligand condition (apo, cAMP and cGMP) is described by a single Gaussian distribution of distances (parameters in Figure 5—figure supplement 2) (20). The $[Fe(phenM)_3]^{2+}$ and $[Ru(bpy)_2phenM]^{2+}$ time-resolved tmFRET datasets for each ligand condition were individually fit using this lifetime model (solid and dashed curves, Figure 5A and B) (20, 22). The average distances ($\bar{r}$) and standard deviations (σ) of the Gaussian distance distributions from these fits are shown for $[Fe(phenM)_3]^{2+}$ and for $[Ru(bpy)_2phenM]^{2+}$ as spaghetti plots experiments in Figures 5C, and 5D, respectively. Overlayed on the spaghetti plots are the distance distributions for the resting and active states predicted using chiLife (dashed curves). The $\bar{r}$ and σ of the lifetime model from individual experiments for apo, cAMP and cGMP are summarized in Figure 5E and F. Average Gaussian distances measured from experiments for apo and cAMP using both $[Fe(phenM)_3]^{2+}$ (apo= 39.6 Å, cAMP= 29.4 Å) and $[Ru(bpy)_2phenM]^{2+}$ (apo= 40.1 Å, cAMP= 29.4 Å) agreed remarkably well with the chiLife predictions and with each other despite the difference in R_0 between $[Fe(phenM)_3]^{2+}$ and $[Ru(bpy)_2phenM]^{2+}$. Interestingly, the cGMP data had an $\bar{r}$ distance between the apo and cAMP $\bar{r}$ values and had a much wider σ, spanning a distance range of the apo and cAMP Gaussians combined.

While this lifetime model, with a single average distance for each ligand condition, fits the time-resolved tmFRET data well, it seems likely that there might be more than one conformational state (resting and active) present for each ligand condition (12). As our four-state model suggests, each liganded condition (apo, cAMP and cGMP) should be comprised of a mixture of resting and active conformational states at varying proportions. For example, the wide

cGMP Gaussian positioned between those of the apo and cAMP distributions might reflect the sum of two Gaussians, one with a longer average distance (resting conformation) and one with a shorter average distance (active conformation). The larger apo state σ compared to the chiLife prediction could also be due to the presence of a small fraction of the active state, even without ligand. Determining the fractional occupancy among the resting and active states in the apo, cAMP and cGMP conditions would provide energetic information about the transition between resting and active $SthK_{C\text{-}term}$ in the different conditions.

Global Fitting $[Fe(PhenM)_3]^{2+}$ and $[Ru(Bpy)_2PhenM]^{2+}$for Energetic Information

Our approach to measuring fluorescence lifetimes also provides a model-independent way to visually estimate the probability distribution among resting and active states using a representation of the data known as a phasor plot. Phasor plots show the in-phase (*D*) and out-of-phase (*N*) components that underlie the phase delays and modulation ratios shown in the Weber plots (28). The location of the data on the phasor plot allows us to view complex lifetimes without assumptions about the shape of the distance distributions.

The phasor plot for $SthK_{C\text{-}term}$-S361Acd-V416C modified by $[Fe(phenM)_3]^{2+}$ is shown in Figure 6A. Single-exponential fluorescence lifetimes fall on the universal circle in phasor plots, and for donor-only $SthK_{C\text{-}term}$-S361Acd-V416C, the lifetime data fell on the universal circle at 17 ns (Figure 6A, grey marked with arrow). When fluorescence lifetimes are multi-exponential or nonexponential, the decay data fall inside the universal circle. The data from apo, cAMP, and cGMP conditions all reside within the circle reflecting their complex mixtures of distances. A saturating concentration of cGMP (Figure 6A, green) gives data that lay on a line connecting the apo data (Figure 6A, black) and the cAMP data (Figure 6A, red). This is expected if the cGMP data arises from a mixture of the same distributions found in the apo and cAMP conditions. In contrast, if cGMP were to produce a distinct conformational state with its own donor-acceptor distance, the data would be predicted to lie off the line connecting apo and saturating cAMP concentrations. Using subsaturating concentrations of cAMP illustrates this point as these data also lay along the line connecting apo and saturating cAMP (Figure 6—figure supplement 1). Based on these results, we conclude that the active state produced by cGMP is structurally similar to that produced by cAMP, which is consistent with the previous X-ray crystal structures

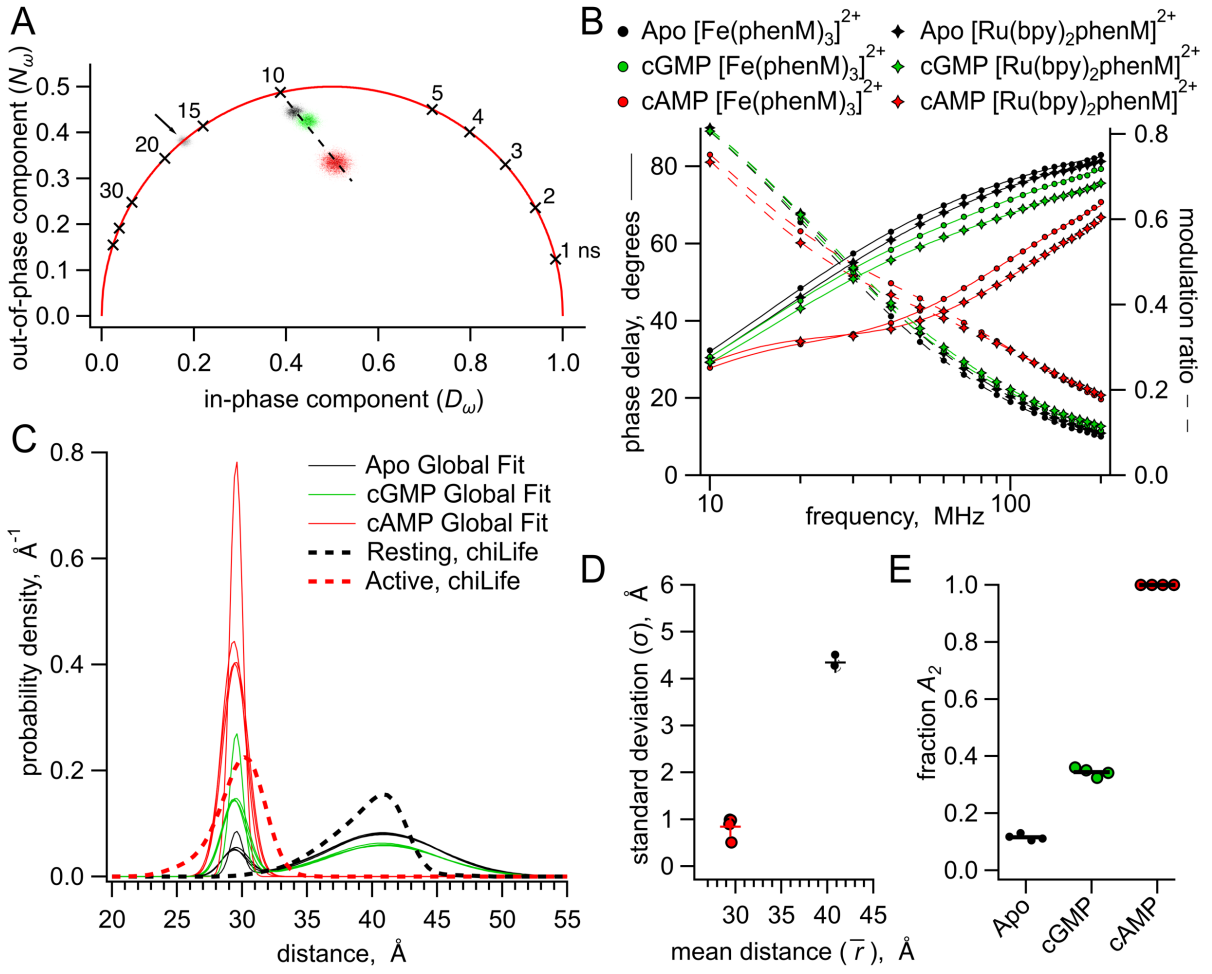

Figure 6. Analysis of lifetime data with global fit model allowing sum of two Gaussian distance distributions. **(A)** Representative phasor plot of measured lifetimes with $[Fe(phenM)_3]^{2+}$ acceptor, where markers on universal circle indicate single-exponential time constants (in nanoseconds). Data shown are donor-only *(*grey), apo (black), cAMP (red*)* and cGMP (green). **(B)** Representative Weber plot showing global fits for $[Fe(phenM)_3]^{2+}$ acceptor data (closed circles) and $[Ru(Bpy)_2phenM]^{2+}$ acceptor data (open diamonds) for apo (black), cAMP (red) and cGMP (green) conditions. **(C)** Spaghetti plot of distance distributions for each experiment (n=4) (thin lines). For comparison, chiLife distributions are overlayed (dashed curves). **(D)** Summary of Gaussian fit standard deviations, σ, versus average distances, $\bar{r}$, for apo and cAMP, with average values as cross marks. Colors correspond to conditions in (A-C). **(E)** Fit values and averages for fraction activation (A_2) for each condition.

of C-terminal SthK with cAMP and cGMP (9). Although the active state is the same, there must be a higher fraction of protein in the resting state in the presence of cGMP compared to cAMP.

To quantify the fraction of resting and active state in apo, cAMP, and cGMP, we next analyzed our lifetime data by globally fitting them to the lifetime model for Gaussian distributions of distances (Figure 5—figure supplement 2). The determination of distance distributions from lifetime experiments alone is an ill-posed problem (23). Using global fits of multiple data sets using three different conditions (apo, cAMP, and cGMP) and two different acceptors with different R_0s increases our ability to determine the various free parameters. For our global fitting analysis, we assumed that the acceptor complexes $[Fe(phenM)_3]^{2+}$ and $[Ru(bpy)_2phenM]^{2+}$ would produce the same measured distance distribution (both within states and between states) for the same acceptor site. This is a reasonable assumption given that: 1) the chemical structures of the complexes are very similar (Figure 2B); 2) chiLife modeling of these two different acceptors produced nearly identical distance distributions (Figure 4B); and 3) dose-response curves for cAMP measured using steady-state FRET were comparable for $[Fe(phenM)_3]^{2+}$- and $[Ru(bpy)_2phenM]^{2+}$-modified protein (Figure 3D). Parameter identifiability for this lifetime model was observed in graphs of χ^2 minimized curves as functions of fixed ranges of each parameter, where minima for each parameter were resolved (Figure 6—figure supplement 2). This global fitting allowed us to determine the fraction of resting and active components, and therefore the free energy change, in each condition.

We globally fit six data sets (each set included phase delay and modulation ratio data), representing the conditions of apo, cAMP and cGMP with the two different acceptors $[Fe(phenM)_3]^{2+}$ and $[Ru(bpy)_2phenM]^{2+}$. We parameterized the distance distribution as the sum of two Gaussians. Each of the Gaussian parameters $\overline{r_1}$, $\overline{r_2}$, σ_1, and σ_2 were assumed to be the same across all conditions, and the fraction of each Gaussian (set by parameter A_2) was allowed to vary between conditions. Global fitting of the lifetime model provided an excellent fit to all of the data (Figure 6B) revealing the distance distributions shown in Figure 6C. Similar to the chiLife predictions (Figure 4) and the single Gaussian fits (Figure 5), the global fits gave $\overline{r_1}$ and $\overline{r_2}$ values of 40.9 Å and 29.5 Å in the resting and active states, respectively, with σ_1 and σ_2 values of 4.3 Å and 0.84 Å in the resting and active states, respectively (Figure 6C, D). Surprisingly, our fits indicated that the apo condition is best explained with 12% in the active

state (A_2 = 0.12) and 88% in the resting state, whereas the saturating cAMP concentration condition was best fit with only the active state (A_2 =1) (Figure 6E). In contrast, cGMP was fit with an A_2 of 0.34. Given that the qualities of these fits are comparable to the single Gaussian fits (with similar χ^2 values), and fewer parameters were used in the global fits than across the sum of comparable data sets with single Gaussian fits, we find the global fitting approach more parsimonious with the phasor plot data and previous SthK X-ray crystallography data in cGMP (9).

Using the probabilities of resting and active states in each condition and the Gibbs free energy equation, we calculated the ΔG and ΔΔG energetics of the transitions in the four-state diagram (Figure 1C and Table 1). In the absence of cyclic nucleotide, the lifetime model fit gave an A_2 of 0.12, corresponding to a ΔG_{Apo} of 1.2 kcal/mol. The isolated $SthK_{C\text{-}term}$, therefore, exhibits considerable activation even in the apo state. For saturating cAMP, for which the global fit indicated an A_2 of 1, we assumed a maximum contribution of the resting state of 0.01, yielding a ΔG_{cAMP} that is more favorable than -2.7 kcal/mol and a $\Delta\Delta G_{cAMP}$ that is more favorable than -3.9 kcal/mol. With a $\Delta\Delta G_{cGMP}$ of -0.82 kcal/mol, cGMP was found here to be a partial agonist, consistent with electrophysiology and previous experiments (7, 8, 10). Interestingly, our measurements reporting the conformational change in the isolated CNBD show a greater activation for apo, cAMP and cGMP, than electrophysiology experiments on full-length channels. These results demonstrate that time-resolved tmFRET can be utilized to obtain energetic information on the individual domains during the allosteric activation of SthK.

Table 1. Calculated Energetics of the Four State Model

Ligand Condition	Ionic Strength (mM KCl)	ΔG (kcal/mol)	ΔΔG (kcal/mol)
Apo	150	1.14 ± 0.03	--
	500	1.2 ± 0.03	--
cAMP	150	--	--
	500	< -2.7 ± 0	< -3.9 ± 0.03
cGMP	150	0.67 ± 0.03	-0.47 ± 0.04
	500	0.38 ± 0.02	-0.82 ± 0.04

Energies are reported in mean values ± SEM.

Changes in Energetics with Salt Concentrations

We were surprised by the high probability of being in the active state for cGMP (A_2 = 0.34) indicated by the sum of Gaussian fits (Figure 6E), especially when electrophysiology shows a much lower open probability with cGMP (Figure 1A). Although this difference might be due to intrinsic energetic differences between our fragment $SthK_{C\text{-}term}$ construct and the full-length channel, it could also arise, in part, from the high ionic conditions (500 mM) used in our lifetime experiments compared with physiological ionic concentrations used in electrophysiology experiments. Known inter-subunit C-terminal salt bridge interactions could be destabilized by increased ionic strength and, previously, it was observed that higher ionic strength eliminated tetramerization in HCN1 C-terminal fragments (7, 29, 30). However, we found no difference in elution volume for SEC experiments performed with $SthK_{C\text{-}term}$-S361Acd-V416C using 150 mM instead of 500 mM KCl, indicating that the oligomerization state was the same under both experimental conditions (Figure 7A).

To test whether the high ionic strength of our experiments contributed to the high A_2 for cGMP, we repeated the above lifetime experiments with a more physiological salt concentration (150 mM KCl). We made new time-resolved tmFRET measurements with $SthK_{C\text{-}term}$-S361Acd-V416C in lower ionic conditions, for both the $[Fe(phenM)_3]^{2+}$ and $[Ru(bpy)_2phenM]^{2+}$ acceptors across apo, cAMP and cGMP conditions. Comparison of $[Fe(phenM)_3]^{2+}$ lifetime data in the two different ionic conditions are shown in the representative Weber plot in Figure 7B. While the apo and cAMP data appeared to be equivalent between 150 and 500 mM KCl, the cGMP data were different between the conditions. When an additional 300 mM KCl was added to protein samples in 150 mM KCl after cGMP application, the phase delay and modulation ratio approached the same lifetimes as the 500 mM KCl cGMP condition (Figure 7B, dark green circle), recapitulating the 500 mM KCl data set. We then globally fit the 150 mM KCl data across $[Fe(phenM)_3]^{2+}$ and $[Ru(bpy)_2phenM]^{2+}$ acceptors for apo, cAMP and cGMP conditions with the sum of two Gaussians (Figure 7C), and found that the average distances, $\overline{r}$, and standard deviations, σ, were nearly identical to those at 500 mM KCl (Figure 7D). The A_2 from cGMP fits decreased in 150 mM KCl compared to 500 mM KCl indicating that a decrease in ionic concentration made activation by cGMP less favorable ($\Delta\Delta G_{cGMP}$ = -0.47 kcal/mol, $\Delta\Delta\Delta G_{cGMP\ KCl}$ = 0.35 kcal/mol). In the absence of ligand, A_2 was unchanged between the two ionic concentrations (Figure 7D),

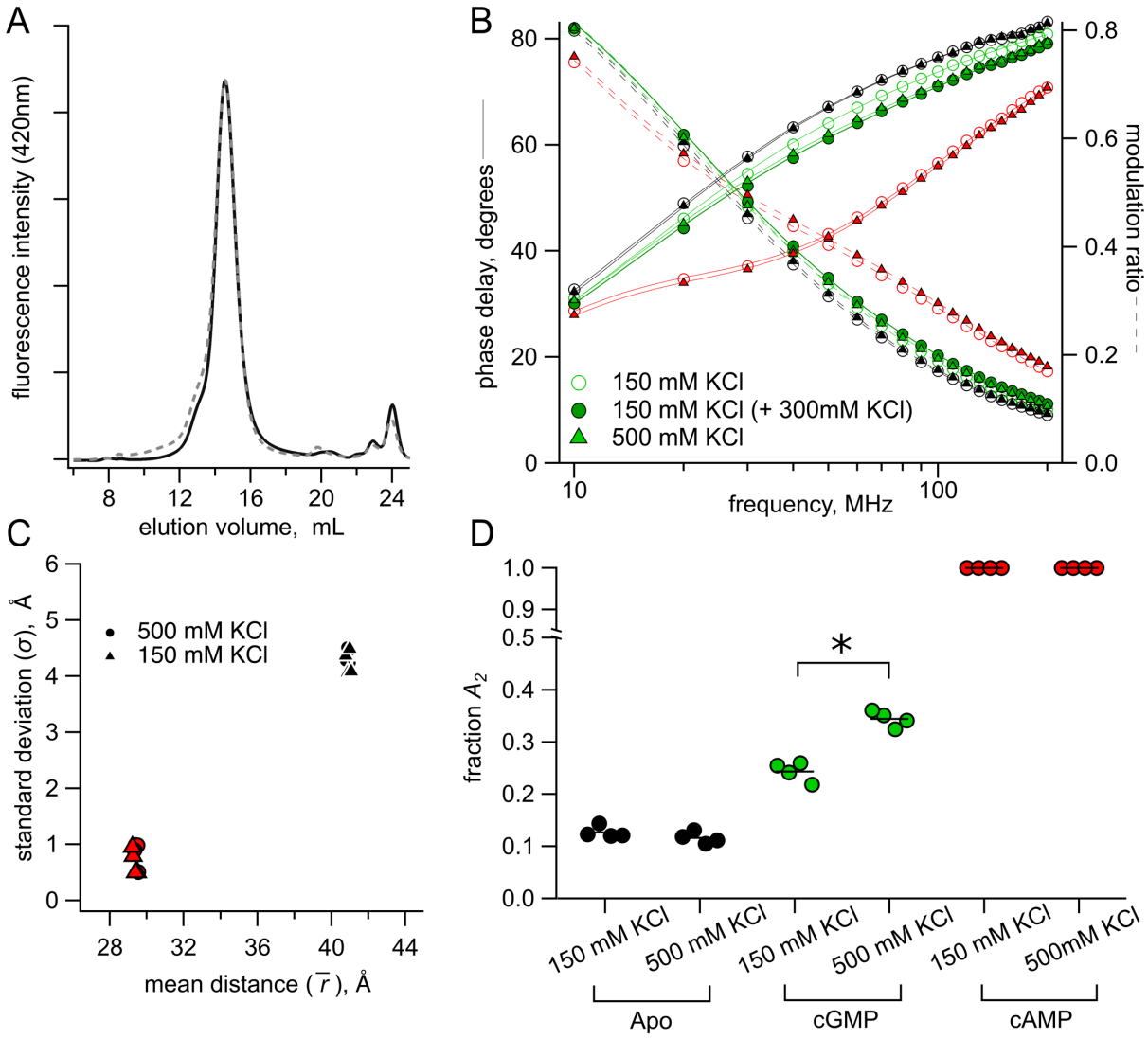

Figure 7. Lifetime measurements in 150 mM KCl versus 500 mM KCl conditions. **(A)** Normalized SEC traces of $SthK_{C\text{-}term}$ in 150 mM KCl (solid curve) and 500 mM KCl (dashed curve). **(B)** Representative Weber plot for $[Fe(phenM)_3]^{2+}$ lifetimes in 150 mM (open circles) and 500 mM KCl (closed triangles), in each ligand condition (apo, black; cGMP, green; cAMP; red). An additional lifetime trace is shown for an experiment where additional 300 mM KCl was added to the protein sample with 150 mM KCl in cGMP (closed green circles). **(C)** Comparison of Gaussian average distance, $\bar{r}$, and standard deviation, σ, between ionic concentrations using model global fitting of $[Fe(phenM)_3]^{2+}$ and $[Ru(bpy)_2phenM]^{2+}$ with the sum of two Gaussians (apo, black, and cAMP, red, n=4). **(D)** Fraction of active state in each condition (A_2) for 150 mM KCl and 500 mM KCl using the sum of two Gaussian model fits [apo P=0.2, cGMP *P=0.0001].

indicating that the increased ionic strength effected only the active conformation in the presence of cGMP. Since activation is already very favorable in the presence of cAMP, we could not determine if ionic strength also effected $\Delta\Delta G_{cAMP}$. These results suggest that ionic strength might specifically affect an electrostatic interaction between CNBD and the cyclic nucleotide during the activation transition.

Discussion

In this study, we measured both steady-state and time-resolved tmFRET for a C-terminal fragment of SthK and interpreted the data using a four-state allosteric model. This approach allowed us to acquire structural information and energetics of the conformational change of the C-helix under different ligand and experimental conditions. Our findings revealed a small presence of the active state in the absence of ligand, while saturating concentrations of cAMP exhibited energetics consistent with that of a full agonist by strongly shifting occupancy into the active state. In contrast, saturating concentrations of cGMP demonstrated characteristics of a partial agonist, eliciting a lower fraction of the same active conformation observed with cAMP. Furthermore, our results demonstrated the impact of both oligomerization and ionic strength on the energetics of the conformational change of isolated $SthK_{C\text{-}term}$.

Our ability to recover structural information in the form of average distance, $\overline{r}$, and standard deviation of distances, σ, from time-resolved tmFRET indicates that this approach is superior to weighted-average steady-state distance measurements alone. The average distance values obtained from lifetime measurements closely matched the distances predicted by chiLife, indicating that the characterized states likely correspond to the observed resting and active states in existing X-ray and cryo-EM structures (9, 11). Whereas the active state's standard deviation (σ_2) closely aligned and was slightly narrower than the chiLife predictions, the resting state's standard deviation (σ_1) was larger than chiLife predictions, even with the global fitting approach. This indicates a broad structural heterogeneity in the resting state that cannot be explained by the rotamer clouds of the labels alone, such as heterogeneity in the position of the C-helix backbone, which is consistent with several past experimental observations (10, 31, 32). Overall, time-resolved tmFRET reliably provides valuable, although sparse, structural insights, especially in cases of heterogeneity where current structural methods are limited.

In addition to the heterogeneity within a given conformational state, time-resolved tmFRET allowed us to obtain the heterogeneity between conformational states (A_2) and thus energetics of state transitions in our four-state model. We determined the distribution between these four conformational states by employing a model comprising the sum of two Gaussian distributions, and globally fitting data across distinct acceptors and ligand conditions. This analysis allowed us to quantify the changes in free energy (ΔG) describing our four-state model. Additionally, we were able to calculate the ΔΔG for each ligand, which represents the free energy imparted by the ligand to drive the conformational change of the CNBD. Although we assumed a model with only two stable conformational states, this may not capture all the stable states in the CNBD. Even if the conformational distributions assumed here were oversimplified, our time-resolved tmFRET approach still allowed for a deeper understanding of the allostery in the C-terminal of SthK.

There are some complications with our time-resolved tmFRET approach that should be considered in future applications. 1) Donor and acceptor sites for tmFRET were carefully selected for solvent accessibility, but it is possible that the introduction of Acd and metal acceptor altered the energetics compared to WT $SthK_{C\text{-}term}$. 2) Incomplete labeling in our protein samples introduces a fraction of donor-only molecules, which are not captured in steady-state measurements but are estimated in our lifetime fits. We have previously shown that there is some degree of correlation among parameters in our FRET model, particularly between the fraction of donor-only and the standard deviation of the Gaussians (22). As a result, it is important to ensure a low contribution (<15%) from the donor-only fraction, and this fraction should be validated by independent methods. 3) Although parameters all reliably converged to χ^2 minimized values in our global fits, some parameters were more identifiable than others (Figure 6—figure supplement 2). 4) Both the single Gaussian distribution model and the sum of two Gaussian distributions model yielded minimized χ^2s and excellent fits, however, our results do not conclusively favor one lifetime model over the other. Whereas the single Gaussian distribution fits contain fewer assumptions, the sum of two Gaussian global fits contain fewer free parameters across the multiple acceptors and conditions. We believe that the assumptions in the four-state model and sum of two Gaussians fitting are reasonable based on both previous experiments and theoretical considerations (7, 12, 22).

A number of previous studies have measured the energetics of allostery in CNBD channels, however interpreting our results within the context of these previous studies presents challenges. These studies have utilized various different CNBD channels where the energetics, including even the ligand specificity, are very different (7, 12, 13, 30, 33–38). For example, in CNGA1 channels from rod photoreceptors, cGMP is a full agonist, and cAMP is a weak partial agonist, while in SthK the agonist specificity is reversed (6, 7, 39, 40). In addition, most of these previous studies have been limited to electrophysiology, which measures the open probability of the pore. Without additional information, the open probability provides only an indirect measurement of the energetics of other domains like the ligand-binding domain. While double electron-electron resonance spectroscopy (DEER) (12, 13, 33, 34) and single-molecule fluorescence studies (11, 35, 41) offer the potential to measure the energetics of individual domains, these methods have not yet been applied to the SthK CNBD. Interestingly, DEER spectroscopy on the HCN2 CNBD fragment revealed a mixture of resting and active states in cAMP (12), whereas we observed in the SthK CNBD fragment a more favorable transition in cAMP. These differences might be due to either inherent differences in the energetics between the C-terminal domains of SthK and HCN2, or the different experimental conditions used, such as the monomeric protein used in the DEER studies vs the tetrameric C-terminal domain studied here. Although their energetics may differ, all CNBD channels studied to date appear to involve an allosteric transition of the CNBD where the binding of cyclic nucleotide promotes a movement of the C-helix relative to the β-roll that is coupled indirectly to the opening of the pore.

For simplicity, here we used the C-terminal fragment of SthK instead of the full-length channel. The relationship between the energetics of the C-terminal fragment and the full-length channel is likely complex and requires further study. For example, coupling of the conformational changes in the individual CNBDs to a concerted opening of the pore is expected to alter both the ΔG for the CNBD transition and the cooperativity of the transitions between subunits. This coupling would also make the $\Delta\Delta G$ measured in the pore by electrophysiology smaller than the $\Delta\Delta G$ we measured in the CNBD. If the conformational change in the CNBD is the same in the fragment and full-length channel, as suggested by structural studies (9, 11), we

could use our measured ΔΔG from the fragment, together with measurements from the full-length channel, to develop a full allosteric model of the intact channel.

Materials and Methods

Key Resources Table				
Reagent type (species) or resource	**Designation**	**Source or reference**	**Identifiers**	**Additional information**
strain, strain background (*Escherichia coli*)	B-95.ΔA *E. coli*	Addgene	Bacterial strain #197933	
recombinant DNA reagent	pDule2-Mj Acd A9 (plasmid)	Addgene	Plasmid #197652	
recombinant DNA reagent	MBP-S361TAG - ctermSthK-TEV-TWS.pETM11 (plasmid)	Addgene		
recombinant DNA reagent	MBP-S361TAG - V416C-ctermSthK-TEV-TWS.pETM11 (plasmid)	Addgene		
recombinant DNA reagent	MBP-Q364TAG - ctermSthK-TEV-TWS.pETM11 (plasmid)	Addgene		

recombinant DNA reagent	MBP-Q364TAG - R417C-ctermSthK-TEV-TWS.pETM11 (plasmid)	Addgene		
software, algorithm	FDlifetime_17_Igor_procedures.ipf	Github	https://github.com/zagotta/FDlifetime_program	

Constructs and Mutagenesis. The C-terminal construct of SthK ($SthK_{C\text{-}term}$) was created by replacing the first 224 residues of cysteine-free SthK in the pETM11 vector (described previously, Uniprot accession #E0R11) (7), with the sequence for MBP followed by a 14 residue asparagine linker and a TEV protease cleavage site, using restriction digestion and T4 ligation. Following the C-terminal end of truncated SthK sequence (225-430), another TEV cleavage site and a Twin-Strep-tag sequence was incorporated using Gibson cloning. An amber stop codon (TAG) was introduced at positions 359, 361 or 364 of the WT $SthK_{C\text{-}term}$ using site directed mutagenesis (42) to create new "donor-only" constructs. To generate constructs with both donor and acceptor sites, a single cysteine mutation was introduced into each donor-only construct at sites 416 or 417, to make the three constructs: $SthK_{C\text{-}term}$-I359TAG-V417C, $SthK_{C\text{-}term}$-S361TAG-V416C, and $SthK_{C\text{-}term}$-Q364TAG-V417C.

Expression and Purification of the C-Terminal SthK fragment. The WT $SthK_{C\text{-}term}$, donor-only, and cysteine-containing constructs were each co-transformed with the AcdA9 aminoacyl tRNA synthetase/tRNA-containing plasmid (pDule2) (43) into B-95.ΔA *E. coli* (DE3) cells(44). The transformed *E. coli* cultures were grown in terrific broth medium at 37° C in 50 μg/ml kanamycin and 60 μg/ml spectinomycin to an OD_{600} ~1.0 before adding Acd (for a final concentration of 0.3 mM), and 0.5 mM isopropyl β-D-1-thiogalactopyranoside (IPTG) for protein induction (27, 45). The cultures were transferred to 18°C to grow an additional 17-19 hours, cells were harvested by centrifugation, and cell pellets were resuspended in lysis buffer (150 mM KCl, 50 mM Tris, 2 mM β-mercaptoethanol, and 10% glycerol, pH 7.4 supplemented with complete mini EDTA-free protease inhibitor cocktail (Pierce, ThermoFisher)). Cell

suspensions were lysed on an Avestin EmulsiFlex-C3 cell disruptor three times at 15,000- 20,000 psi, then diluted with lysis buffer and cleared by centrifugation at 39,000 x g for 30 minutes. Clarified lysate was loaded onto 0.75 mL of Strep-Tactin Superflow high-capacity beads (iba Biosciences) at 4° C in a disposable column. The resin was washed with 25 column volumes of KBT solution (150 mM KCl, 50 mM Tris, 10% glycerol, pH 7.9) and eluted with 10 mM d-Desthiobiotin (Sigma) in KBT buffer. Eluted protein was treated with 10 mM tris(2-carboxyethyl)phosphine (TCEP) to fully reduce cysteines, flash frozen with liquid nitrogen, and stored at -80° C.

Acd-labeled protein was mixed with WT $SthK_{C\text{-}term}$ protein in ratios of >3:1 and were then TEV cleaved with 1:10 vol/vol TEV protease (1.2 mg/ml) for 18 hours at room temperature to cleave the N-terminal MBP and C-terminal Twin-Strep-tag. TEV-cleaved protein was then diluted 1:500 in KBT and then loaded onto a HiTrap Q HP column (GE Healthcare) for ion exchange chromatography (IEC) to remove TEV protease, and cleavage fragments from $SthK_{C\text{-}term}$. $SthK_{C\text{-}term}$ was eluted with an increasing concentration ramp of KCl (10 mM – 1 M) and fractions were collected, with $SthK_{C\text{-}term}$ coming off in a single peak. We used size exclusion chromatography (SEC) on a Superdex 200 10/300 column (GE Healthcare) to evaluate oligomerization state or collect fractions in either KBT or High-KBT (500 mM KCl, 50 mM Tris, 10% Glycerol, pH 7.9).

Mass Photometry. Mass photometry utilizes light scattering to measure the molecular weight of proteins along with their relative abundance in a sample, with an analytical range of 40 kDa - 5 MDa (46, 47). Glass coverslips (24x50 mm) were isopropanol-cleaned and dried with nitrogen gas. We used 10 nM ß-amylase (BAM) to calibrate a TwoMP Mass Photometer instrument (Refeyen Ltd, Oxford, UK). As a background reference, 10 µl of buffer solution (KBT with 150 mM KCl) was first measured in sample gasket wells. Collected SEC $SthK_{C\text{-}term}$ fractions were then measured (10 µl added for total of 20 µl, ~50 nM) and mass histograms collected via the DiscoverMP analysis software. The mass histograms were analyzed with single Gaussian fits in IGOR-Pro v.8 (Wavemetrics, Lake Oswego, OR).

Cyclic Nucleotides and Labeling Reagents. Adenosine 3’,5’-cyclic monophosphate sodium salt monohydrate (cAMP) and guanosine 3’,5’- cyclic monophosphate sodium salt (cGMP) were purchased from Sigma Aldrich and both prepared at 16 mM in 150 mM KCl, 50 mM Tris and

10% glycerol, pH 7.4. Metal acceptor complexes, $[Fe(phenM)_3]^{2+}$, $[Ru(bpy)_2phenM]^{2+}$, and $[Cu(TETAC)]^{2+}$ for tmFRET were prepared as previously described (21, 22).

$SthK_{C\text{-}term}$ Steady-State Fluorescence Measurements. For steady-state tetramer experiments (Figure 3), fractions from IEC-purified $SthK_{C\text{-}term}$ donor-only or $SthK_{C\text{-}term}$-Acd-cysteine protein, with excess WT $SthK_{C\text{-}term}$, were used at high concentration immediately after elution from the IEC. Protein was confirmed as tetrameric by analytical SEC and diluted 1:2 to 1:5 into KBT into quartz cuvettes. Acd fluorescence intensity was measured at 10 second intervals using Jobin Yvon Horiba FluoroMax-3 spectrofluorometer in anti-photobleaching mode (Edison, NJ) as described previously (20, 21). Acceptor molecules at final concentrations of 6 μM $[Fe(phenM)_3]^{2+}$, 20 μM $[Ru(bpy)_2phenM]^{2+}$ or 10 μM $[Cu(TETAC)]^{2+}$ were added to the cuvettes followed by 160 μM final concentration of either cAMP or cGMP. For $[Cu(TETAC)]^{2+}$ experiments, 5 mM TCEP was added after cAMP or cGMP to reverse the tmFRET by removing the acceptor. All experiments had a 'no-cysteine' protein control to correct the FRET efficiency for intensity changes without bound acceptor, where FRET efficiency $E = 1 - (F_{Cys}/F_{No\ Cys})$. In different experiments, FRET efficiencies at increasing concentrations of cAMP were normalized to the maximal observed FRET efficiency and experimental averages were fit with the Hill equation. Fit slopes, h, were fixed at 1 for the $[Ru(bpy)_2phenM]^{2+}$ and $[Cu(TETAC)]^{2+}$ data but was allowed to vary for the $[Fe(phenM)_3]^{2+}$, which did not fit with a slope of 1. For steady-state tmFRET experiments to compare between oligomeric states, monomeric and tetrameric protein were separated and collected by SEC using a Superdex 75 Increase 10/300 GL column (GE Healthcare) and then used directly in fluorescence experiments (Figure 3—figure supplement 1).

Measurements of Fluorescence Lifetimes Using FLIM. For lifetime studies, tetrameric $SthK_{C\text{-}term}$-S361Acd-V416C protein, mixed >1:3 with WT $SthK_{C\text{-}term}$, was labeled with either $[Fe(phenM)_3]^{2+}$ or $[Ru(bpy)_2phenM]^{2+}$. For $[Fe(phenM)_3]^{2+}$ experiments, $SthK_{C\text{-}term}$-S361Acd-V416C protein was buffer exchanged using a BioSpin6 Mini column (BioRad) into KBT (150 mM KCl) or High-KBT (500 mM KCl) then labeled immediately prior to lifetime measurements. For $[Ru(bpy)_2phenM]^{2+}$ experiments, $SthK_{C\text{-}term}$-S361Acd-V416C protein was incubated with 1 mM $[Ru(bpy)_2phenM]^{2+}$ for 30 minutes at room temperature and then buffer exchanged into KBT or High-KBT to remove the unincorporated label.

The theory of time-resolved FRET and the implementation of the lifetime FRET model in the frequency domain have been described previously (23, 48–51). Frequency domain fluorescence lifetime data were obtained using a Q2 laser scanner and A320 FastFLIM system (ISS, Inc., Champaign, IL, USA) attached to a Nikon TE2000U microscope. Acd was excited using a 375 nm pulsed diode laser (ISS, Inc) driven by FastFLIM at 10 MHz, with a long-pass dichroic mirror (387 nM) and a band-pass emission filter (451/106 nm). Collected emission was recorded on a Hamamatsu model H7422P PMT detector. Lifetime measurements were calibrated using Atto 425 in water (with a lifetime of 3.6 ns), using the same optical configuration. Protein samples were used at full strength by pipetting 11 µl onto an ethanol-cleaned #1.5 glass coverslip for recording with a Nikon CFI Super Fluor 10x 0.5NA objective. Confocal images (256 x 256 pixels) were collected with a pinhole of 200 µm and a pixel dwell time of 1 ms. Donor-only lifetimes were obtained from $SthK_{C\text{-}term}$-S361Acd-V416C in KBT and High-KBT solutions prior to the addition of $[Fe(phenM)_3]^{2+}$ at a final concentration of 76.8 µM. $[Ru(bpy)_2phenM]^{2+}$-labeled protein was measured following buffer exchange. Either 1 µl of 16 mM cAMP or 16 mM cGMP was added to acceptor-labeled protein to a final concentration of 1.23 mM. The phase delays and modulation ratios of the fluorescence signal were obtained using VistaVision software from the sine and cosine Fourier transform of the phase histogram H(p), subject to the instrument response function (20).

Lifetime Distance Distribution Model. The model for obtaining a single Gaussian distribution, or a sum of two Gaussian distributions of distances from lifetimes has been described previously (20, 22). Globally fitting lifetime data across $[Fe(phenM)_3]^{2+}$ and $[Ru(bpy)_2phenM]^{2+}$ experiments and the conditions of apo, cAMP and cGMP, used the same model as previously described (Figure 5—figure supplement 2 for parameters), but parameters were constrained differently. Parameters defining the Gaussian states included: two unconstrained average distances ($\overline{r_1}$ and $\overline{r_2}$), two standard deviations (σ_1 and σ_2) constrained between values of 0.5-10 Å, and one fraction for the proportions between the two Gaussians (A_2) varied independently for each of conditions, apo, cAMP and cGMP, constrained between 0 and 1. Other parameters that were varied independently included: the fraction of donor-only in each respective sample, the fraction of background in each experiment (<5%), and the t_0 offset for each experiment. The measured donor-only lifetimes (in KBT and High-KBT) were single exponential, and the time constant was previously measured and held fixed for the global fitting. The acceptor complex R_0

values were determined previously (21) and held constant at 41.8 Å and 43.5 Å for $[Fe(phenM)_3]^{2+}$ and $[Ru(bpy)_2phenM]^{2+}$ respectively[19]. For the single Gaussian lifetime fits, the fraction donor only was held constant within experiments from the same labeled protein samples.

Energetic and Hill Equation Calculations. ΔG, ΔΔG and ΔΔΔG are calculated as follows:

$$\Delta G = -RT * \ln\left(\frac{P_{active}}{P_{resting}}\right) \quad [1]$$

$$\Delta\Delta G_{cNMP} = \Delta G_{cNMP} - \Delta G_{apo} \quad [2]$$

$$\Delta\Delta\Delta G_{cGMP\ KCl} = \Delta\Delta G_{cGMP\ 150\ mM\ KCl} - \Delta\Delta G_{cGMP\ 500\ mM\ KCl} \quad [3]$$

where R is the molar gas constant, T is the absolute temperature (K), and P_{active} and $P_{resting}$ are the proportion of molecules in the active state and resting respectively, and cNMP is cyclic nucleotide (either cAMP or cGMP).

Hill fits (Figure 1B and Figure 3D) were obtained using:

$$Normalized\ Response = 1/\left(1 + (K_{1/2}/[cAMP])^h\right) \quad [4]$$

where $K_{1/2}$ is the concentration of cAMP producing half-maximal FRET change and h is the Hill coefficient.

chiLife Predictions. Computational predictions of the possible rotameric positions for the donor and acceptor labels were made with chiLife using the accessible-volume sampling method as previously described (22, 26). Acd, $[Cu(TETAC)]^{2+}$, $[Fe(phenM)_3]^{2+}$ and $[Ru(bpy)_2phenM]^{2+}$ were added as custom labels in chiLife and modeled onto the cryo-EM structure of the full-length SthK closed state (11) (PDB: 7RSH, residues 225 to 416) and the X-ray crystallography structure of the cAMP bound SthK C-terminal fragment (9) (PDB: 4D7T). For each donor-acceptor pair, labels were superimposed at indicated residue positions and 10,000 possible rotamers were modeled. Rotamers resulting in internal clashes (<2 Å) were removed and external clashes evaluated as previously described (26). Donor-acceptor distance distributions were calculated between the remaining (~500-2000) label rotamers for each donor-acceptor pair. Inter-subunit distances were calculated as distances between one Acd molecule and the modeled acceptor rotamers on each of the other three subunits.

Electrophysiology. The cysteine-free construct of full-length SthK (cfSthK) was cloned into a pcGFP vector (52) (with YFP instead of GFP) and expressed in E.*coli* C43(DE3) bacteria (53). A valine to alanine mutation at position 208 was added for increased open channel probability (A208V-cfSthK-YFP) (7). Spheroplasts were formed from the C43 samples as previously described (7). SthK currents were recorded from inside-out spheroplast patches using an Axopatch 200A amplifier with Patchmaster software (HEKA Elektronik) as previously described (7). The pipette and bath recording solution were both:150 mM KCl, 20 mM $MgCl_2$, 500 mM sucrose, 10 mM HEPES, pH7.4 (7). Currents were measured using jumps in the holding potential from 0 mV to +80 mV. Fractional activation for 1 mM cGMP were obtained by comparing the fractional response to 1 mM cAMP in the same patch.

Statistics and reproducibility. Data values were expressed as mean ± SEM of n independent experiments, unless stated otherwise, and all error bars are ± SEM. Statistical significance (*$P<0.05$) was determined by using a two tailed Student's t-test.

Acknowledgements

We thank the Oregon State University GCE4ALL (Center for Genetic Code Expansion for All) for their long-standing collaboration, and Drs. Chloe Jones, James Petersson, and Kyle D Shaffer. (University of Pennsylvania) for excellent technical support. We also thank Dr. Lisa Tuttle (University of Washington) for assistance with Mass Photometry and all members of the SEG and WNZ laboratories for helpful conversations and support. Research reported in this publication was supported by the National Institutes of Health under award numbers R35GM145225 (to SEG), R35GM148137 and R01EY010329 (to WNZ), T32GM008268 and T32EY7031-43 (to PE).

References

1. K. B. Craven, W. N. Zagotta, CNG and HCN channels: Two peas, one pod. *Annu Rev Physiol* **68**, 375–401 (2006).
2. K. Matulef, W. N. Zagotta, Cyclic Nucleotide-Gated Ion Channels. *Annu Rev Cell Dev Biol* **19**, 23–44 (2003).
3. C. He, F. Chen, B. Li, Z. Hu, Neurophysiology of HCN channels: From cellular functions to multiple regulations. *Prog Neurobiol* **112**, 1–23 (2014).
4. U. B. Kaupp, R. Seifert, Cyclic Nucleotide-Gated Ion Channels. *Physiol Rev* **82**, 769–824 (2002).
5. Z. M. James, W. N. Zagotta, Structural insights into the mechanisms of CNBD channel function. *Journal of General Physiology* **150**, 225–244 (2018).
6. M. Brams, J. Kusch, R. Spurny, K. Benndorf, C. Ulens, Family of prokaryote cyclic nucleotide-modulated ion channels. *Proc Natl Acad Sci U S A* **111**, 7855–7860 (2014).
7. J. L. W. Morgan, E. G. B. Evans, W. N. Zagotta, Functional characterization and optimization of a bacterial cyclic nucleotide-gated channel. *Journal of Biological Chemistry* **294**, 7503–7515 (2019).
8. P. A. M. Schmidpeter, X. Gao, V. Uphadyay, J. Rheinberger, C. M. Nimigean, Ligand binding and activation properties of the purified bacterial cyclic nucleotide-gated channel SthK. *Journal of General Physiology* **150**, 821–834 (2018).
9. D. Kesters, *et al.*, Structure of the SthK carboxy-terminal region reveals a gating mechanism for cyclic nucleotide-modulated ion channels. *PLoS One* **10**, 1–12 (2015).
10. J. Rheinberger, X. Gao, P. A. M. Schmidpeter, C. M. Nimigean, Ligand discrimination and gating in cyclic nucleotide-gated ion channels from apo and partial agonist-bound cryo-EM structures. *Elife* **7**, 1–25 (2018).
11. X. Gao, *et al.*, Gating intermediates reveal inhibitory role of the voltage sensor in a cyclic nucleotide-modulated ion channel. *Nat Commun* **13** (2022).
12. H. A. DeBerg, P. S. Brzovic, G. E. Flynn, W. N. Zagotta, S. Stoll, Structure and energetics of allosteric regulation of HCN2 ion channels by cyclic nucleotides. *Journal of Biological Chemistry* **291**, 371–381 (2016).
13. A. Collauto, *et al.*, Rates and equilibrium constants of the ligand-induced conformational transition of an HCN ion channel protein domain determined by DEER spectroscopy. *Physical Chemistry Chemical Physics* **19**, 15324–15334 (2017).
14. D. Colquhoun, Binding, gating, affinity and efficacy: The interpretation of structure-activity relationships for agonists and of the effects of mutating receptors. *Br J Pharmacol* **125**, 923–947 (1998).
15. A. Auerbach, Life at the top: the transition state of AChR gating. *Sci STKE* **2003**, 1–9 (2003).
16. H. Y. Aviram, *et al.*, Direct observation of ultrafast large-scale dynamics of an enzyme under turnover conditions. *Proc Natl Acad Sci U S A* **115**, 3243–3248 (2018).
17. J. Guo, H. X. Zhou, Protein Allostery and Conformational Dynamics. *Chem Rev* **116**, 6503–6515 (2016).
18. F. T. Horrigan, R. W. Aldrich, Coupling between voltage sensor activation, Ca2+ binding and channel opening in large conductance (BK) potassium channels. *J Gen Physiol* **120**, 267–305 (2002).

19. H. Hofmann, All over or overall - Do we understand allostery? *Curr Opin Struct Biol* **83**, 102724 (2023).
20. W. N. Zagotta, *et al.*, An improved fluorescent noncanonical amino acid for measuring conformational distributions using time-resolved transition metal ion FRET. *Elife* **10**, 2021.05.10.443484 (2021).
21. S. E. Gordon, *et al.*, Long-distance tmFRET using bipyridyl- and phenanthroline-based ligands. *Biophys J* 2023.10.09.561591 (2024). https://doi.org/10.1016/j.bpj.2024.01.034.
22. W. N. Zagotta, *et al.*, Measuring conformational equilibria in allosteric proteins with time-resolved tmFRET. *Biophys J* 2023.10.09.561594 (2024). https://doi.org/10.1016/j.bpj.2024.01.033.
23. J. R. Lakowicz, *Principles of fluorescence spectroscopy* (2006).
24. I. Sungwienwong, *et al.*, Improving target amino acid selectivity in a permissive aminoacyl tRNA synthetase through counter-selection. *Org Biomol Chem* **15**, 3603–3610 (2017).
25. L. Stryer, R. P. Haugland, Energy transfer: a spectroscopic ruler. *Proc Natl Acad Sci U S A* **58**, 719–726 (1967).
26. M. H. Tessmer, S. Stoll, chiLife: An open-source Python package for in silico spin labeling and integrative protein modeling. *PLoS Comput Biol* **19**, 1–16 (2023).
27. L. C. Speight, *et al.*, Efficient synthesis and in vivo incorporation of acridon-2-ylalanine, a fluorescent amino acid for lifetime and Förster resonance energy transfer/luminescence resonance energy transfer studies. *J Am Chem Soc* **135**, 18806–18814 (2013).
28. M. A. Digman, V. R. Caiolfa, M. Zamai, E. Gratton, The phasor approach to fluorescence lifetime imaging analysis. *Biophys J* **94**, 14–16 (2008).
29. M. Lolicato, *et al.*, Tetramerization dynamics of C-terminal domain underlies isoform-specific cAMP gating in hyperpolarization-activated cyclic nucleotide-gated channels. *Journal of Biological Chemistry* **286**, 44811–44820 (2011).
30. K. B. Craven, W. N. Zagotta, Salt bridges and gating in the COOH-terminal region of HCN2 and CNGA1 channels. *J Gen Physiol* **124**, 663–677 (2004).
31. J. W. Taraska, M. C. Puljung, N. B. Olivier, G. E. Flynn, W. N. Zagotta, Mapping the structure and conformational movements of proteins with transition metal ion FRET. *Nat Methods* **6**, 532–537 (2009).
32. K. Matulef, W. N. Zagotta, Multimerization of the ligand binding domains of cyclic nucleotide-gated channels. *Neuron* **36**, 93–103 (2002).
33. M. C. Puljung, H. A. DeBerg, W. N. Zagotta, S. Stoll, Double electron - Electron resonance reveals cAMP-induced conformational change in HCN channels. *Proc Natl Acad Sci U S A* **111**, 9816–9821 (2014).
34. E. G. B. Evans, J. L. W. Morgan, F. DiMaio, W. N. Zagotta, S. Stoll, Allosteric conformational change of a cyclic nucleotide-gated ion channel revealed by DEER spectroscopy. *Proc Natl Acad Sci U S A* **117**, 10839–10847 (2020).
35. M. P. Goldschen-Ohm, *et al.*, Structure and dynamics underlying elementary ligand binding events in human pacemaking channels. *Elife* **5** (2016).
36. C. Pfleger, *et al.*, Allosteric signaling in C-linker and cyclic nucleotide-binding domain of HCN2 channels. *Biophys J* **120**, 950–963 (2021).
37. K. B. Craven, N. B. Olivier, W. N. Zagotta, C-terminal movement during gating in cyclic nucleotide-modulated channels. *J Biol Chem* **283**, 14728–14738 (2008).

38. M. Kondapuram, *et al.*, Functional and structural characterization of interactions between opposite subunits in HCN pacemaker channels. *Commun Biol* **5**, 1–14 (2022).
39. S. E. Gordon, W. N. Zagotta, A histidine residue associated with the gate of the cyclic nucleotide-activated channels in rod photoreceptors. *Neuron* **14**, 177–183 (1995).
40. M. D. Varnum, K. D. Black, W. N. Zagotta, Molecular mechanism for ligand discrimination of cyclic nucleotide-gated channels. *Neuron* **15**, 619–625 (1995).
41. M. P. Goldschen-Ohm, D. S. White, V. A. Klenchin, B. Chanda, R. H. Goldsmith, Observing Single-Molecule Dynamics at Millimolar Concentrations. *Angew Chem Int Ed Engl* **56**, 2399–2402 (2017).
42. H. Liu, J. H. Naismith, An efficient one-step site-directed deletion, insertion, single and multiple-site plasmid mutagenesis protocol. *BMC Biotechnol* **8**, 91 (2008).
43. I. Sungwienwong, *et al.*, Improving target amino acid selectivity in a permissive aminoacyl tRNA synthetase through counter-selection. *Org Biomol Chem* **15**, 3603–3610 (2017).
44. T. Mukai, *et al.*, Highly reproductive Escherichia coli cells with no specific assignment to the UAG codon. *Sci Rep* **5**, 1–9 (2015).
45. C. M. Jones, Y. Venkatesh, E. J. Petersson, *Protein labeling for FRET with methoxycoumarin and acridonylalanine*, 1st Ed. (Elsevier Inc., 2020).
46. D. Wu, G. Piszczek, Standard protocol for mass photometry experiments. *Eur Biophys J* **50**, 403–409 (2021).
47. G. Young, *et al.*, Quantitative mass imaging of single biological macromolecules. *Science* **360**, 423–427 (2018).
48. J. R. Lakowicz, *et al.*, Resolution of the conformational distribution and dynamics of a flexible molecule using frequency-domain fluorometry. *Biophys Chem* **39**, 79–84 (1991).
49. H. C. Cheung, *et al.*, Conformational flexibility of the Cys 697-Cys 707 segment of myosin subfragment-1: Distance distributions by frequency-domain fluorometry. *Biophys Chem* **40**, 1–17 (1991).
50. J. R. Lakowicz, *et al.*, Distance distributions in proteins recovered by using frequency-domain fluorometry. Applications to troponin I and its complex with troponin C. *Biochemistry* **27**, 9149–9160 (1988).
51. R. A. Hochstrasser, S. M. Chen, D. P. Millar, Distance distribution in a dye-linked oligonucleotide determined by time-resolved fluorescence energy transfer. *Biophys Chem* **45**, 133–141 (1992).
52. T. Kawate, E. Gouaux, Fluorescence-detection size-exclusion chromatography for precrystallization screening of integral membrane proteins. *Structure* **14**, 673–681 (2006).
53. B. Miroux, J. E. Walker, Over-production of proteins in Escherichia coli: mutant hosts that allow synthesis of some membrane proteins and globular proteins at high levels. *J Mol Biol* **260**, 289–298 (1996).

Supplemental Figures

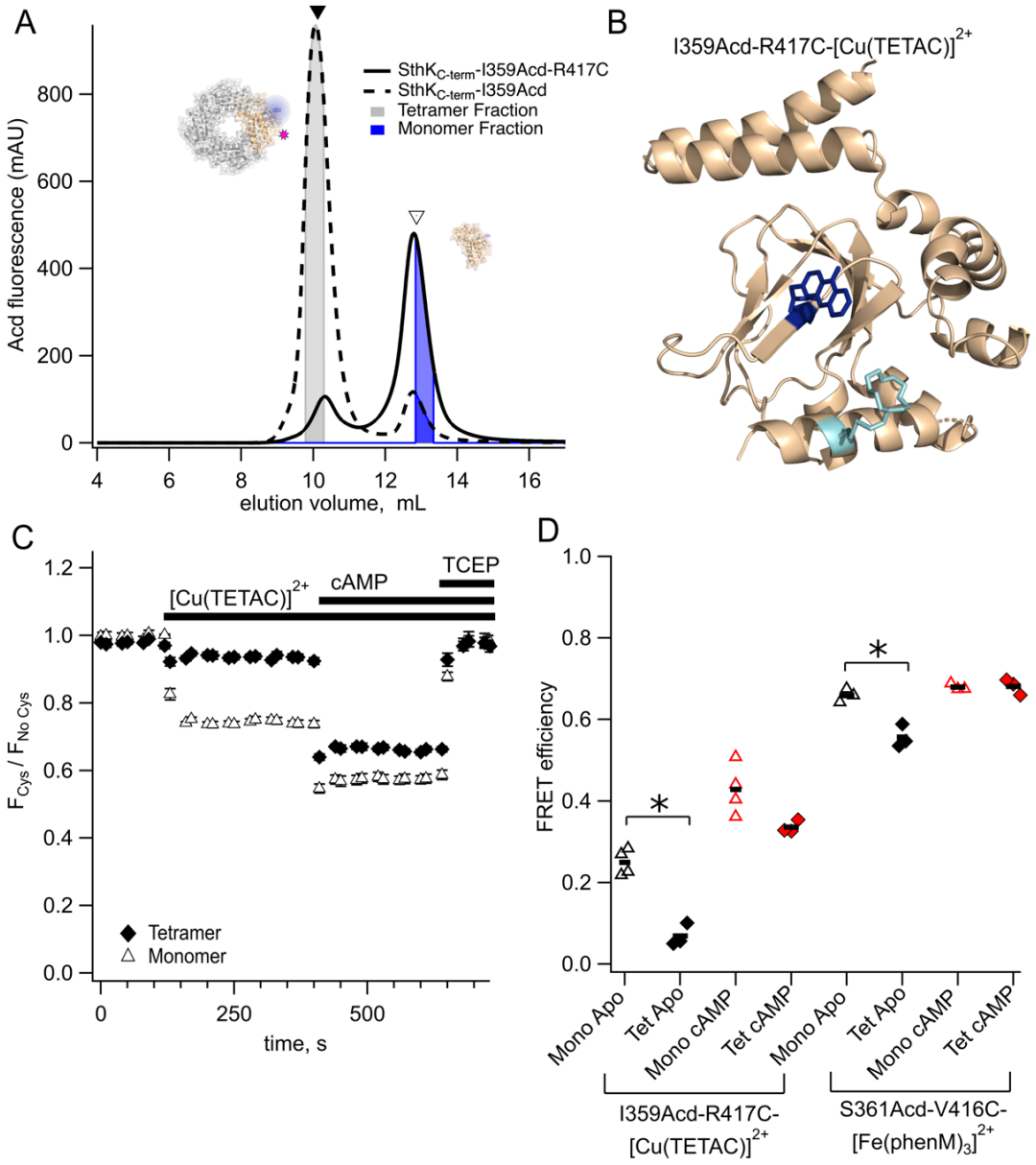

Figure 3—figure supplement 1. Steady-state tmFRET of monomeric and tetrameric SthK$_{C\text{-}term}$. **(A)** SEC chromatogram showing separation of monomeric (empty triangle, blue area) and tetrameric protein (solid triangle, gray area) fractions for SthK$_{C\text{-}term}$-I359Acd and SthK$_{C\text{-}term}$-I359Acd-R417C (no WT SthK$_{C\text{-}term}$ present) on a Superdex 75 increase 10/300 column (GE Healthcare). **(B)** Structure showing SthK$_{C\text{-}term}$-I359Acd with [Cu(TETAC)]$^{2+}$ acceptor at R417C (PDB:4D7T). **(C)** Fluorescence time-course of SthK$_{C\text{-}term}$-I359Acd-417C upon addition of [Cu(TETAC)]$^{2+}$, cAMP and TCEP in tetrameric protein (closed diamonds) and monomeric protein (open triangles). **(D)** Summary of FRET efficiencies for monomer and tetramer, with mean values shown as horizontal lines. Left: SthK$_{C\text{-}term}$-I359Acd-R417C-[Cu(TETAC)]$^{2+}$ (apo, *P=0.0005, cAMP, P=0.06). Right: SthK$_{C\text{-}term}$-S361Acd-V416C-[Fe(phenM)$_3$]$^{2+}$ apo, *P=0.006, cAMP: P=0.9).

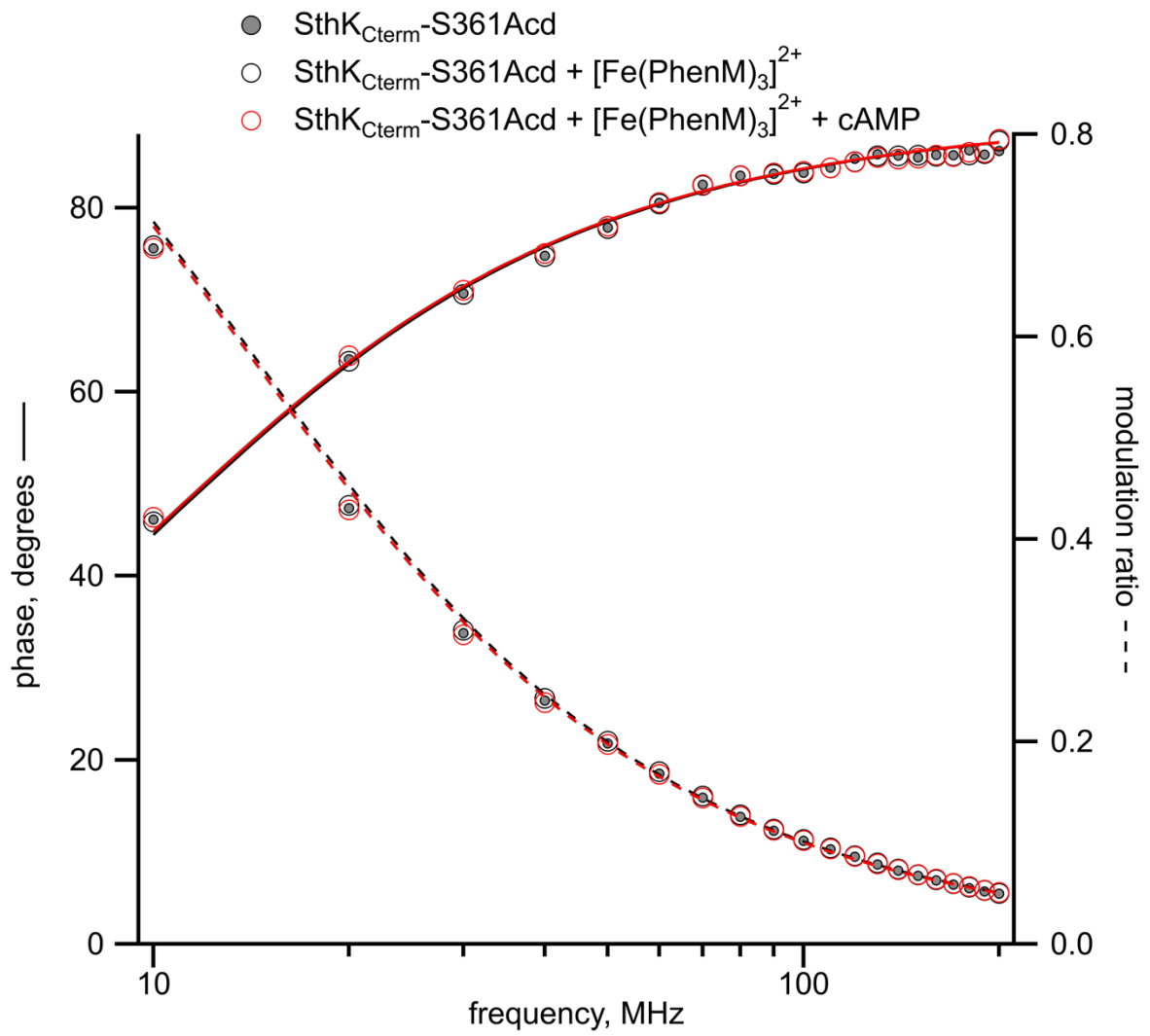

Figure 5—figure supplement 1. Representative Weber plot of measured lifetimes of SthK$_{C\text{-}term}$-S361Acd donor-only (grey), then in the presence of [Fe(phenM)$_3$]$^{2+}$ (black), and after the addition of 1.23 mM cAMP (red), showing no change in lifetimes in the absence of a cysteine residue.

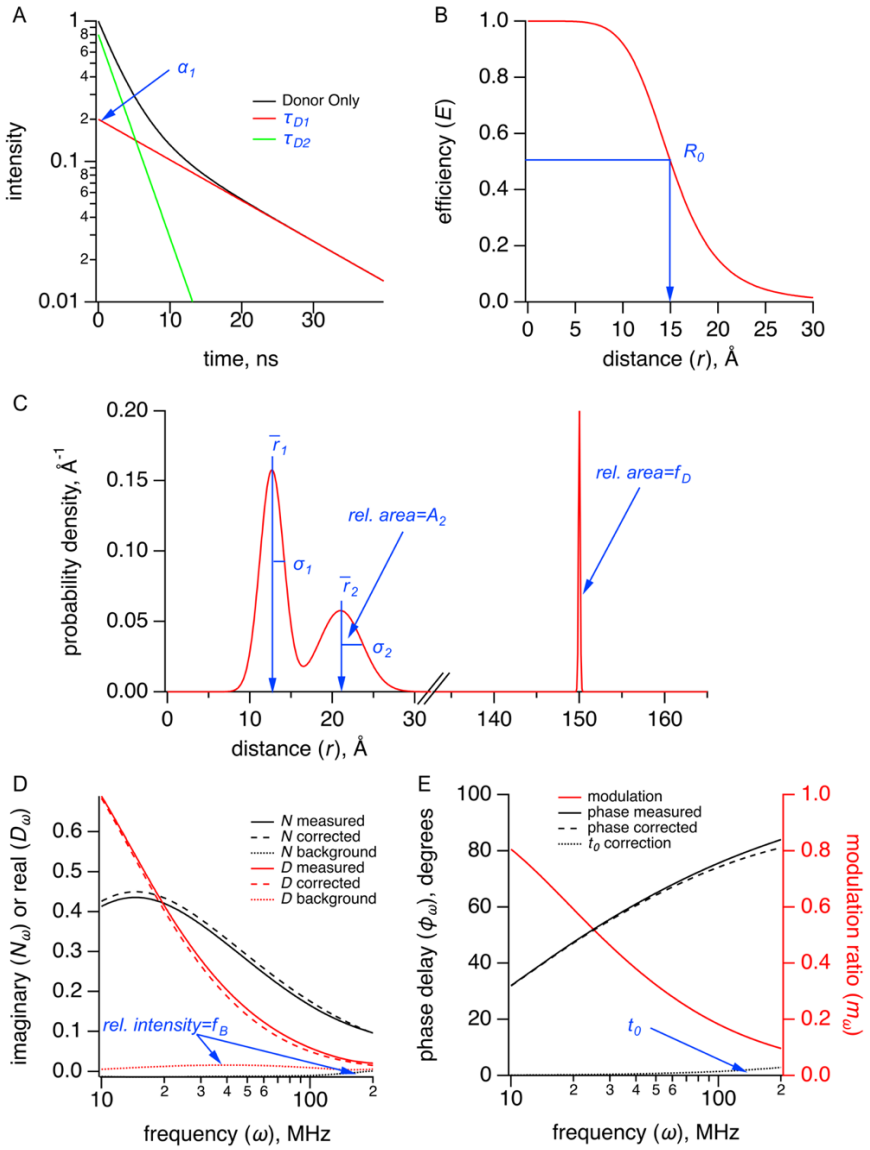

Figure 5—figure supplement 2. Parameters used in the lifetimes fitting model for both the single and sum of two Gaussian approaches, shown in blue. **(A)** Graph of donor-only fluorescence-lifetime decay with two exponential components with time constants (τ_{D1}, τ_{D2}) **(B)** FRET efficiency (E) plot as a function of distance (r) between donor and acceptor and the R_0 values for 50% FRET transfer. **(C)** Probability distribution plot of donor and acceptor distances P(r) showing the sum of two Gaussian distributions, each with their own average distance ($\overline{r_1}$ and $\overline{r_2}$), standard deviations (σ_1 and σ_2) and relative amplitude of the second component (A_2). The donor-only fraction (f_D) is modeled as a narrow Gaussian with mean distance of 150 Å and standard deviation of 0.1 Å, beyond a detectable amount of FRET. **(D)** The in-phase (D_ω) and out-of-phase (N_ω) components are plotted for the measured, corrected, and background fluorescence signal as a function of the excitation modulation frequency (ω), where f_B is the fraction of the fluorescence intensity due to the background. **(E)** Plot of the phase delay (φ_ω) and modulation ratio (m_ω) of the measured and corrected fluorescence response as a function of the modulation frequency (ω) where t_0 is the time shift of the instrument response function.

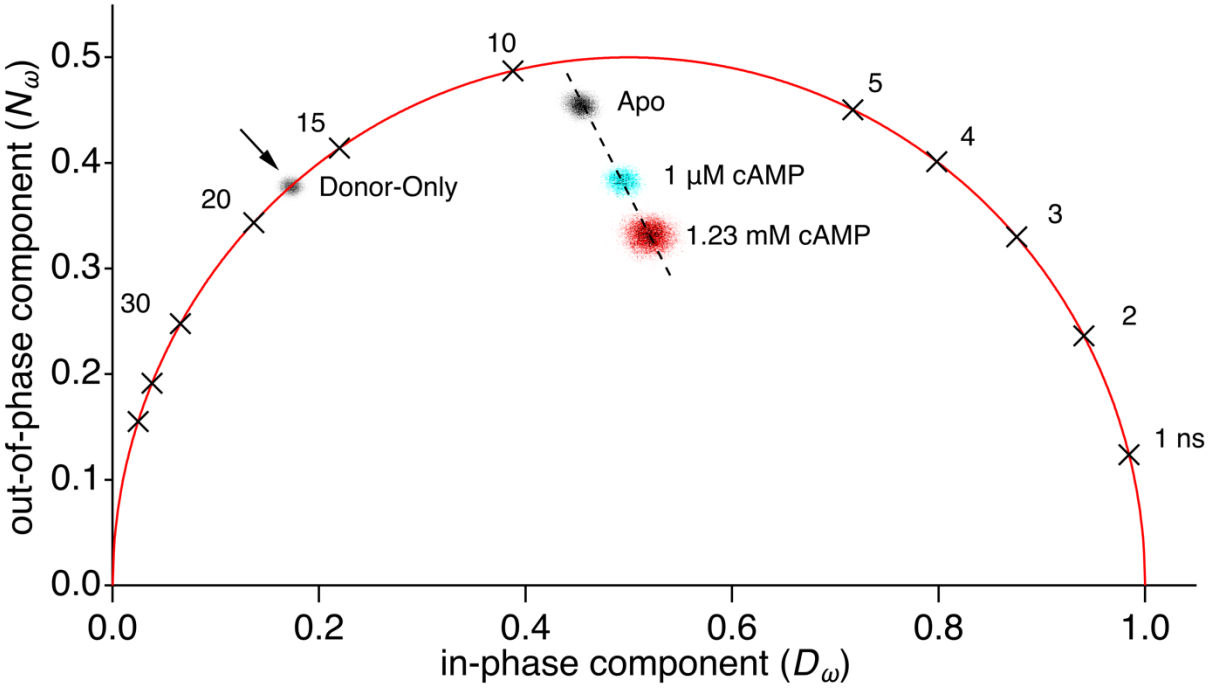

Figure 6—figure supplement 1. Representative phasor plot of measured lifetimes of $SthK_{C\text{-}term}$-S361Acd-V416C alone (donor-only, grey), in the presence of $[Ru(bpy)_2phenM]^{2+}$ (apo, black), in the presence of 1 µM cAMP (cyan) and presence of 1.23 mM cAMP (red).

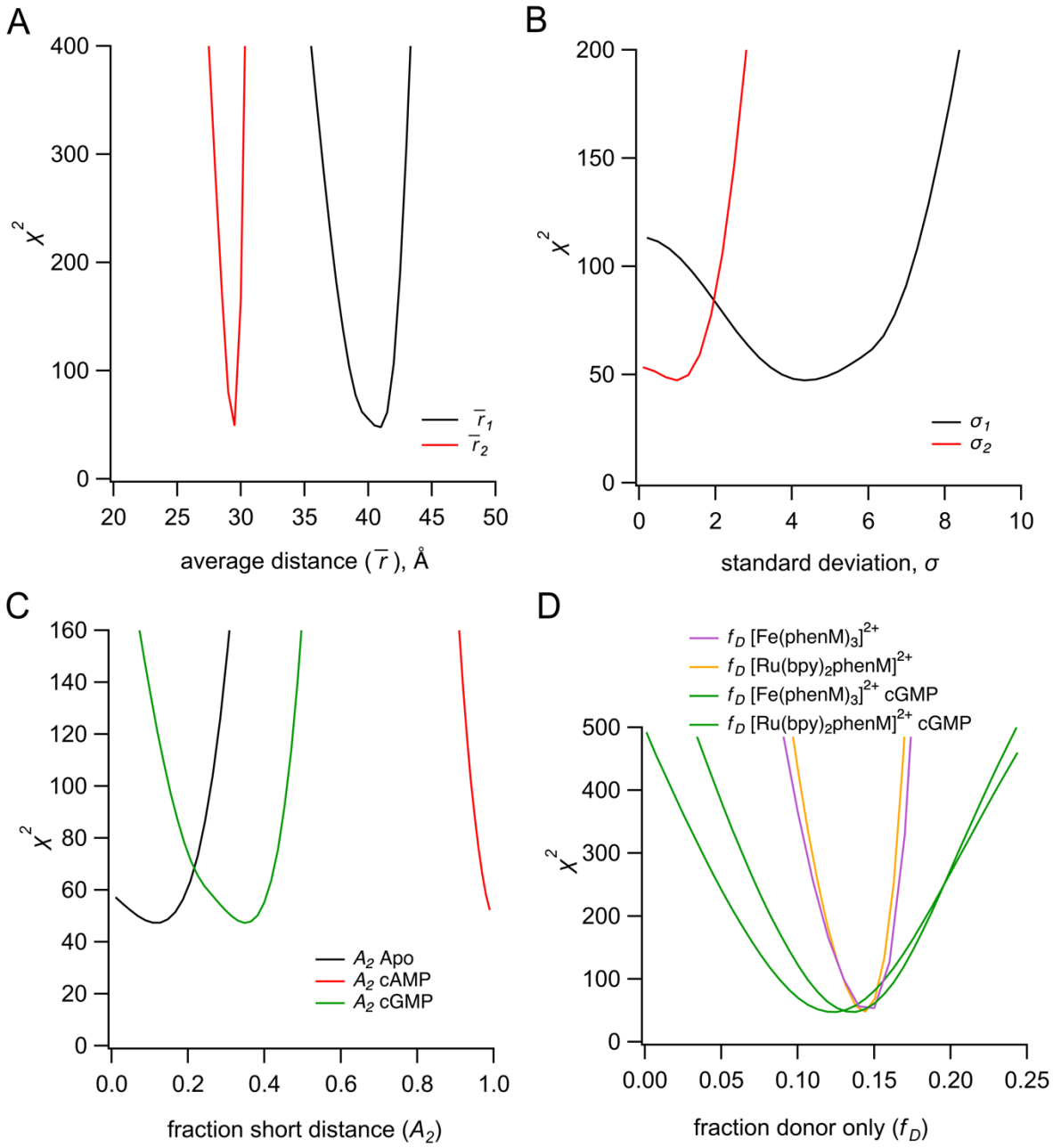

Figure 6—figure supplement 2. Identifiability of parameters in the sum of two Gaussian distributions model, with global fitting Fe(phenM)$_3$]$^{2+}$ and [Ru(bpy)$_2$phenM]$^{2+}$ data. **(A-B)** Minimization of χ^2 values for the Gaussian average distance ($\bar{r}$) (A) and standard deviation (σ) (B) for the resting (black) and active states (red). **(C)** Minimization of χ^2 values for parameter A_2 for the conditions of apo, cAMP and cGMP. **(D)** Minimization of χ^2 values for the fraction of donor-only component (f_D) in protein samples for each experiment of apo and cAMP for [Fe(phenM)$_3$]$^{2+}$, of apo and cAMP for [Ru(bpy)$_2$phenM]$^{2+}$, of cGMP for [Fe(phenM)$_3$]$^{2+}$, and of cGMP for [Ru(bpy)$_2$phenM]$^{2+}$.

Chapter 4: Domain Coupling in Allosteric Regulation of SthK Measured Using Time-Resolved Transition Metal Ion FRET

Preface

This work is intended for publication, with the following authors in order: Pierce Eggan, Sharona E. Gordon, and William N. Zagotta.

Author contributions:

Direct contribution to this work by P. Eggan, myself, include: designing and conducting all experiments, all data analysis, figure preparation, writing, and data curation.

W.N. Zagotta and S.E. Gordon contributed with conceptualization, experimental design, and data analysis. W.N. Zagotta produced Figure 2-Supplemental 1 and Figure 2-Supplemental 2.

Abstract

Cyclic nucleotide-binding domain (CNBD) ion channels are vital for cellular signaling and excitability, with activation regulated by cyclic adenosine- or guanosine-monophosphate (cAMP, cGMP) binding. However, the allosteric mechanisms underlying this activation, particularly the energetics that describe conformational changes within individual domains and between domains, remain unclear. The prokaryotic CNBD channel SthK has been a useful model for better understanding this allosteric mechanism. Here, we applied time-resolved transition metal ion Förster resonance energy transfer (tmFRET) to investigate the conformational dynamics and energetics in the CNBD of SthK, first in a soluble C-terminal fragment of the protein, $SthK_{Cterm}$, and then in the full-length channel, $SthK_{Full}$. We incorporated the noncanonical amino acid Acd as a FRET donor and a metal bound to a chelator-conjugated to a cysteine as an acceptor. We used time correlated single photon counting (TCSPC) to measure time-resolved FRET and fit the TCSPC data to obtain donor-acceptor distance distributions in the absence and presence of cAMP. The distance distributions allowed us to quantify the energetics of coupling between the C-terminal domains and the transmembrane domains by comparing the donor-acceptor distance distributions for $SthK_{Cterm}$ and $SthK_{Full}$. Our data indicate that the presence of the SthK transmembrane domains makes the activating conformational change in the CNBD more favorable. These findings highlight the power of time-resolved tmFRET to uncover the structural and energetic landscapes of allosteric proteins and of the ligand-mediated mechanism in CNBD channels specifically.

Introduction

Cyclic nucleotide-binding domain (CNBD) ion channels are essential for a variety of physiological processes, including signal transduction and cellular excitability, and are regulated by combinations of environmental stimuli, including second messenger cyclic nucleotides and changes in voltage (1–3). When cyclic nucleotides bind to the CNBD of these tetrameric channels, these proteins undergo conformational changes resulting in the opening of the channel pore (4–6). However, this central channel pore is over 60Å away each of four peripheral binding sties and the allosteric mechanism that underlies this 'activity at a distance' remains incompletely understood. Within the CNBD channel family, the prokaryotic ion channel SthK has been a useful model to better understand the underlying mechanisms of ligand gating overall (7–11). The functional characteristics of SthK, such as open probabilities and kinetics, have been described with both macroscopic and single channel electrophysiology, but this has left many questions unanswered about structural and energetic changes occurring outside of the pore domain (12). X-ray crystallography and cryo-EM structures of SthK channels have revealed large structural changes across multiple domains with cyclic adenosine monophosphate (cAMP) binding but are inherently static snapshots and have not been able to capture the full heterogeneity within and between conformational states that proteins are known to possess (9, 13, 14). As a result, there is still a considerable need to integrate both conformational and energetic information in these channels to provide a more complete mechanistic understanding of how binding of cyclic nucleotide in the CNBD alters the energetics of the pore opening.

Our previous work utilized time-resolved transition metal ion FRET (tmFRET) to investigate the conformational and energetic changes of the CNBD in an isolated C-terminal fragment of SthK ($SthK_{Cterm}$) (15). Distance distributions were obtained for the movement of the C-helix relative to the beta-roll of the CNBD in the presence and absence of ligand, which allowed for the calculation of change in free energy (ΔG) and differences in free energy change ($\Delta\Delta G$) induced by cyclic nucleotide. However, these $SthK_{Cterm}$ measurements were made in a truncated portion of the protein without the physiologically relevant pore and transmembrane domains. It remained unclear how this conformational change of the CNBD might look in the full-length channel and how the energetics that describe this transition might differ between the full channel structure ($SthK_{Full}$) and the isolated C-terminal domains ($SthK_{Cterm}$, Figure 1A). In

the intact channel, the CNBD and C-linker domains are directly coupled to the pore and the transmembrane region (Figure 1A). Just as the CNBD's conformational transition is known to affect the opening of the pore domain, as is evident from the ionic current induced by the binding of cyclic nucleotides, in converse the presence of the pore must influence the energetics of the CNBD transitions. Understanding this coupling between the C-terminal domains and the pore in the full-length channel, both in terms of its direction (whether the pore enhances or inhibits the CNBD transition) and its overall magnitude, is essential for understanding the allosteric mechanism of CNBD channels.

The 'modular-gating scheme,' as also called the 'ensemble' allostery model, provides a powerful framework for integrating structural and energetic contributions across distinct protein regions (16–18). In this model, allosteric transitions are viewed through a modular lens, where individual domains or functional modules undergo conformational changes that are energetically coupled to one another. The number of modules, as well as which modules are coupled together, can be different depending on the protein and available structural or functional information. For SthK and other CNBD channels, a modular gating scheme is shown for ligand gating in Figure 1B, suggesting distinct modules (four separate CNBDs, a single concerted C-linker, and a single pore) involved in the allosteric process, each with their own conformational changes (5). Within each module, the conformational transition can be described using equilibrium constants and a simple four-state model (double arrows within modules of Figure 1B), as previously described (15). For example, the CNBD can be thought to transition between 'resting' (*R*) and 'active' states (*A*), which can both exist in either ligand-unbound (apo) or bound (holo) states. Importantly, this scheme highlights that the conformational changes in the CNBD are not isolated, but are coupled to transitions in other modules, such as the C-linker and pore domains (arrows between modules in Figure 1B). By measuring the conformational energetics from different modules in the intact channel, we can begin to quantify the extent of inter-domain coupling and identify how energetic contributions from different modules combine to drive the allosteric mechanism of CNBD channels. Specifically, when comparing the energetics of the CNBD C-helix in $SthK_{Cterm}$ to the energetics of the same transition in $SthK_{Full}$, we can identify the extent of energetic coupling between the cytoplasmic domains and the transmembrane regions of the channel, including the pore.

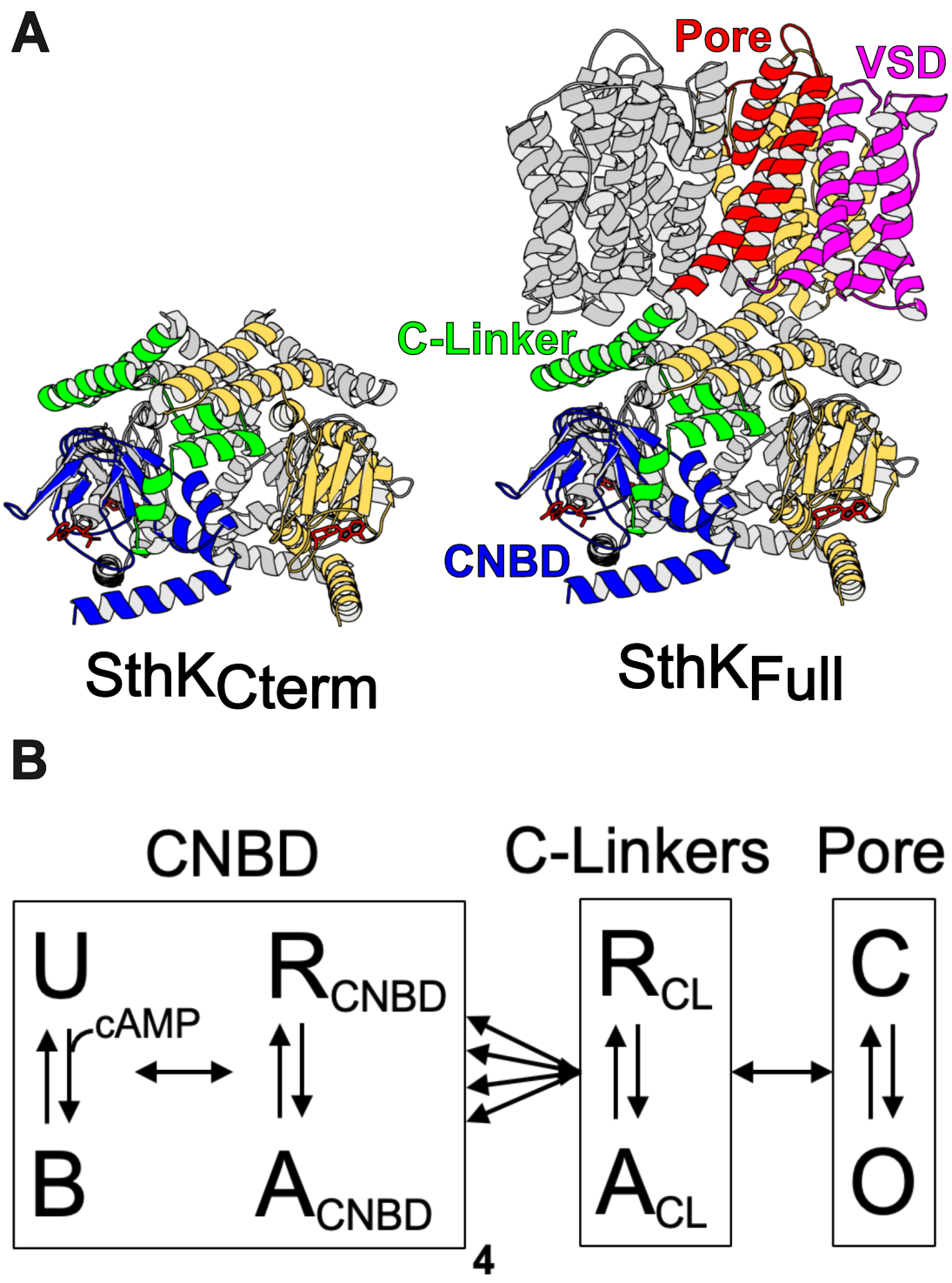

Figure 1. Structure of SthK constructs and modular gating scheme. **(A)** Cartoon structures for $SthK_{Cterm}$ and $SthK_{Full}$ with the domains labeled on the $SthK_{Full}$ structure. **(B)** Modular gating scheme for SthK showing different modules from domains of the structures. Within each domain, resting (*R*) and active (*A*) conformations are shown with double arrows indicating the transition between states. Horizontal arrows between modules indicate the coupling between domains.

To quantify the energetic differences between $SthK_{Cterm}$ and $SthK_{Full}$ as well as begin to fill in all structural and energetic values of our modular getting scheme in SthK, we need a technique that can measure both the conformational changes and energetics of each individual module. While methods like electrophysiology and structural studies have advanced our understanding of gating energetics, they are limited in resolving conformational changes, coupling, and state heterogeneity in domains outside the pore. Therefore, a technique is needed that can directly reveal both structural information and the relative proportion of structural states for individual protein domains. Such a method must be adaptable to various domain topologies and capable of measuring a range of distance distributions to provide a comprehensive view of the channel gating mechanism. Time-resolved tmFRET, meets these requirements by using fluorescence lifetimes to quantify distance distributions between a fluorophore donor and a metal ion acceptor, offering insights into both structural and energetic changes. Importantly, the donor and acceptor molecules can be incorporated into both soluble and membrane proteins structures and the technique is broadly applicable across various experimental conditions, providing a versatile tool for studying ion channel dynamics. The theoretical framework of time-resolved tmFRET has been outlined in depth in past work and previous chapters (15, 19–22).

To apply time-resolved tmFRET approach to full-length SthK channels, we first extended our method to measuring lifetimes in the time-domain using time-correlated single photon counting (TCSPC) data. Although fluorescence lifetimes can be measured using either frequency-domain or time-domain methods comparably, we believe that this TCSPC data approach provides several advantages over our previously utilized microscope setup for frequency-domain lifetimes. As membrane protein expression and purification is challenging, we needed an approach that allowed us to use much lower concentrations of protein than required for our previous experiments. The TCSPC cuvette-based instrument has a longer pathlength than on an imaging microscope and therefore allowed us to use ~10-fold lower protein concentrations. Additionally, we sought a method for measuring tmFRET that would allow us to use a simpler noise model than required for frequency domain measurements, giving better model comparability and compatibility with more advanced statistical analyses in the future. TCSPC directly records photon arrival times after fluorophore excitation, and builds a histogram of arrival times, meaning that the noise in these measurements is due to a well-defined Poisson distribution of single photon emissions (22). Photon arrival histograms from the fluorophore can

be analyzed with either a single- or multi-exponential decay model depending on the shape of the histogram. In the presence of FRET, the apparent fluorescence lifetime decreases and the histogram of photon arrival times will be shifted to shorter arrival times. Like in frequency domain measurements, TCSPC data can be fit with a distribution of distances that describes the amount of measured FRET. This distribution of distances can account for both the heterogeneity within a state and the heterogeneity between states. This heterogeneity between conformational states, is directly related to the energetics of conformational transitions through the Boltzmann relationship and thus Gibbs free energy change, ΔG, can be obtained between the states.

In this study, we used time-resolved tmFRET with TCSPC to measure the ligand-induced conformational changes in SthK's CNBD, first in the isolated C-terminal fragment, $SthK_{Cterm}$, and then in the full-length channel, $SthK_{Full}$. Distance distributions were obtained for both $SthK_{Cterm}$ and $SthK_{Full}$ in the presence and absence of ligand. This allowed for calculation of ΔG_{apo} and ΔG_{cAMP} in each construct to determine the energetic contribution of coupling to the pore domain. These findings additionally validate the use of TCSPC data in time-resolved tmFRET and demonstrate its capability to measure unique distance distributions across different protein constructs for energetic analysis. Ultimately, these results contribute to a deeper understanding of the allosteric mechanism of ligand gating in SthK.

Results

To make a direct comparison between the energetics of $SthK_{Cterm}$ and $SthK_{Full}$ constructs, we needed to follow a couple sequential experimental steps. 1) We first validated the TCSPC method with tmFRET using our previously published $SthK_{Cterm}$ construct. Rather than comparing across the different lifetime measurement techniques, measurements of $SthK_{Cterm}$ and $SthK_{Full}$ both utilizing TCSPC data would give a more direct comparison and allow for global fitting methods of our data. 2) In $SthK_{Full}$ which are homotetramers of identical subunits, there is the potential for some intersubunit FRET, which was avoided in our $SthK_{Cterm}$ frequency domain results by using an of excess unlabeled subunits. We thus quantified the amount of intersubunit FRET possible with all four labeled subunits in our $SthK_{Cterm}$ system by mixing subunits that contained only a single donor-labeled subunit with an excess of subunits containing only acceptor-labeled sites. 3) To ensure that we could account for this intersubunit FRET component

in homotetrameric SthK protein, we measured the intrasubunit FRET distance distribution of homotetrameric $SthK_{Cterm}$. 4) Finally, this intrasubunit distance distribution from homotetrameric $SthK_{Cterm}$ was compared to TCSPC data and distances obtained from $SthK_{Full}$ in the same experimental setup.

Validation of Time-Resolved tmFRET Using TCSPC in $SthK_{Cterm}$

To first validate our time-resolved tmFRET approach using TCPSC, we started with our previously published construct of the C-terminal fragment of SthK ($SthK_{Cterm}$) (15). This allowed us to compare distance distributions obtained through TCSPC data and those previously obtained through frequency domain fluorescence lifetime intensity microscopy (FLIM) data in the same protein construct. In these experiments, $SthK_{Cterm}$, comprised of the isolated C-linker domain and CNBD, was expressed with the noncanonical amino acid acridon-2-ylalanine, Acd, at site S361 and a cysteine at site V416 for metal-ion acceptor conjugation. As previously described, $SthK_{Cterm}$ incorporating Acd was purified and mixed with excess WT unlabeled $SthK_{Cterm}$, to create heterotetrameric $SthK_{Cterm}$-WT:$SthK_{Cterm}$-S361Acd-V416C protein ($SthK_{Cterm}$:WT/361Acd-V416C, cartoon in Figure 2A) and to eliminate the possibility of FRET between neighboring subunits. In parallel, SthKCterm:WT/361Acd-V416C (with a cysteine) and SthKCterm:WT/361Acd (donor only, without any cysteines) protein constructs were incubated with the thiol-specific metal ion acceptor $[Ru(bpy)_2phenM]^{2+}$. This acceptor has an R_0 = 43.5 Å when paired with Acd, where R_0 is the distance at which FRET efficiency is 0.5 (structures of donor and acceptor labels shown in Figure 2A) (23). The labeled protein was run on size exclusion chromatography (SEC) to remove unreacted $[Ru(bpy)_2phenM]^{2+}$ as well as any monomeric protein and the purified tetrameric protein was used immediately in fluorescence lifetime experiments.

We collected fluorescence lifetime data in the form of TCSPC decays of our Acd-incorporated protein. First, the donor-only SthKCterm:WT/361Acd was measured and the photon arrival times are shown on a normalized log scale histogram (grey decay trace, Figure 2B). We observed that this lifetime, while approximating a single-exponential decay, was best fit with a double exponential decay, with 87% of the amplitude arising from a 17.6 ± 0.02 ns lifetime and the remaining contribution from a second 4.73 ± 0.13 ns lifetime. The $SthK_{Cterm}$-

S361Acd donor-only protein lifetime did not significantly change in the presence of cAMP as expected (orange trace, Figure 2B). This lifetime is very similar to what was previously described for Acd in the same protein using frequency domain lifetime measurements (15). To ensure that any lifetime changes would be due FRET alone, the donor only construct was measured in the same way (in the presence of $[Ru(bpy)_2phenM]^{2+}$) and under the various cAMP concentrations, as the cysteine-containing constructs. The donor only lifetimes for each condition were then used as fixed starting lifetimes when analyzing the amount of FRET in our cysteine-containing protein.

Decay traces were then measured for the $SthK_{Cterm}$:WT/361Acd-V416C-$[Ru(bpy)_2phenM]^{2+}$ protein, in the absence of ligand (black trace, Figure 2B). As expected, labeling this construct with $[Ru(bpy)_2phenM]^{2+}$ shortened the overall lifetime of Acd compared to the donor-only lifetime due to FRET between the donor and acceptor. In addition to shortening the overall lifetime decay, the decay profile became more multi-exponential, indicative of multiple donor-acceptor distances contributing to the FRET. Subsequently, upon the addition of a subsaturating concentration of 1 μM cAMP the Acd decay rate (blue trace, Figure 2B) became even shorter compared to the apo state and decreased even further upon addition of a saturating concentration of 320 μM cAMP (red trace, Figure 2B). This decrease in the fluorescence lifetime, indicates increased FRET and shorter distances between the donor and acceptor molecules in response to cAMP. Overall, this cAMP-induced shift to shorter lifetimes, compared with our control without acceptor, demonstrate that our TCSPC approach has the sensitivity to measure ligand-triggered conformational changes in the CNBD of $SthK_{Cterm}$.

The TCPSC decay traces from $SthK_{Cterm}$:WT/361Acd-V416C-$[Ru(bpy)_2phenM]^{2+}$ were then fit with a model that assumes that a distribution of donor-acceptor distances produces the measured lifetime changes due to FRET. We parameterized the distance distribution as the sum of two Gaussians, each with an average distance ($\bar{r}$) and a standard deviation (σ), as well as fraction A_2 describing the relative contribution of each Gaussian. These two Gaussians represent the resting and active conformational states of the CNBD C-helix. This time-resolved lifetime distance distribution model is the same as was used with our previously published frequency domain measurements (15, 20–22); however, the model has been adapted to TCSPC lifetime data (see Materials and Methods.)

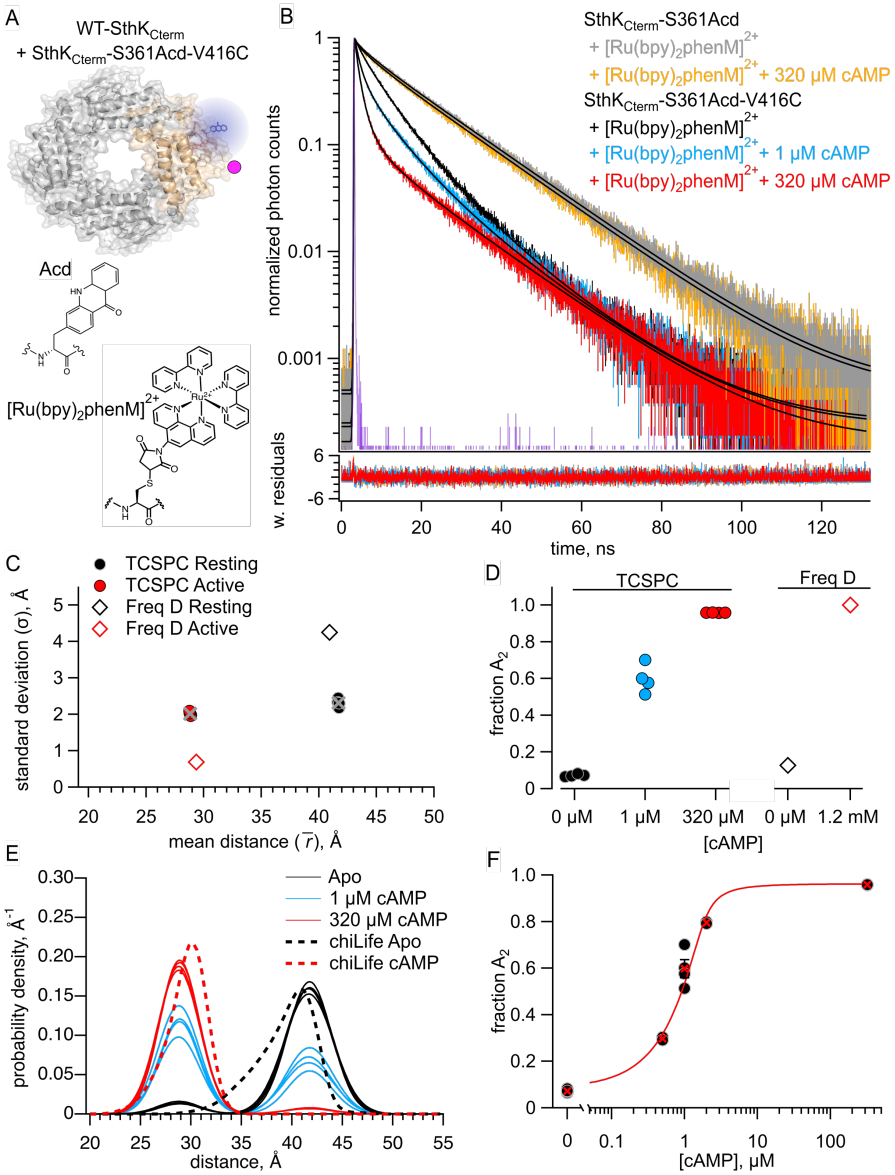

Figure 2. Fluorescence TCSPC data from WT-heterotetrameric-SthK$_{Cterm.}$ (**A**) Cartoon of SthK$_{Cterm}$:WT/361Acd-V416C with single labeled donor and acceptor subunit, and corresponding structures of donor fluorophore, Acd, and acceptor metal complex [Ru(Bpy)$_2$phenM]$^{2+}$. (**B**) Representative TCSPC decays from SthK$_{Cterm}$:WT/361Acd with [Ru(Bpy)$_2$phenM]$^{2+}$ (grey) and upon addition of 320 µM cAMP (orange). Decays from SthK$_{Cterm}$:WT/361Acd-V416C with [Ru(Bpy)$_2$phenM]$^{2+}$ (black) and upon 1 µM cAMP (blue), and 320 µM cAMP (red). Instrument response function (IRF) trace shown in purple and weighted residuals for respective fits from lifetime model are below. (**C**) Summary of Gaussian fit parameter values, $\bar{r}$ and σ (n = 4), and frequency domain FLIM averages for comparison (red and black diamonds). (**D**) Fraction A$_2$ fit values from apo, 1 µM and 320 µM cAMP compared with frequency domain averages (diamonds). (**E**) Spaghetti plot of distance distributions for individual experiments shown for apo (black), 1 µM cAMP (blue) and 230 µM cAMP (red). Resting (black) and active (red) computational chiLife distributions overlayed as dashed lines. (**F**) Summary of fraction A$_2$ over range of cAMP concentrations fit with a quadratic (red curve, K$_d$ = 0.22 ± 0.08 µM, [protein] = 1.2 µM).

We globally fit the decay traces from apo, and a range of cAMP concentrations (0.5, 1, 2, 320 μM) and the fits are overlayed on the representative traces in Figure 2B, with corresponding weighted residuals shown below the traces. These fits converged with a reduced χ^2 values near 1 and the parameters were well-identified (see Materials and Methods). The $\bar{r}$s and σs for the resting and active state Gaussians from different experiments are summarized in Figure 2C, with an average distance $\overline{r_1}$ = 41.7 Å and σ_1 = 2.3 Å in the resting state and $\overline{r_2}$ = 28.8 Å and a σ_2 = 2.1 Å in the active state. These values were similar to our previously published frequency domain results of this same donor-acceptor sites obtained with FLIM, which gave $\overline{r_1}$ = 40.9 Å with σ_1 = 4.3 Å in the resting state and $\overline{r_2}$ = 29.5 Å and σ_2 = 0.84 Å in the active state. The fraction of the distribution in the active state, fraction A_2, was best fit with 8% in the absence of ligand and 96% in the presence of a saturating concentration of cAMP. Our previous frequency domain measurements gave values for fraction A_2 that were similar to those obtained using TCSPC (12% in the absence of cAMP and 100% in the presence of a saturating concentration of cAMP, Figure 2C). A summary of distributions from individual experiments for apo, 1 μM, and 320 μM cAMP (a saturating concentration), can be seen in the spaghetti plot in Figure 2E. Overlayed on the spaghetti plots are the distance distributions computationally derived from known structures with chiLife (15). These structurally predicted distance distributions show a remarkable similarity to those based on fits to our experimental data. The fraction A_2 values measured across a range of subsaturating concentrations of cAMP are displayed as a dose response curve and fit with a quadratic equation assuming no binding cooperativity (K_D = 0.22 ± 0.08 μM, Figure 2F). This K_D value is comparable to the value obtained using steady-state tmFRET (15). The distance distributions obtained here with TCSPC data are quite close to those measured previously for this same donor-acceptor pair in the frequency domain and the chiLife computational predictions for the resting and active states. We felt confident given these results that TCSPC data and labeling with the $[Ru(bpy)_2phenM]^{2+}$ acceptor alone could obtain reasonable distance distributions in our system.

Intersubunit FRET In Homotetrameric $SthK_{Cterm}$

Our ultimate goal of examining conformational energetics in full length SthK, which includes the membrane spanning domains, presents an additional experimental challenge. Unlike

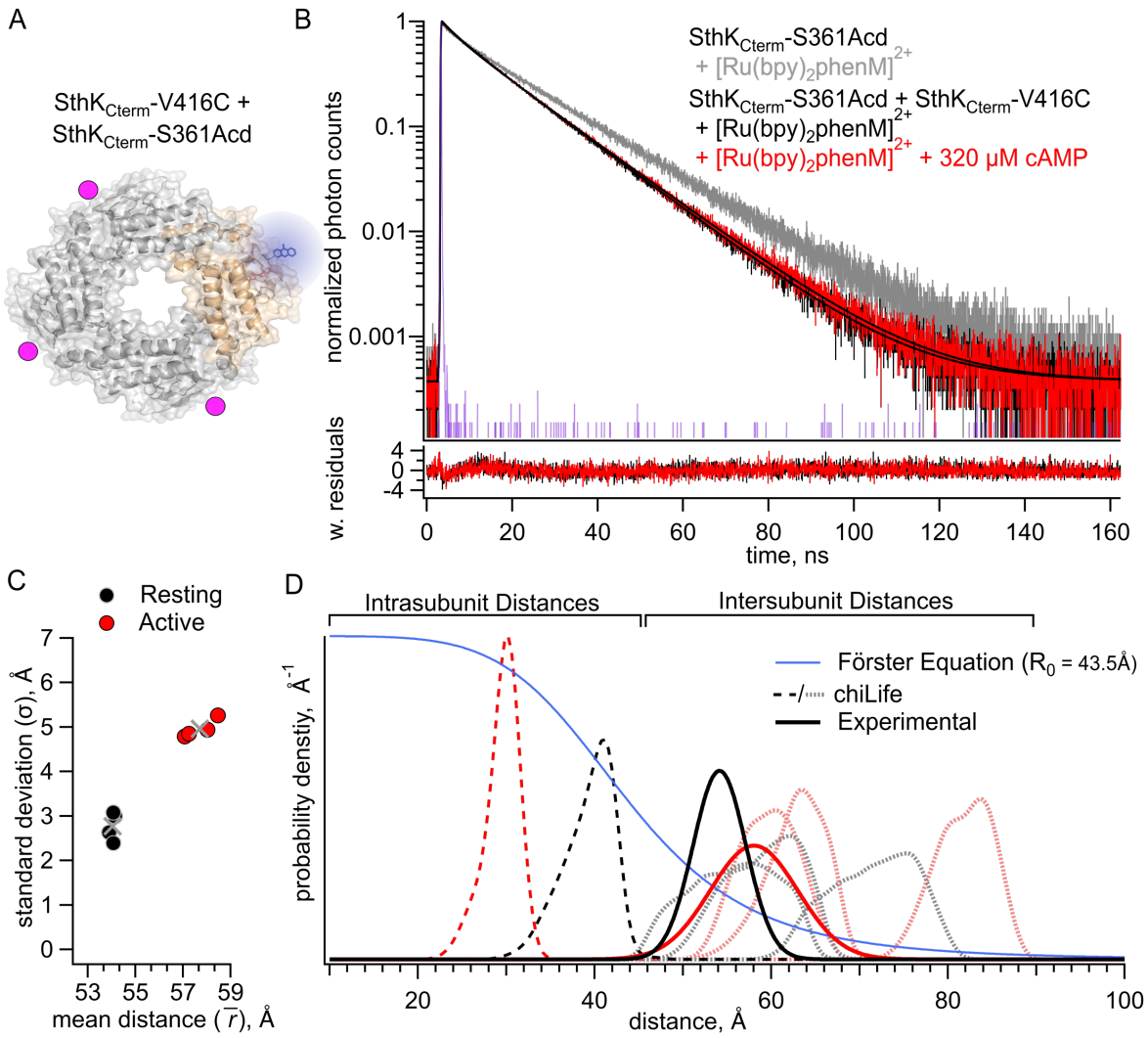

Figure 3. Experimental measure of intersubunit FRET. **(A)** Cartoon structure of SthK$_{Cterm}$:V416C/S361Acd construct with 3 acceptor SthK$_{Cterm}$:V416C subunits to one SthK$_{Cterm}$:S361Acd. **(B)** Representative TCSPC decay traces from SthK$_{Cterm}$:S361Acd donor only decay (in grey), the heterotetramer SthK$_{Cterm}$:V416C/S361Acd protein in the presence of [Ru(Bpy)$_2$phenM]$^{2+}$ (black) and then upon addition of 320 µM cAMP (red). Matching IRF shown in purple and weighted residuals for fits from lifetime model shown below for respective traces. **(C)** Summary of Gaussian fit parameter values, $\bar{r}$ and σ, for individual experiments in circles (n = 4) and averages as cross marks. **(D)** chiLife distance distribution predictions between donor and acceptor molecule within a subunit (darker dashed curves) and between the three other subunits (lighter dashed curves) where black = resting and red = active. The experimentally obtained distance distributions for resting and active are overlayed as solid black and red Gaussians.

in the C-terminal fragment in which it is straightforward to make heterotetramers with only a single labelled subunit, at this time we can only express and purify full length SthK as homotetramers. These homotetramers would, of necessity, have donors and acceptors in all subunits and thus could have some intersubunit FRET. To address the contribution of intersubunit FRET, we measured FRET between Acd incorporated into only a single $SthK_{Cterm}$:S361Acd subunit (with no acceptor cysteine) and $[Ru(bpy)_2phenM]^{2+}$ acceptor labeled on the remaining three $SthK_{Cterm}$:V416C subunits, by mixing an excess (>7:1 molar ratio) of $SthK_{Cterm}$:V416C protein with $SthK_{Cterm}$:S361Acd (Figure 3A). This construct, $SthK_{Cterm}$:WT-V416C/S361Acd, in which only intersubunit FRET was possible, showed faster lifetime decays than the control donor-only construct ($SthK_{Cterm}$:WT/S361Acd), both in the absence and presence of cAMP, as seen by the black and red representative traces in Figure 3B. To quantify this intersubunit FRET, we fit these data with a model representing the distance distribution as the sum of two Gaussians, which gave parameter values of $\overline{r_1}$= 54.1 Å and σ_1 = 3.0 Å in the resting sate, and $\overline{r_1}$ = 58.0 Å and σ_1 = 5.0 Å in the active state (see methods, Figure 3C). The resting and active distributions aligned extremely well with the intersubunit distance distributions predicted by chiLife (Figure 3D). Indeed, the fits most closely aligned with the shortest predicted intersubunit distance, conforming to expectations that the closest distances would dominate the FRET. Based on these results, we conclude that our experiments with homotetrameric full-length protein, with all four subunits labeled with donor and acceptor, must take into account this intersubunit FRET.

TCSPC Measurements in Homotetrameric $SthK_{Cterm}$

Now that quantified the intersubunit FRET in our tetramer system, we were able to measure the intrasubunit FRET in homotetrameric $SthK_{Cterm}$:S361Acd-V416C protein labeled with $[Ru(bpy)_2phenM]^{2+}$ ($SthK_{Cterm}$:361Acd-V416C-$[Ru(bpy)_2phenM]^{2+}$, Figure 4A). We measured TCSPC traces for this construct in the absence of cAMP and presence of either 1 or 320 μM cAMP (Figure 4B). To account for the contributions from intersubunit FRET, we added a second FRET acceptor to the experimentally determined intersubunit distance distribution in our lifetime FRET model (Figure 3C, see Materials and Methods). The fits from this model are overlayed on the lifetime data in Figure 4B, with weighted residuals shown below and gave intrasubunit distribution values of $\overline{r_1}$ = 41.6 Å and a σ_1 = 3.6 Å and $\overline{r_2}$ = 29.1 Å with σ_2 = 4.1 Å,

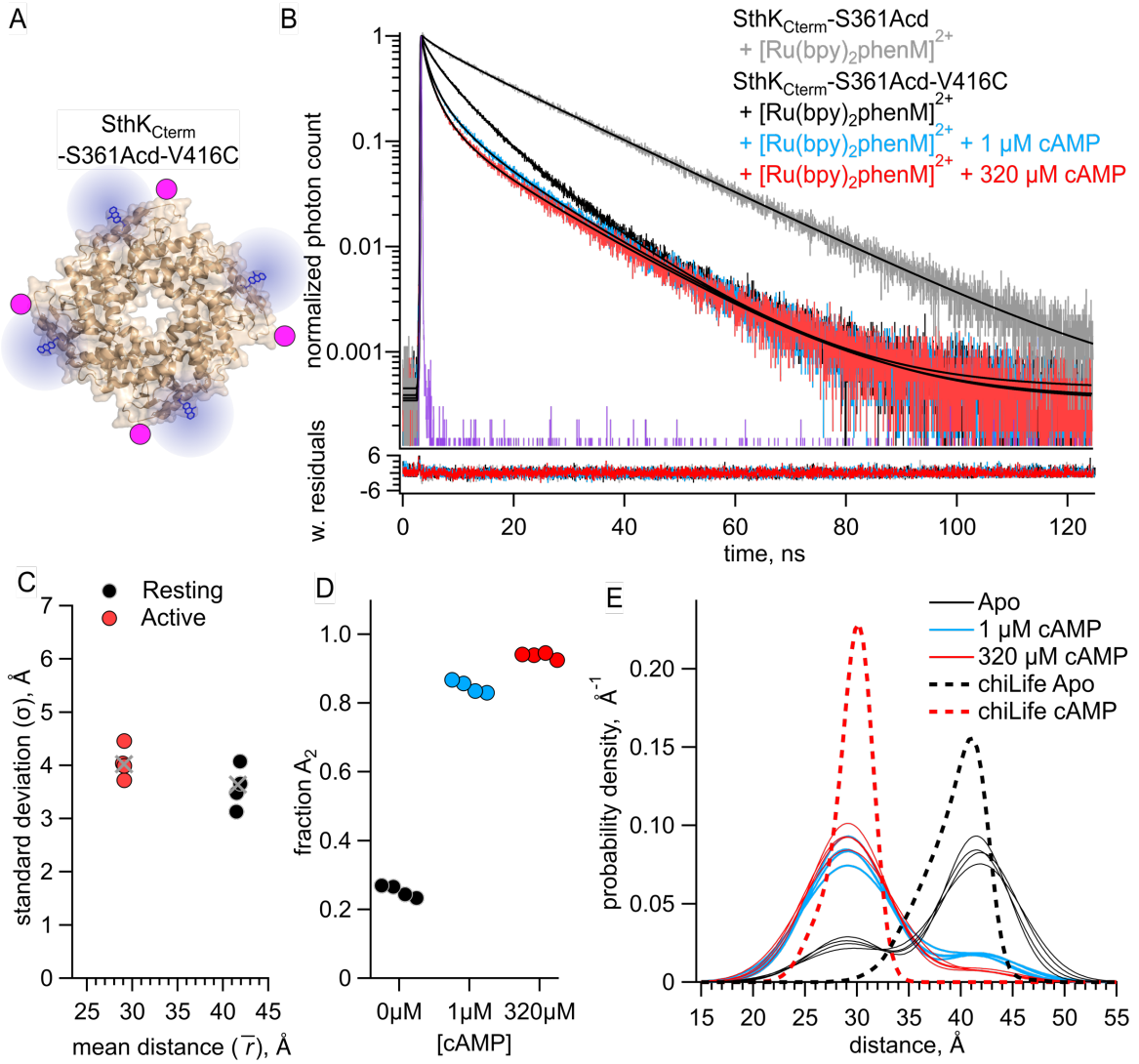

Figure 4. Fluorescence lifetime data from homotetrameric SthK$_{Cterm}$. **(A)** Cartoon structure of homotetrameric SthK$_{Cterm}$:S361Acd-V416C construct. **(B)** Representative TCSPC decay traces for SthK$_{Cterm}$:S361Acd (in grey), the SthK$_{Cterm}$:S361Acd-V416C protein in the presence of [Ru(Bpy)$_2$phenM]$^{2+}$ (black), and then upon the addition of 1 µM cAMP (blue) and 320 µM cAMP (red). Matching IRF shown in purple and weighted residuals for fits from lifetime model shown below for respective traces. **(C)** Summary of Gaussian fit parameter values, $\bar{r}$ and σ, for individual experiments in circles (n = 4) and averages as cross marks. **(D)** Individual fit values and averages for fraction A$_2$ from apo, 1 µM and 320 µM cAMP. **(E)** Spaghetti plot of distance distributions for individual experiments shown for apo (black), 1 µM cAMP (blue), and 320 µM cAMP (red). Resting (black) and active (red) computational chiLife distributions overlayed as dashed curves.

for the resting and active states (Figure 4C). These $\bar{r}$ values are similar to those obtained from $SthK_{Cterm}$:WT/361Acd-V416C-$[Ru(bpy)_2phenM]^{2+}$, with somewhat wider σ values particularly in the active state. Interestingly, the distribution among states in the homotetramer, with a fraction $A_2 = 0.25$ in the absence of ligand, and fraction $A_2 = 0.94$ in the presence of a saturating concentration of ligand, was somewhat different from the WT-heterotetramers (Figure 4D). This suggests a slightly more favorable closing of the C-helix in the absence of cAMP and slightly less favorable closing in the presence of saturating cAMP in $SthK_{Cterm}$:361Acd-V416C-$[Ru(bpy)_2phenM]^{2+}$. Additionally, the 1 μM cAMP concentration also seemed to slightly increase favorability of C-helix closure compared to in the heterotetramer protein. A summary of distance distributions from different experiments across apo, 1 μM, and 320 μM cAMP is shown as a spaghetti plot in Figure 4E, with the chiLife predictions overlayed as dashed curves. Based on these data, we concluded that differences in the distribution among resting and active Gaussians that we observed between the homotetrameric protein and the heterotetrameric protein is minimal.

The slight variation in relative proportions of resting and active Gaussians between homotetrameric and the heterotetrameric constructs could arise from two primary reasons: 1) a different amount of intersubunit FRET in our homotetrameric protein than we experimentally measured and accounted for in our fits or 2) additional energetic effects due to the presence of four donor-acceptor labels in homotetramers. Considering that the experimentally derived intersubunit FRET closely paralleled the computational chiLife distributions, we think our assessment of intersubunit FRET was reasonable. Even when the chiLife distributions were used as the additional intersubunit FRET distributions in our analysis instead of the experimental distributions, very similar Gaussian proportions were obtained (data not shown). We noticed however, that in the preparation of the different tetrameric protein samples, the ability for the constructs to tetramerize were not the same. As observed in SEC, the same relative protein concentrations (as determined by absorbance at 280 nm), had a lower proportion of tetrameric protein for $SthK_{Cterm}$:S361Acd-V416C compared to $SthK_{Cterm}$:WT/S361Acd-V416C (Figure 4, figure supplement 1). This lower tetramerization ratio was also observed with homotetrameric $SthK_{Cterm}$:S361Acd, but not for the heterotetrameric $SthK_{Cterm}$:V416C/S361Acd construct. It is therefore possible that Acd incorporation at this residue position affects the energetics of tetramerization and alters the conformational equilibrium between resting and active states of the

C-helix. This would appear more substantial in the homotetrameric protein than in the heterotetrameric protein. Regardless of the exact cause of this energetic change observed between the WT-heterotetrameric $SthK_{Cterm}$ and homotetrameric $SthK_{Cterm}$, when comparing between $SthK_{Cterm}$ and $SthK_{Full}$, this energetic component should be equivalent, allowing us to make a direct comparison of distance distributions and coupling energetics.

Full-Length SthK Acd Incorporation and Purification

Having established a method to account for intersubunit FRET, we expressed and purified full-length SthK protein ($SthK_{Full}$) using the same Acd site at residue 361, either with or without a cysteine at the same acceptor position 416. These constructs were expressed in *E.coli*, where membrane fractions were isolated and solubilized in n-Dodecyl-β-D-maltoside (DDM) detergent with 10:1 cholesteryl hemisuccinate (CHS). The $SthK_{Full}$ was then purified using StrepTactin affinity resin and the DDM detergent was exchanged for Lauryl Maltose Neopentyl Glycol (LMNG) detergent + CHS on the StrepTactin column (Figure 5A). $SthK_{Full}$:S361Acd-V416C (with cysteine) and $SthK_{Full}$:S361Acd (without cysteine) were successfully purified as confirmed with in-gel fluorescence (Figure 5B). Coomassie staining showed a small proportion of protein subunits (< 15%) appeared truncated at the TAG codon site for Acd incorporation, which co-assembled with full-length subunits. Size exclusion chromatography showed predominantly a single peak in Acd fluorescence without aggregates, indicating well solubilized and well-behaved protein (Figure 5C).

TCSPC Data of Full-Length SthK

We measured the fluorescence lifetimes of both purified constructs, $SthK_{Full}$:S361Acd and $SthK_{Full}$:S361Acd-V416C, before and after labeling with $[Ru(bpy)_2phenM]^{2+}$ acceptor with TCSPC (Figure 6A). The lifetimes of $SthK_{Full}$:S361Acd donor-only protein were again best fit with a double exponential decay (grey trace, Figure 6B) and addition of cAMP did not change the lifetime (orange trace, Figure 6B). These lifetimes values were close to those measured in the $SthK_{Cterm}$ construct indicating no large change in environment of the fluorophore between constructs. In comparison to $SthK_{Full}$:S361Acd, the $SthK_{Full}$:S361Acd-V416C gave significantly shortened lifetime decays upon labeling with $[Ru(bpy)_2phenM]^{2+}$ (representative trace in black, Figure 6B). The addition of a range of cAMP concentrations (0.25, 0.5, 1, 2 and 320 μM) to

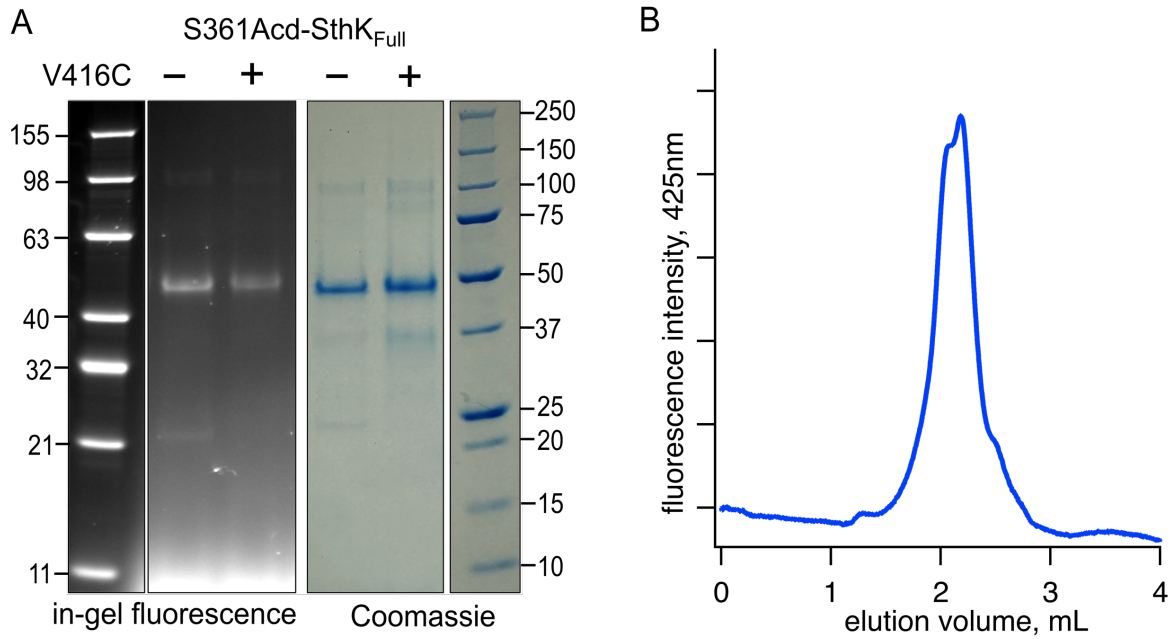

Figure 5. Acd incorporation into SthK$_{Full}$ expression and purification. **(A)** Protein SDS page gel showing in-gel fluorescence for SthK$_{Cterm}$:S361Acd (left) and SthK$_{Cterm}$:S361Acd-V416C (right) at correct mass (triangles, theoretical mass = 53.0 kDa), along with Coomassie stain for same gel on right. **(B)** Size exclusion chromatography for SthK$_{Cterm}$:S361Acd-V416C on Superose6 5/150 showing fluorescence at 420 nm.

$SthK_{Full}$:S361Acd-V416C protein further decreased the lifetimes in a concentration-dependent manner, following the same trend as was observed in the $SthK_{Cterm}$ protein (representative decays for 0.5 μM cAMP in blue, and 320 μM cAMP saturating concentration in red, in Figure 6B).

We fit the decay traces from $SthK_{Full}$ with the lifetime FRET model that includes the intrasubunit and intersubunit FRET contributions (see Figure 4). The model fits are overlayed on the representative decay traces in Figure 6B, with corresponding weighted residuals shown below. We found that the best fit for the dataset (across all protein repeated trials) had average parameter values of $\bar{r_1}$ = 39.8 Å and a σ_1= 4.1 Å and $\bar{r_2}$ = 31.0 Å with σ_2 = 2.7 Å for the resting and active state Gaussians, respectively. A summary of $\bar{r}$ and σ values for individual experiments is shown in Figure 6C. The parameter values are noticeably similar to those obtained from homotetrameric $SthK_{Cterm}$, particularly for $\bar{r}$s, which were within 1.5 Å of those previously measured for both the resting and active states (Figure 4C). Interestingly, the σ values for the active state were narrower than in the resting state, which suggests a decreased heterogeneity of the ligand-bound state relative to the apo state as expected. The fraction A_2 showed $SthK_{Full}$ had a higher probability of being in the active state both in the absence of cAMP and in the presence of a saturating concentration of cAMP (apo fraction A_2 = 0.36, cAMP fraction A_2 = 1) compared to $SthK_{Cterm}$ (Figure 6D). The distance distributions for the different $SthK_{Full}$ experiments are summarized in spaghetti plots in Figure 6E. Across a range of subsaturating cAMP concentrations, fraction A_2 showed intermediate values between those obtained from apo and saturating cAMP (Figure 6F). This relationship was fit with a quadratic equation to give a K_D = 0.52 ± 0.04 μM, which is similar to that obtained from the $SthK_{Cterm}$ but substantially lower than the K_D reported from WT-SthK electrophysiology experiments (K_D = 1.5 μM) (12). Overall, in $SthK_{Full}$ with the presence of pore and transmembrane domains, as well as detergent environment, we observed similar resting and active state distances ($\bar{r}$ and σ) for the CNBD C-helix and different relative proportions between these states (fraction A_2).

To focus on changes in the fraction A_2 in $SthK_{Full}$ compared to $SthK_{Cterm}$, we globally fit the data from both protein constructs assuming that $\bar{r}$ and σ would be the same in both constructs. We believe this assumption is reasonable considering that the cryoEM structure of the full-length SthK channel in the cAMP bound and activated state (PDB: 7RTJ) closely aligns with the X-ray crystal structure of C-terminal SthK with cAMP bound (PDB:4D7T). Additionally, the

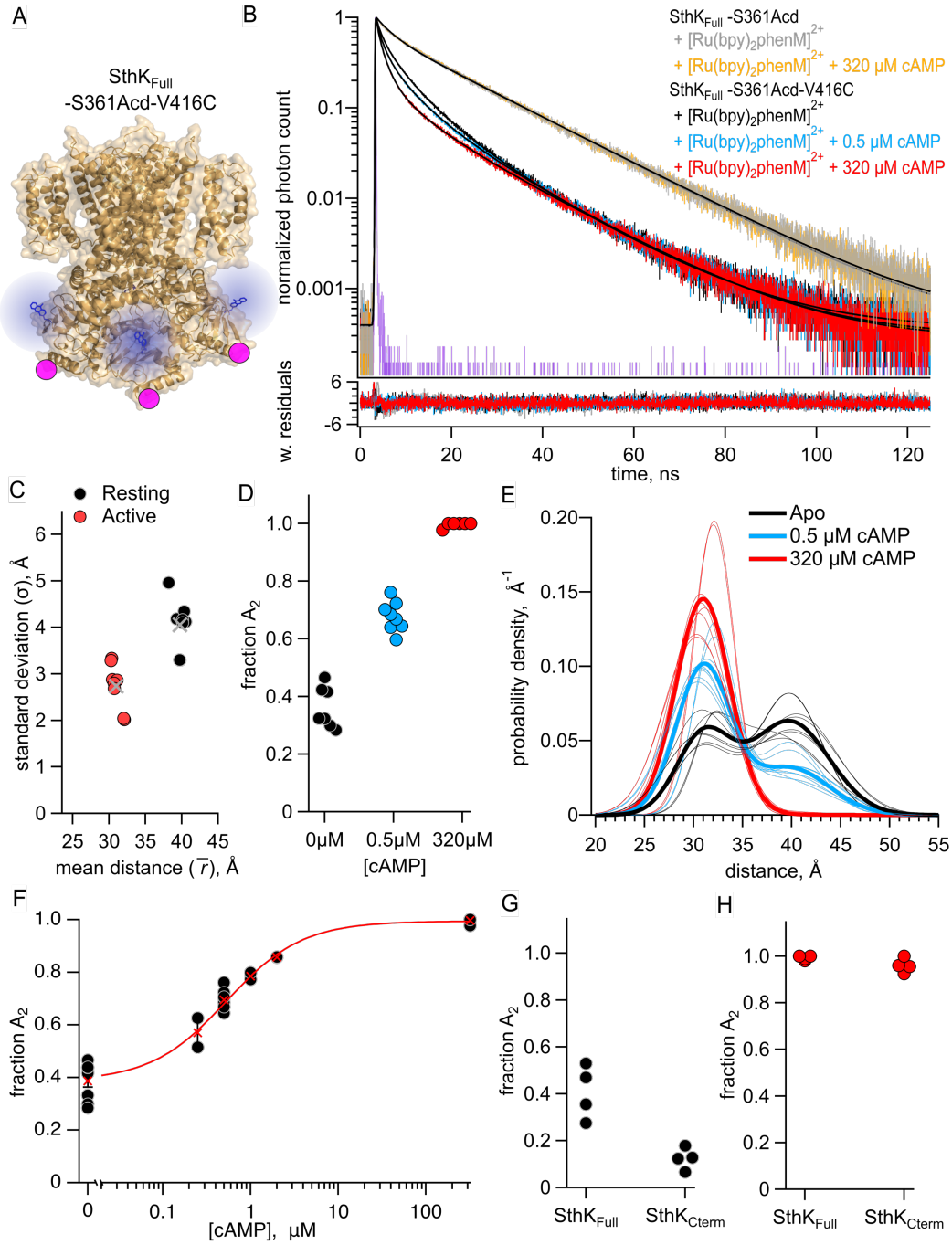

Figure 6. Fluorescence lifetime data from SthK$_{Full}$. **(A)** Cartoon structure of SthK$_{Full}$:S361Acd-V416C construct. **(B)** Representative TCSPC decays for SthK$_{Full}$:S361Acd donor upon addition of [Ru(Bpy)$_2$phenM]$^{2+}$ (grey) followed by 320 µM cAMP (orange) and SthK$_{Full}$:S361Acd-V416C with acceptor (black), upon addition of 0.5 µM cAMP (blue) and 320 µM cAMP (red). Matching IRF (purple) and weighted residuals for fits shown below. **(C)** Summary of Gaussian fit parameter values, $\bar{r}$ and σ, for individual experiments (n = 8). **(D)** Parameter fraction A$_2$ for apo, 0.5 µM and 320 µM cAMP. **(E)** Spaghetti plot of distance distributions for individual experiments (thin curves) shown for apo (black), 0.5 µM cAMP (blue) and 320 µM cAMP (red) and averaged fit parameters (thick curves). **(F)** Summary of fraction A$_2$ over range of cAMP concentrations, fit with quadratic equation (K$_{1/2}$ = 0.53 µM, *h*= 1). **(G-H)** Fraction A$_2$ values from globally fitting SthK$_{Full}$ and SthK$_{Cterm}$ constructs.

chiLife computational distributions were based on the cryoEM full-length SthK structure in the apo state (PDB: 7RSH), which we found correlated well to the experimental $SthK_{Cterm}$ tmFRET distance distributions (Figure 2E) (14). Lastly, we believe that the effect of coupling between the pore and the CNBD most likely changes only the energetics of the CNBD transition, and not its structures, based on the modular gating scheme in Figure 1. This is supported by the observation that changes in distance distributions arising from Acd labeling (Figure 4 and Figure 4 – supplemental figure 1) did not seemingly change the end structural distances ($\bar{r}$ values), but rather the heterogeneity within a state (σ values) and the fraction A_2. Our global fit of both $SthK_{Cterm}$ and $SthK_{Full}$ included data in the absence of cAMP and a saturating concentration of cAMP and used the lifetime FRET model with both intersubunit and intrasubunit FRET. Whereas the resting and active states average distances ($\bar{r}$) and standard deviations (σ) were constrained to be the same across both types of protein, the fraction A_2 was allowed to vary across each type of protein and cAMP concentration. The best fit to both datasets yielded $\bar{r_1}$ = 40.5 Å with σ_1= 4.1 Å, and $\bar{r_2}$ = 30.5 Å with σ_2 = 3.3 for the absence of cAMP and a saturating concentration of cAMP, respectively. As in fits to each dataset independently (Figure 4D and Figure 6D), the globally fit fraction A_2 differed between the protein constructs, with $SthK_{Full}$ (apo A_2= 0.41, cAMP A_2=0.99) giving a higher fraction A_2 in both the absence of cAMP and the presence of a saturating concentration of cAMP, compared to $SthK_{Cterm}$ (apo A_2= 0.12, cAMP A_2=0.96) (Figure 6 G and H).

The proportion of molecules in each state can be converted into energetic terms in the form of Gibbs free energy in the context of the modular gating scheme in Figure 1B. A summary of the energetics for this conformational transition of the C-helix is shown in Figure 7, based on the global fits across the $SthK_{Cterm}$ and $SthK_{Full}$ datasets. In $SthK_{Cterm}$ protein construct, the resting to active conformational transition is unfavorable in the absence of ligand (ΔG = +1.15 Kcal/mol), which is made more favorable in the presence of saturating cAMP (ΔG = -1.87 Kcal/mol). In comparison, in $SthK_{Full}$ with attached pore and transmembrane domains, the resting to active transition without ligand is still unfavorable (ΔG = + 0.22 Kcal/mol), but more favorable than in $SthK_{Cterm}$, while the presence of cAMP stabilizes the transition even further (ΔG = -2.87 Kcal/mol). This suggests that the direction of coupling between the pore and the cytoplasmic domains stabilizes the active state of the CNBD by about -1 Kcal/mol. According to

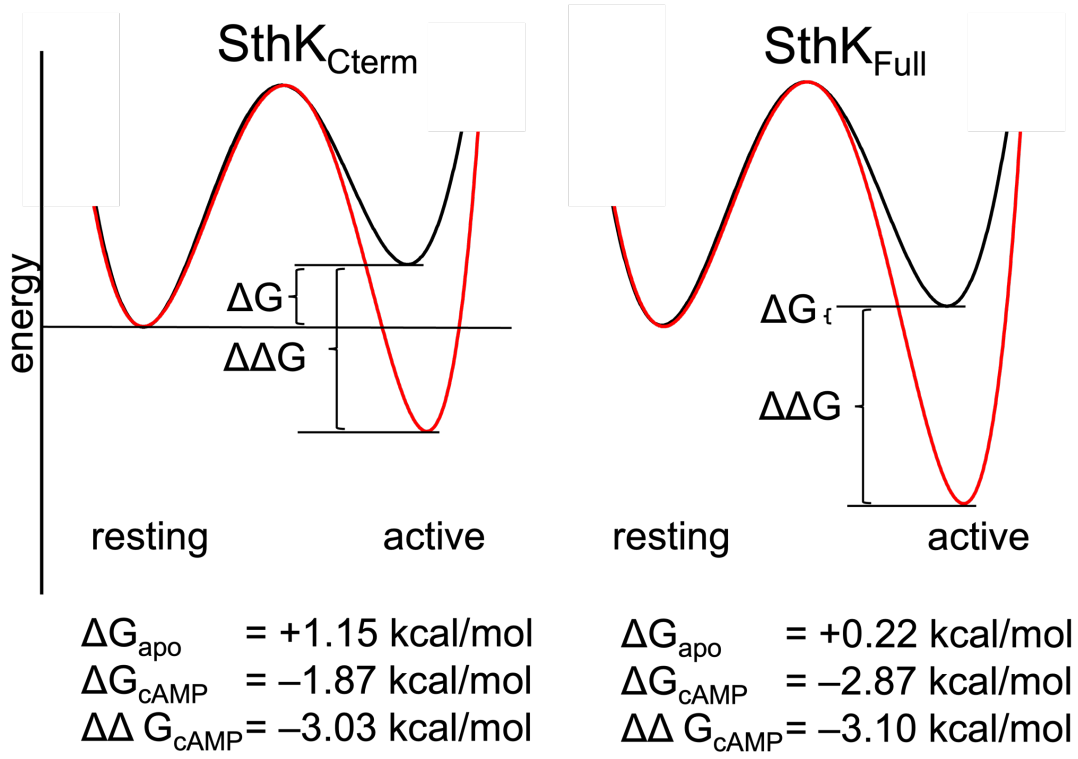

Figure 7. Summary of energetics as reaction coordinate for transition of the C-helix CNBD upon cAMP binding. A hypothetical energy landscape showing the relative energy difference between resting and active states (ΔG and associated arrow) without ligand (black) and with cAMP (red), for SthK$_{Cterm}$ (left) and SthK$_{Full}$ (right). The difference in free energy change (ΔΔG and associated arrow) is shown between the resting state in the absence of ligand and resting state in presence of ligand. Calculated ΔG and ΔΔGs are shown in Kcal/mol for each construct below the diagram.

the modular gating scheme, while domain coupling may alter ΔG values in each state, it should not affect the difference in change of free energy (ΔΔG) produced by cAMP. Interestingly, the ΔΔG between $SthK_{Cterm}$ and $SthK_{Full}$ were remarkably close with the ΔΔG of $SthK_{Cterm}$ = -3.03 Kcal/mol and ΔΔG of $SthK_{Full}$ = -3.10 Kcal/mol, suggesting that the modular gating scheme captures the most salient features of our datasets.

Discussion

This work utilized time-resolved tmFRET with TCSPC lifetime data to investigate the ligand-mediated allosteric mechanism in the CNBD ion channel SthK. With this technique, we measured distance distributions associated with the conformational transition of the CNBD C-helix across different protein constructs and quantified the effect of domain coupling on this transition in $SthK_{Full}$. Using WT-heterotetrarmeric $SthK_{Cterm}$ protein, we applied TCSPC data to our lifetime FRET model for the first time and obtained distance distributions comparable to those previously obtained from the same protein construct using frequency domain lifetime measurements. To make a direct comparison of energetics between $SthK_{Cterm}$ and $SthK_{Full}$, a homotetrameric construct of $SthK_{Cterm}$ was created and the extent of intersubunit FRET in this system was measured. We were able to incorporate this additional FRET contribution in our lifetime model for cases, like homotetrameric $SthK_{Cterm}$ and $SthK_{Full}$, in which additional FRET acceptors were present. We obtained distance distributions of the CNBD C-helix in $SthK_{Full}$ in the presence and absence of cAMP and compared them to distributions from homotetrameric $SthK_{Cterm}$, finding that while the states appear to be similar in both constructs, the relative proportion of active state is higher in both the apo and saturating cAMP conditions for $SthK_{Full}$. Together, these findings highlight the power of time-resolved tmFRET in providing structural and energetic insights in the ligand-mediated conformational changes of SthK.

This work advances the technique of time resolved tmFRET is several ways. First, our analysis of heterotetrameric $SthK_{Cterm}$ revealed that TCSPC lifetime measurements were able to obtain distance distributions associated with the conformational changes of our protein. These distance distributions were consistent with both chiLife computational predictions and previous frequency domain FLIM measurements. The subtle differences between the TCSPC and frequency domain data may arise from technical considerations: 1) fitting a double-exponential

lifetime for the donor only values in the TCSPC data, 2) globally fit across two $[Ru(bpy)_2phenM]^{2+}$ and $[Fe(phenM)_3]^{2+}$ acceptors with different R_0s in the frequency domain, 3) the experimental setup between FLIM and cuvette-based TCSPC measurements, or 4) protein batch preparations. Nonetheless, the similarity in outcomes between the two different measurement methods reinforces the use of time resolved tmFRET techniques for studying protein conformations even across different experimental setups. While both lifetime methods appear equally justified in theory and practice, we favor the TCSPC measurement technique due to its well-defined error model, which offers more comparable statistical measurements and meaningful reduced χ^2 values. We believe this makes for better assessments of fit qualities (χ^2 values and residuals) and more direct comparisons between different models. Second, in homotetrameric $SthK_{Cterm}$, intersubunit FRET contributions were identified and modeled as fixed background distributions in the lifetime FRET analysis. Although the intersubunit FRET was relatively minor in the donor-acceptor pair site used here, this approach provides a general framework for addressing more complex systems with FRET changes occurring between multiple different acceptors. Incorporating intersubunit FRET enhanced the accuracy and interpretability of our tmFRET data in SthK and would be generally applicable to systems in which experimental FRET setups would not be able to avoid multiple FRET acceptors. Third, time-resolved tmFRET has been shown here to be sensitive to differences in protein energetics, even when using the same donor-acceptor pair across different protein constructs and recording conditions. Comparisons among heterotetramers, homotetramers and full-length constructs revealed close structural states with average distances differing by no more than 2Å. Despite these similarities in state distances, the energetic profiles between constructs varied significantly, which was consistent even when employing different fitting approaches (ie. individually fitting $SthK_{Full}$ or globally fitting $SthK_{Full}$ to $SthK_{Cterm}$). This sensitivity to energetic variations reinforces the utility of tmFRET to uncover complex energetic and conformational changes in proteins.

Despite the success of this approach, it is worth mentioning some experimental challenges with this work that can be improved moving forward. 1) As illustrated by our analysis of χ^2 surfaces from TCSPC data, correlations between certain parameters, such as the σ values of the Gaussian states and the fraction donor only, may complicate the identification of certain parameter values. While these correlations likely did not affect the direct comparison between

$SthK_{Cterm}$ and $SthK_{Full}$, we noticed deviations from expected trends in some constructs, such as the lack of consistently lower σs in ligand-bound states of the homotetrameric- $SthK_{Cterm}$. 2) The experimental conditions of our $SthK_{Full}$ protein measurements, conducted in detergent with a small presence of truncated subunits, may not fully replicate SthK's conformational changes in physiological conditions. Future studies should aim to make time-resolved tmFRET measurements of SthK in lipid nanodisks, liposomes, or more native systems to address these concerns. 3) The measured intersubunit FRET that we included into our model as a fixed background may not fully represent the actual additional FRET contribution. For example, the assumption of a Gaussian shaped distance distributions in this case, especially with the potential for up to 3 intersubunit acceptors and 12 different resting-active state combinations, is not well founded. The chiLife distributions, while only static predictions, are not Gaussian in shape (Figure 3D) and thus may not be well approximated with a Gaussian distribution. However, using the chiLife distributions in place of the experimentally derived distributions did not seem to change the analysis significantly (data not shown). 5) The energetic effect observed of the chosen donor and acceptor labeling sites, despite their seemingly peripheral location and solvent exposure, highlights the importance of understanding how labeling may affect protein energetics. Even with these limitations, we believe that we have advanced our time-resolved tmFRET approach and our understanding of ligand-mediated allostery in SthK.

Our results can be further interpreted in terms of the modular gating scheme in Figure 1B. Our findings suggest that the presence of the pore in $SthK_{Full}$ does effect the conformational changes in the CNBD. In comparing the ΔGs between $SthK_{Cterm}$ and $SthK_{Full}$, the presence of the pore domain enhances the favorability of conformational transitions in the CNBD by decreasing the relative ΔG in both the apo and cAMP state by roughly ~1 Kcal/mol (Figure 7). As a result, in reverse, the presence of the C-terminal domains must also decrease the favorability of the pore's transition from closed to open. This observation aligns with previous studies indicating that removing cytoplasmic domains of HCN channels increases favorability of pore opening (24, 25). Another implication of this result is that the C-linker likely remains in a 'broken' resting state in $SthK_{Cterm}$ without the pore, where it is either not able to, or very minimally able to, enter its active state.

Although several questions arise in putting these results in context of the modular gating scheme, one question emerges in particular from the high proportion (nearly 40%) of the active state of the CNBD in the absence of ligand. How does this result fit with electrophysiology experiments showing that the pore is almost never open without ligand? One explanation for this could be that the coupling between the CNBD domain and either the C-linker or pore is very inefficient, resulting in the very low open probabilities of the pore. Future work should investigate conformational transitions upon ligand binding in additional domains of $SthK_{Full}$, such as the C-linker and pore regions, to obtain these coupling values between domains. These measurements would complement our current understanding of CNBD energetics and provide a more complete picture of the modular gating scheme proposed in Figure 1. Overall, this work underscores the versatility of time-resolved tmFRET as a tool for studying structural and energetic changes in proteins, advancing our ability to dissect complex molecular mechanisms of allostery.

Materials and Methods

Protein expression and purification of $SthK_{Cterm}$. The creation, expression and purification of $SthK_{Cterm}$ protein constructs was carried out as previously described (15). The construct for $SthK_{Cterm}$:V416C was designed and expressed following the same methodology as the other $SthK_{Cterm}$ protein constructs. For all constructs, purified protein constructs underwent TEV cleavage and ion exchange cleanup to remove the attached MBP solubility tag. Protein was run on PD MidiTrap G-10 (Cytiva) to remove TCEP and immediately frozen with liquid nitrogen (LN) for storage at -80° C. For $SthK_{Cterm}$:S361Acd-V416C homotetramers, no additional WT-$SthK_{Cterm}$ was added although protein was prepared identically otherwise.

Constructs, expression and purification of $SthK_{Full}$. Constructs for the full-length channel $SthK_{Full}$ were designed by modifying the previously published construct of the cysteine free SthK (cfSthK) in the pCGFP vector (12). The GFP sequence fragment was removed from the C-terminal end of SthK by Gibson cloning and replaced with the sequences for a TEV protease cleavage sequence followed by a Twin-Strep-tag affinity tag sequence (the same as the $SthK_{Cterm}$ constructs). Using site-directed mutagenesis, an amber stop codon was introduced at position 361

and an acceptor site was engineered by mutating site 416 to cysteine to create two constructs: $SthK_{Full}$:S361Acd and $SthK_{Full}$:S361Acd-V416C.

These constructs were co-transformed with the AcdA9 aminoacyl tRNA synthetase/tRNA-containing plasmid (pDule2) (26) into B-95.ΔA *E. coli* (DE3) cells (27). Liter sized cultures of transformed *E. coli* were grown in terrific broth medium at 37° C in 100 μg/ml carbenicillin and 60 μg/ml spectinomycin to an OD_{600} ~0.4 before adding Acd (for a final concentration of 0.3 mM) and slowly lowering the temperature to 18° C (28, 29). For protein induction, 0.5 mM isopropyl β-D-1-thiogalactopyranoside (IPTG) was added and cultures were incubated at 18° C for 20 hours followed by harvesting by centrifugation. Cell pellets were resuspended in lysis buffer (150 mM KCl, 30 mM Tris, 2 mM β-mercaptoethanol, and 10% glycerol, pH 7.9 supplemented with mini EDTA-free protease inhibitor tablets [Pierce, ThermoFisher]) and lysed on an Avestin EmulsiFlex-C3 cell disruptor 5x times at 15,000-20,000 psi. Lysate was diluted and centrifuged at 30,000x g for 30 minutes at 4° C. Clarified lysate was then spun for 1.25 hours at 200,000x g at 4° C to isolate membranes. *E. coli* membranes were then resuspended 1:2 [wt/vol] in membrane resuspension buffer (150mM KCl, 30 mM Tris, 20% Glycerol, and 2 mM β-mercaptoethanol, pH 7.9 with an additional mini-protease inhibitor tablet) using a tissue homogenizer. Resuspended membranes were then solubilized with 1:1 [vol/vol] of solubilization buffer (150 mM KCl, 30 mM Tris, 80 mM DDM [Anatrace], 8 mM CHS [Anatrace], 2 mM β-mercaptoethanol, pH 7.9) for 1 hour and added to 1mL of Strep-Tactin Superflow high-capacity beads (iba Biosciences) at 4° C in a disposable column. The resin was washed with 25 mL of 2 mM β-mercaptoethanol supplemented KBT (150 mM KCl, 50 mM Tris, pH 7.9) with first 1 mM DDM, 0.1 mM CHS and then 10 mL of KBT with 4 mM LMNG, 0.4 mM CHS. Detergent was allowed to exchange on column for 30 mins at 4° C. An additional 10 mL of KBT was applied with 1 mM LMNG, 0.1 mM CHS with 1 mM tris(2-carboxyethyl)phosphine (TCEP) instead of β-mercaptoethanol. Protein was eluted from the Strep-Tactin resin with 10 mM d-Desthiobiotin (Sigma) in KBT buffer with 1 mM LMNG and 0.1 mM CHS and 1 mM TCEP.

Detergent solubilized protein was then run on a bolt 4-12% bis-tris polyacrylamide gel for in-gel fluorescence and run analytically on a Superose 6 5/150 size exclusion chromatography (SEC) column with 0.2 mM LMNG, 0.02 mM CHS to check for aggregates and protein stability. A PD-

10 MidiTrap G-10 (Cytiva) desalting column was used to remove TCEP and lower detergent to 0.2 mM LMNG, 0.02 mM CHS. Protein was immediately frozen with LN and stored at -80° C for later labeling and TCSPC experiments.

Labeling of $SthK_{Cterm}$ and $SthK_{Full}$ with metal acceptor tmFRET experiments. All constructs of $SthK_{Cterm}$ (both with cysteine and without) were labeled with 1mM $[Ru(bpy)_2phenM]^{2+}$ (in DMSO) before running on SEC to remove excess label and to isolate tetramers from monomers. Tetrameric $SthK_{Cterm}$ was then used directly in TCSPC experiments. The $SthK_{Full}$:S361Acd and $SthK_{Full}$:S361Acd-V416C constructs were labeled with 1 mM $[Ru(bpy)_2phenM]^{2+}$ for 30 minutes and then cleaned up as described previously using a BioSpin6 Mini column (BioRad) (15).

TCSPC Lifetime measurements. TCSPC lifetime data of Acd labeled protein samples (85 uL) were measured in 50 uL volume quartz cuvettes. Lifetime decays were obtained using a PicoQuant FluoTime Fluorescence Lifetime Spectrometer (PicoQuant, Berlin Germany) with a 375 nm UV laser excitation and single photon arrivals recorded on a hybrid photomultiplier detector assembly (PMA-40). Four cuvettes were consecutively recorded, the first two with Acd labeled protein, the third with buffer-only solution equivalent to the protein sample, and the fourth with diluted Ludox for measurement of the instrument response function (IRF). To each of the first three cuvettes, Adenosine 3',5'-cyclic monophosphate sodium salt monohydrate (cAMP, SigmaAldrich) in KBT buffer (150mM KCl, 30mM Tris, 10% glycerol, pH 7.9) was added at various concentrations following initial measurements without ligand. Buffer-only and IRF decays were applied to the lifetime model for each respective protein construct and ligand condition that was recorded. Decays were acquired with the EasyTau2 measurement software and exported for analysis in Igor (Wavemetrics) with our lifetime model.

Gaussian model of time-domain fluorescence lifetime data to obtain distance distributions. The time-domain fluorescence lifetime decays of the donor fluorophore in the presence of the acceptor were fit by model estimates for the time course of the decay, $Decay(t)$. These fits were calculated from the convolution of the measured instrument response function, $IRF(t)$ of the system with a model estimate of the fluorescence lifetime of the donor in the presence of the acceptor, $I_{DA}(t)$ and buffer-only fluorescence $I_B(t)$:

$$Decay(t) = \int_{-\infty}^{\infty}\left[IRF(t' - shift_{irf}) - bkgr_{irf}\right]\left[I_{DA}(t - t') + f_B\, I_B(t - t')\right]dt' + bkgr_{dec}$$

Equation 1

Where the variables are defined in Table I and important parameters displayed in Figure 8.

Table I

Variable	**Description**
t	Time of photon emission (in s)
r	Distance between the donor and acceptor (in Å)
$Decay(t)$	Time-dependent decay of the donor fluorescence (in counts)
$DecayB(t)$	Time-dependent decay of the buffer-only fluorescence (in counts)
$I_{DA}(t)$	Model estimate of the fluorescence lifetime of the donor in the presence of the acceptor (in counts)
$I_B(t)$	Model estimate of the fluorescence lifetime of a buffer-only sample (in counts)
$IRF(t)$	Measured instrument response function (in counts)
$bkgr_{dec}$	Time-independent decay background (in counts)
$bkgr_{irf}$	Time-independent background of the instrument response function (in counts)
$shift_{irf}$	Time shift between the instrument response function and the measured decay (in ps)
f_B	Scaling of the buffer fluorescence
A_0	Amplitude of the model estimate of the fluorescence lifetime of the donor (in counts)
f_D	Fraction of donor-only fluorescence in the sample
α_{Di}	Fraction of the ith component of the donor-only fluorescence (in counts)

τ_{Di}	Time constant of the ith component of the donor-only fluorescence (in s)
α_{Bi}	Amplitude of the ith component of the buffer fluorescence (in counts)
τ_{Bi}	Time constant of the ith component of the buffer fluorescence (in s)
R_0	Characteristic distance between donor and acceptor producing 50% FRET efficiency
$\rho(r)$	Probability distance distribution of the donor and acceptor distances
f_{Ai}	Fraction of the ith component of the probability distance distribution
$\bar{r}_i$	Average distance of the ith component of the donor-only fluorescence (in Å)
σ_i	Standard deviation of the ith component of the donor-only fluorescence (in Å)

The model for fluorescence lifetime assumes a donor-only fluorescence lifetime with one or two exponential components, and FRET between a donor and acceptor separated by one or two Gaussian-distributed distances, similar to that previously described for frequency domain measurements (1-5). This model predicts the following relationship for the fluorescence lifetime of the donor in the presence of acceptor, $I_{DA}(t)$:

$$I_{DA}(t) = A_0 \left[f_D \sum_{i=1}^{2} \alpha_{Di}\, e^{\left(-\frac{t}{\tau_{Di}}\right)} + (1 - f_D) \int_0^{\infty} \rho(r) \sum_{i=1}^{2} \alpha_{Di}\, e^{\left[-\frac{t}{\tau_{Di}} - \frac{t}{\tau_{Di}}\left(\frac{R_0}{r}\right)^6\right]} dr \right] \quad \text{Equation 2}$$

Where $\alpha_{D1} + \alpha_{D2} = 1$.

The density distribution of donor-acceptor distances, $\rho(r)$, was assumed to be the sum of up to two Gaussians:

$$\rho(r) = \sum_{i=1}^{2} f_{Ai} \frac{1}{\sigma_i \sqrt{2\pi}}\, e^{\left[-\frac{1}{2}\left(\frac{r-\bar{r}_i}{\sigma_i}\right)^2\right]} \quad \text{Equation 3}$$

where $f_{A1} + f_{A2} = 1$.

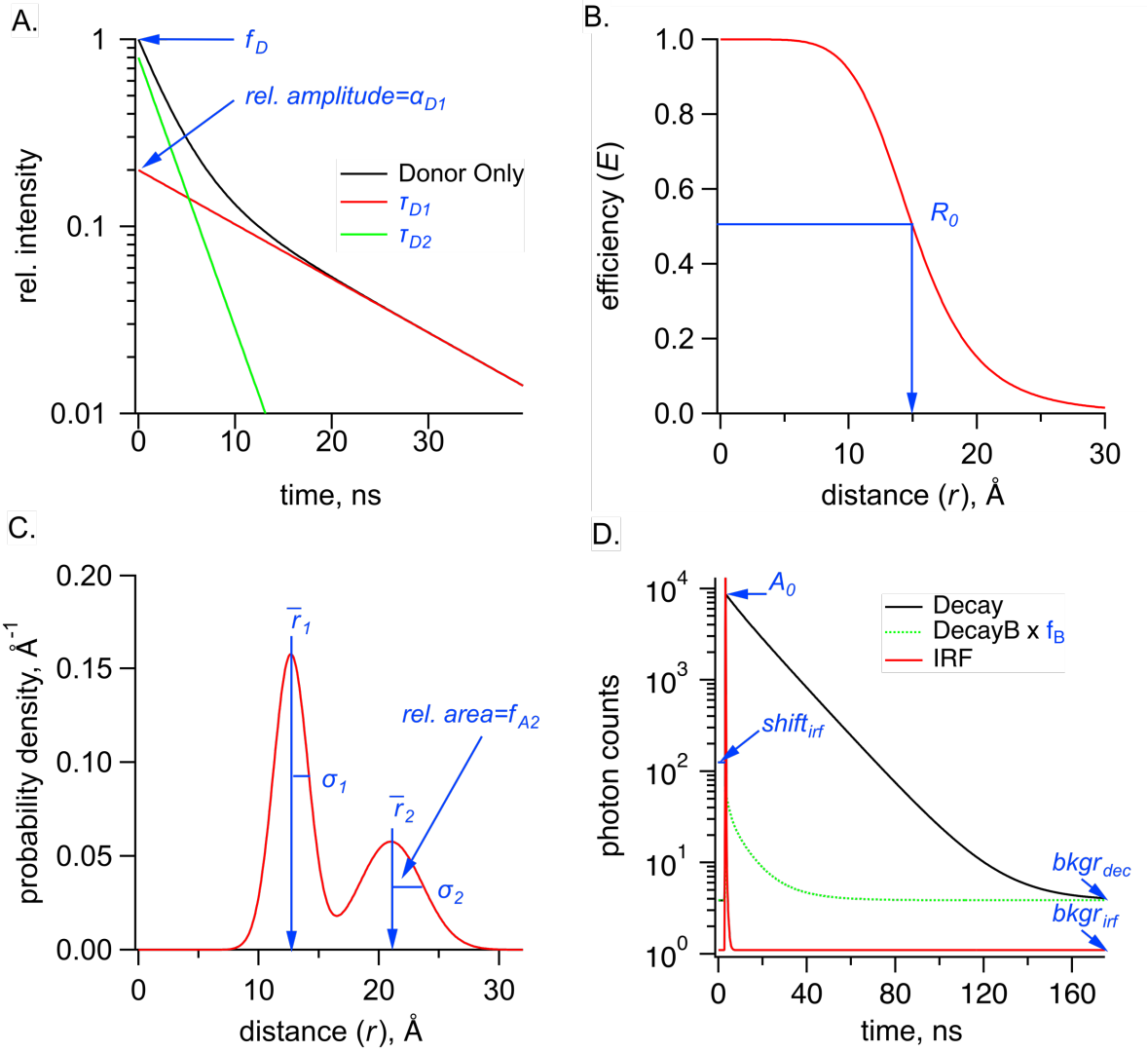

Figure 8. Parameters used in the lifetimes fitting model, shown in blue, for TCSPC data for the sum of two Gaussians distribution. **(A)** Graph of donor-only fluorescence-lifetime decay with two exponential components with time constants (τ_{D1}, τ_{D2}). The amplitude fraction of the donor-only lifetime in an experiment is determined as f_D. **(B)** FRET efficiency (E) plot as a function of distance (r) between donor and acceptor and the R_0 values for 50% FRET transfer. **(C)** Probability distribution plot of donor and acceptor distances P(r) showing the sum of two Gaussian distributions, each with their own average distance ($\bar{r}_1$ and $\bar{r}_2$), standard deviations (σ_1 and σ_2) and relative amplitude of the second component (A_2). **(D)** Example TCSPC data is shown with experimental measured photon count data (Decay), the instrument response function (IRF), and the buffer only decay (DecayB), with its corresponding scaling factor f_B relative to the Decay trace. Also indicated is a time-independent background of photon counts for the Decay trace, $bkgr_{dec}$, as well as two parameters associated with the IRF, its background, $bkgr_{irf}$, and the shift between instrument response function and measured decay, $shift_{irf}$. Parameter A_0 is the amplitude of the model estimate of the fluorescence lifetime of the donor (in photon counts).

The decay time course of the buffer-only sample, $DecayB(t)$, was fit with a convolution of the measured instrument response function, $IRF(t)$ with a multi-exponential model for the fluorescence lifetime, $I_B(t)$:

$$DecayB(t) = \int_{-\infty}^{\infty}\left[IRF(t' - shift_{irf}) - bkgr_{irf}\right][I_B(t - t')]dt' + bkgr_{dec} \qquad \text{Equation 4}$$

$$I_B(t) = \sum_{i=1}^{4} \alpha_{Bi}\, e^{\left(-\frac{t}{\tau_{Bi}}\right)} \qquad \text{Equation 5}$$

This model for the buffer-only fluorescence lifetime was then added to the model for the sample lifetime before convolving with the $IRF(t)$ (Equation 1).

This Gaussian model for fluorescence lifetimes and FRET was implemented in Igor Pro v8 (Wavemetrics, Lake Oswego, OR) (code available at https://github.com/zagotta/TDlifetime_program). The Gaussian model was either fit, with χ^2 minimization, to individual decay time courses, or globally fit to multiple decays with the sample under different conditions as indicated in the text. There are 15 parameters in the parameter vector ($f_D, \tau_{D1}, \alpha_{D1}, \tau_{D2},\ R_0, \bar{r}_1, \sigma_1, f_{A2}, \bar{r}_2, \sigma_2, shift_{irf}, f_B, A_0, bkgr_{dec}, bkgr_{irf}$). R_0 was fixed to a value previously determined from emission spectra of the donor and absorbance spectra of the acceptor using the Förster equation assuming $\kappa^2 = 2/3$. f_{A2}, was generally fixed to 0 or 1 for fits assuming a single Gaussian distance distribution but was allowed to vary when multiple distance components were expected (e.g. when two Gaussians were fit). f_B was fixed to the acquisition time for the experimental sample divided by the acquisition time for the buffer-only sample. And $bkgr_{irf}$was always fixed to 0 as the average background photon count in the $IRF(t)$ was <<1.

For the individual decay fits to the donor-only sample, f_D was set to 1, and only $\tau_{D1}, \alpha_{D1}, \tau_{D2}, shift_{irf}, A_0, bkgr_{dec}$ were allowed to vary. For the individual decay fits to the donor+acceptor samples, $\tau_{D1}, \alpha_{D1}, \tau_{D2}$were constrained to the previously determined values from the donor-only sample, and $f_D, \bar{r}_1, \sigma_1, f_{A2}, \bar{r}_2, \sigma_2, shift_{irf}, A_0, bkgr_{dec}$ were varied. For global fits to multiple decays with the sample under different conditions, multiple parameters were constrained to be the same across some or all of the decay fits, as indicated in the text.

To assess the resolvability of our parameters in our TCSPC model, we generated χ^2 plots from a representative dataset of $SthK_{Cterm}$:S361Acd-V416C for the key parameters (Figure 8 - figure supplement 1). Similar to previous results, parameters we tested reliably converged on a minimized reduced χ^2 value (~1), although the σ parameters produced plots with much shallower slopes and were noticeably less well determined than the other parameters (15). Additionally, for the parameters expected to have highest correlation, as identified by a covariance matrix from our fits, we calculated reduced χ^2 surfaces (Figure 8- figure supplement 2). A small correlation was observed between σ_1 and the fraction donor only, f_D, and between the average distance $\overline{r_1}$ and f_D. As a result, we limit our interpretation of σ values. Overall, the close agreement of $\overline{r}$, σ, and fraction A_2 values obtained with TCSPC and frequency domain indicates that time-resolved tmFRET is robust across different methods of lifetime measurements. The time-domain lifetime model was used to obtain distance distributions moving forward and was adapted to make structural and energetic measurements in the full-length SthK channel.

Adaptation of the Gaussian time-domain lifetime model to include intersubunit FRET. The general form of the lifetime equation for Equation 2, in which there is one single donor acceptor pair, is as follows:

$$I_{DA}(t) = \int_0^\infty \rho(r) \sum_{i=1}^{2} \alpha_{Di}\, e^{-\left[\frac{t}{\tau_{Di}} + \frac{t}{\tau_{Di}}\left(\frac{R_0}{r}\right)^6\right]} dr \qquad \text{Equation 6}$$

Adding a second acceptor FRET site with a new distance r_2 can be generalized as:

$$I_{DA}(t) = \int_0^\infty \int_0^\infty \rho_1(r_1)\rho_2(r_2) \sum_{i=1}^{2} \alpha_{Di}\, e^{-\left[\frac{t}{\tau_{Di}} + \frac{t}{\tau_{Di}}\left(\frac{R_0}{r_1}\right)^6 + \frac{t}{\tau_{Di}}\left(\frac{R_0}{r_2}\right)^6\right]} dr_1\, dr_2 \qquad \text{Equation 7}$$

Where $\rho_1(r_1)$ is the distance distribution of the first acceptor and $\rho_2(r_2)$ is the distance distribution of the second, intersubunit FRET acceptor. This equation can be rewritten as the product of integrals of the following form:

$$I_{DA}(t) = \sum_{i=1}^{2} \int_0^\infty \alpha_{Di}\, \rho_1(r_1)\, e^{-\left[\frac{t}{\tau_{Di}} + \frac{t}{\tau_{Di}}\left(\frac{R_0}{r_1}\right)^6\right]}\, dr_1 \int_0^\infty \rho_2(r_2)\; e^{-\left[\frac{t}{\tau_{Di}}\left(\frac{R_0}{r_2}\right)^6\right]}, \qquad \text{Equation 8}$$

where each $\rho(r)$ are parameterized as a sum of two Gaussian distributions.

The experimentally measured intersubunit FRET was first fit with the lifetime model from Equation 6 (Equation 2). The assumption of a Gaussian shaped distance distributions in this case, especially with the potential for up to 3 acceptors and 2^4 different resting-active state combinations, is not well founded. As a result, the ratio between the Gaussians was not allowed to vary in our fit of the experimental data and was fixed at a best-fit ratio between the resting and active Gaussians of 0.2 and 0.8 for the apo and cAMP conditions respectively. The obtained $\bar{r}_1, \sigma_1, \bar{r}_2, \sigma_2$ values from this fit were then used as fixed values for the distribution $\rho_2(r_2)$ in Equation 8 when fitting homotetrameric $SthK_{Cterm}$ and $SthK_{Full}$ lifetime data. While the $\rho_2(r_2)$ $\bar{r}s$ and σs of the intersubunit distance distribution were held constant, the fraction between these states (A_2) was allowed to vary with the same fraction A_2 value from $\rho_1(r_1)$ along with $\bar{r}_1, \sigma_1, \bar{r}_2, \sigma_2$ from $\rho_1(r_1)$.

Free Energy and Dose Response Calculations.

$$\Delta G = -RT * \ln\left(\frac{A_2}{1-A_2}\right) \quad \text{Equation 9}$$

$$\Delta\Delta G_{cAMP} = \Delta G_{cAMP} - \Delta G_{apo} \quad \text{Equation 10}$$

where R is the molar gas constant, T is the absolute temperature (K), and A_2 and 1 - A_2 are the proportion of molecules in the active state and resting respectively.

Quadratic fits (Figure 2F and Figure 6F) were obtained using:

$$Fractional\ Response = A \times \frac{([R]_{total} + [P]_{total} + K_D) - \sqrt{([R]_{total} + [P]_{total} + K_D)^2 - 4 \times [P]_{total} \times [R]_{total}}}{2 \times [P]_{total}} + B$$

Equation 11

Where K_D is the dissociation constant for cAMP, $[R]_{total}$ is the total cAMP concentration, $[P]_{total}$ is the total protein concentration, A is a scaled amplitude parameter and B is a y-axis offset term. Above parameters were obtained from fits, and protein concentration $[P]_{total}$ was corroborated via absorbance at 280nm and bradford assay for each sample, which were in good agreement.

Statistics and reproducibility. Data values were expressed as mean ± SD of n independent experiments, unless stated otherwise, and all error bars are ± SD.

References

1. K. B. Craven, W. N. Zagotta, CNG and HCN channels: Two peas, one pod. *Annu Rev Physiol* **68**, 375–401 (2006).
2. C. He, F. Chen, B. Li, Z. Hu, Neurophysiology of HCN channels: From cellular functions to multiple regulations. *Prog Neurobiol* **112**, 1–23 (2014).
3. K. Matulef, W. N. Zagotta, Cyclic Nucleotide-Gated Ion Channels. *Annu Rev Cell Dev Biol* **19**, 23–44 (2003).
4. E. G. B. Evans, J. L. W. Morgan, F. DiMaio, W. N. Zagotta, S. Stoll, Allosteric conformational change of a cyclic nucleotide-gated ion channel revealed by DEER spectroscopy. *Proc Natl Acad Sci U S A* **117**, 10839–10847 (2020).
5. Z. M. James, W. N. Zagotta, Structural insights into the mechanisms of CNBD channel function. *Journal of General Physiology* **150**, 225–244 (2018).
6. K. B. Craven, N. B. Olivier, W. N. Zagotta, C-terminal movement during gating in cyclic nucleotide-modulated channels. *J Biol Chem* **283**, 14728–14738 (2008).
7. M. Brams, J. Kusch, R. Spurny, K. Benndorf, C. Ulens, Family of prokaryote cyclic nucleotide-modulated ion channels. *Proc Natl Acad Sci U S A* **111**, 7855–7860 (2014).
8. P. A. M. Schmidpeter, C. M. Nimigean, *Correlating ion channel structure and function*, 1st Ed. (Elsevier Inc., 2021).
9. J. Rheinberger, X. Gao, P. A. M. Schmidpeter, C. M. Nimigean, Ligand discrimination and gating in cyclic nucleotide-gated ion channels from apo and partial agonist-bound cryo-EM structures. *Elife* **7**, 1–25 (2018).
10. P. A. M. Schmidpeter, X. Gao, V. Uphadyay, J. Rheinberger, C. M. Nimigean, Ligand binding and activation properties of the purified bacterial cyclic nucleotide-gated channel SthK. *Journal of General Physiology* **150**, 821–834 (2018).
11. A. Marchesi, *et al.*, An iris diaphragm mechanism to gate a cyclic nucleotide-gated ion channel. *Nat Commun* **9** (2018).
12. J. L. W. Morgan, E. G. B. Evans, W. N. Zagotta, Functional characterization and optimization of a bacterial cyclic nucleotide-gated channel. *Journal of Biological Chemistry* **294**, 7503–7515 (2019).
13. D. Kesters, *et al.*, Structure of the SthK carboxy-terminal region reveals a gating mechanism for cyclic nucleotide-modulated ion channels. *PLoS One* **10**, 1–12 (2015).
14. X. Gao, *et al.*, Gating intermediates reveal inhibitory role of the voltage sensor in a cyclic nucleotide-modulated ion channel. *Nat Commun* **13** (2022).
15. P. Eggan, S. E. Gordon, W. N. Zagotta, Ligand-Coupled Conformational Changes in a Cyclic Nucleotide-Gated Ion Channel Revealed by Time-Resolved Transition Metal Ion FRET. *Elife* 2024.04.25.591185 (2024). https://doi.org/10.1101/2024.04.25.591185.
16. F. T. Horrigan, R. W. Aldrich, Coupling between voltage sensor activation, Ca2+ binding and channel opening in large conductance (BK) potassium channels. *J Gen Physiol* **120**, 267–305 (2002).
17. H. N. Motlagh, J. O. Wrabl, J. Li, V. J. Hilser, The ensemble nature of allostery. *Nature* **508**, 331–339 (2014).
18. V. J. Hilser, J. O. Wrabl, H. N. Motlagh, Structural and energetic basis of allostery. *Annu Rev Biophys* **41**, 585–609 (2012).

19. E. Haas, M. Wilchek, E. Katchalski-Katzir, I. Z. Steinberg, Distribution of end-to-end distances of oligopeptides in solution as estimated by energy transfer. *Proc Natl Acad Sci U S A* **72**, 1807–1811 (1975).
20. W. N. Zagotta, *et al.*, Measuring conformational equilibria in allosteric proteins with time-resolved tmFRET. *Biophys J* 2023.10.09.561594 (2024). https://doi.org/10.1016/j.bpj.2024.01.033.
21. W. N. Zagotta, *et al.*, An improved fluorescent noncanonical amino acid for measuring conformational distributions using time-resolved transition metal ion FRET. *Elife* **10**, 2021.05.10.443484 (2021).
22. J. R. Lakowicz, *Principles of fluorescence spectroscopy* (2006).
23. S. E. Gordon, *et al.*, Long-distance tmFRET using bipyridyl- and phenanthroline-based ligands. *Biophys J* 2023.10.09.561591 (2024). https://doi.org/10.1016/j.bpj.2024.01.034.
24. K. E. A. Magee, Z. Madden, E. C. Young, HCN Channel C-Terminal Region Speeds Activation Rates Independently of Autoinhibition. *J Membr Biol* **248**, 1043–1060 (2015).
25. B. J. Wainger, M. DeGennaro, B. Santoro, S. A. Siegelbaum, G. R. Tibbs, Molecular mechanism of cAMP modulation of HCN pacemaker channels. *Nature* **411**, 805–810 (2001).
26. I. Sungwienwong, *et al.*, Improving target amino acid selectivity in a permissive aminoacyl tRNA synthetase through counter-selection. *Org Biomol Chem* **15**, 3603–3610 (2017).
27. T. Mukai, *et al.*, Highly reproductive Escherichia coli cells with no specific assignment to the UAG codon. *Sci Rep* **5**, 1–9 (2015).
28. L. C. Speight, *et al.*, Efficient synthesis and in vivo incorporation of acridon-2-ylalanine, a fluorescent amino acid for lifetime and Förster resonance energy transfer/luminescence resonance energy transfer studies. *J Am Chem Soc* **135**, 18806–18814 (2013).
29. C. M. Jones, Y. Venkatesh, E. J. Petersson, *Protein labeling for FRET with methoxycoumarin and acridonylalanine*, 1st Ed. (Elsevier Inc., 2020).

Supplemental Figures

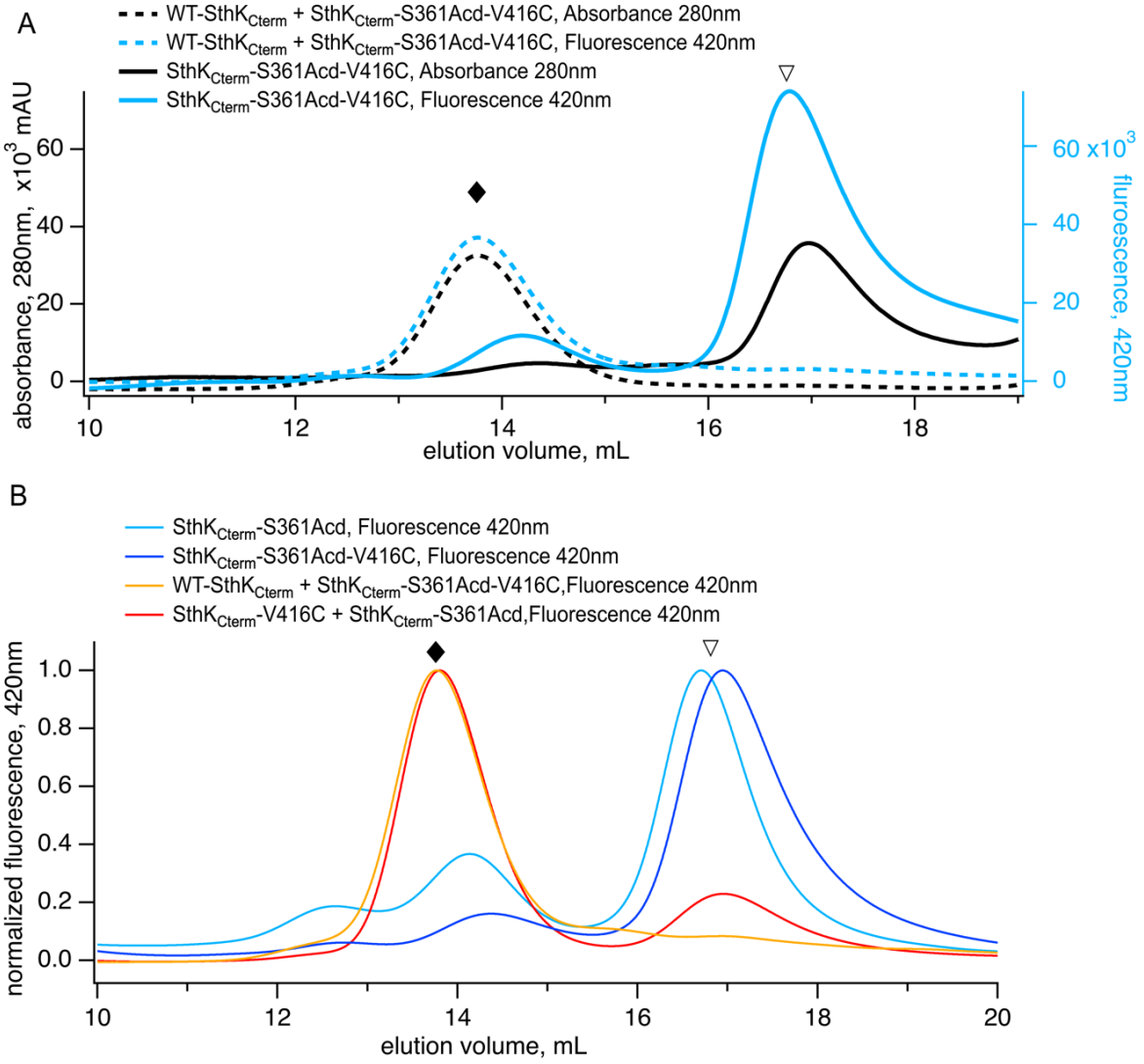

Figure 4 – supplemental figure 1. Different tetramerization abilities for SthK$_{Cterm}$ constructs. **(A)** Size exclusion chromatography (SEC) Superose6 Increase 10/300 column for WT-heterotetrameric-SthK$_{Cterm}$-S361Acd-V416C (dashed lines) and homotetrameric SthK$_{Cterm}$-S361Acd-V416C (solid lines) in 280nm absorbance (black) and Acd 425nm fluorescence (blue). Tetramer peak indicated (solid diamong) along with monomers (open triangles). **(B)** SEC of homotetrameric constructs, SthK$_{Cterm}$-S361Acd (light blue) and SthK$_{Cterm}$-S361Acd-V416C (dark blue) vs heterotetrameric constructs WT-SthK$_{Cterm}$+ SthK$_{Cterm}$-S361Acd-V416C (orange) and SthK$_{Cterm}$-V416C + SthK$_{Cterm}$-S361Acd-V416C (red).

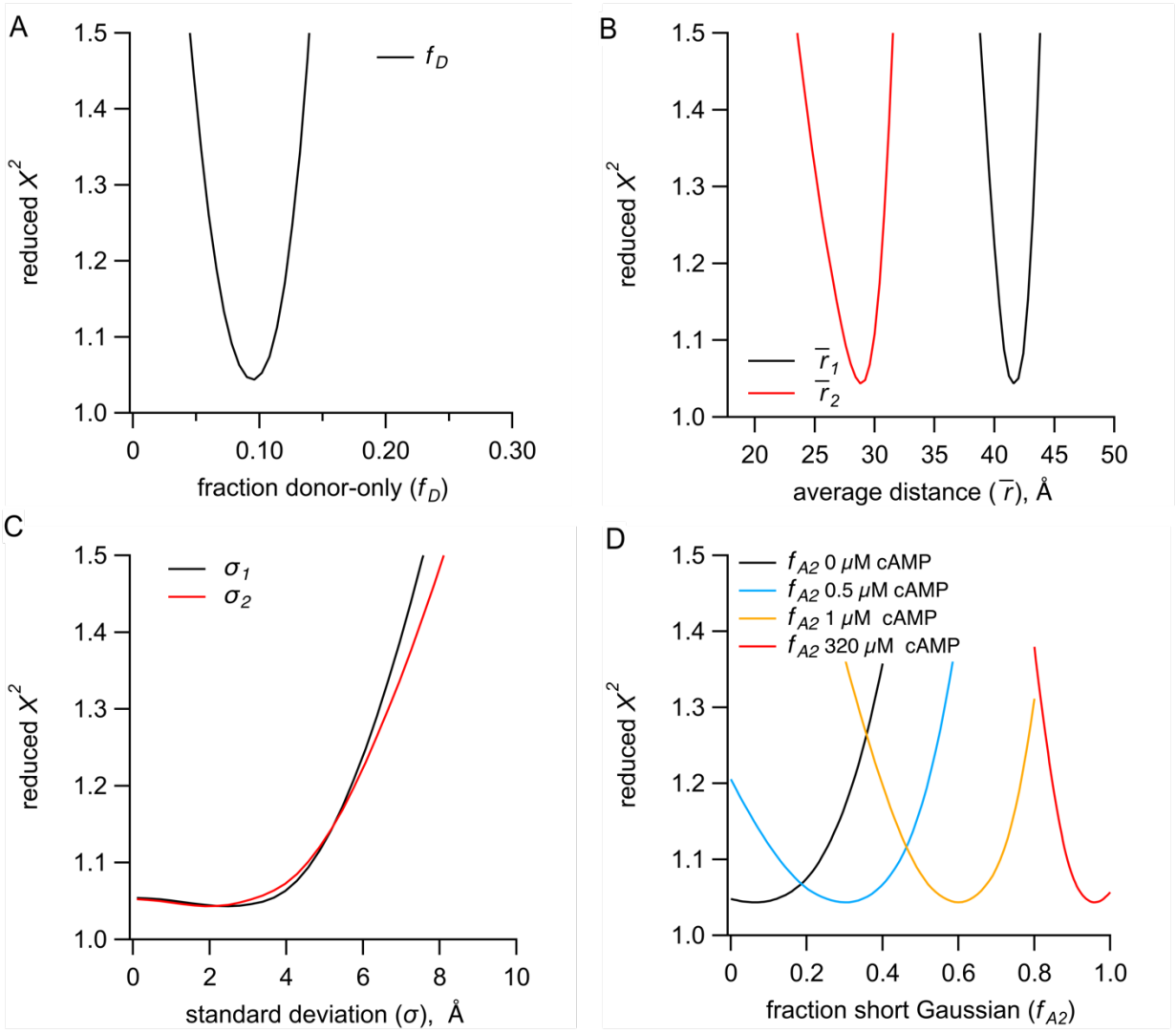

Figure 8 – figure supplement 1. Identifiability of parameters in the sum of two Gaussian distributions model from TCSPC data, from representative dataset. **(A)** Minimization of reduced χ^2 values for the fraction of donor-only component (f_D) in protein samples. **(B-C)** Minimization of χ^2 values for the Gaussian average distance ($\bar{r}$) (B) and standard deviation (σ) (C) for the resting (black) and active states (red). **(D)** Minimization of χ^2 values for parameter A_2 for the conditions of apo, 0.5 μM, 1 μM and 320 μM cAMP.

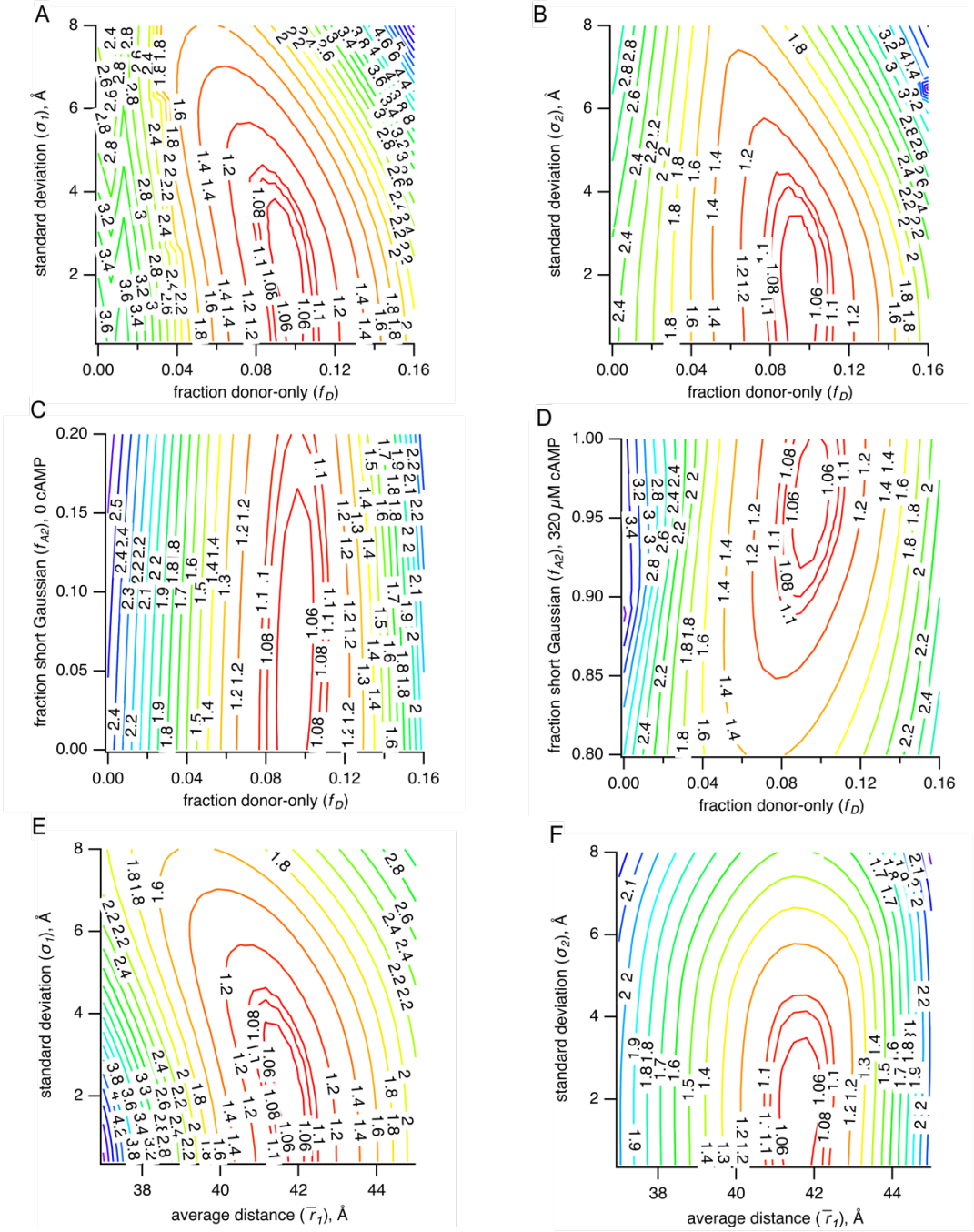

Figure 8 – figure supplement 2. (A-F) Parameter correlation from representative dataset of χ^2 values in 3 dimensions. Parameter correlations are for σ_1 against f_D (A), for σ_2 against f_D (B), for f_{A2} in 0 μM cAMP against f_D (C), for f_{A2} in 320 μM cAMP against f_D (D), for σ_1 against $\bar{r}_1$ (E) and for σ_2 against $\bar{r}_1$(F).

Chapter 5: Conclusions

Conclusions for Ligand-Gating in the CNBD of SthK:

In this work, the technique of time-resolved tmFRET was utilized to better understand the conformational changes and the energetics that describe ligand binding in the prokaryotic CNBD channel SthK. We adopted a modular gating framework, considering the allosteric transition within specific domains as simple transitions between resting and active states. For a complete characterization of the allosteric mechanism across the protein structure, measurements of conformational dynamics are needed at all domain/module levels of the modular gating scheme. For ligand gating in SthK, we chose to start with making time-resolved tmFRET measurements of the conformational change where ligand first binds, at the C-helix movement of the CNBD.

Initially, even before moving to the SthK protein, the time-resolved tmFRET technique was validated in Chapter 2 using the simple model protein MBP, demonstrating its ability to detect structural heterogeneity within and between conformational states. Distance distributions derived from frequency-domain lifetimes in MBP correlated well with both computational predictions and DEER measurements, confirming that the method was reliable. Additionally, it provided the basis for using the metal ion acceptors $[Fe(phenM)_3]^{2+}$ and $[Ru(bpy)_2phenM]^{2+}$ with the Acd donor, for studying longer-range conformational transitions.

Building upon these successes, we applied the time-resolved tmFRET technique to SthK in Chapter 3, to address questions about ligand gating in the allosteric process of channel opening. To simplify the protein system further and isolate changes in the CNBD, where ligand binds first, we focused on a C-terminal fragment of SthK, $SthK_{Cterm}$. We showed that using an unnatural amino acid fluorophore Acd and metal ion acceptors across several different sites we were able to measure the movement of the CNBD C-helix relative to the β-roll. Steady-state FRET experiments revealed differences between monomeric and tetrameric $SthK_{Cterm}$, with monomers favoring the active state in the absence of ligand. Using fluorescence lifetimes in the frequency domain, we obtained distance distributions for tetrameric $SthK_{Cterm}$ in apo, cAMP-, and cGMP- bound conditions. Global fitting across both $[Fe(phenM)_3]^{2+}$ and $[Ru(bpy)_2phenM]^{2+}$ acceptor experiments improved parameter resolution, allowing us to calculate Gibbs free energy changes (ΔG) between states. These results showed that the ligand-free transitions between resting and active states were unfavorable, strongly favored with cAMP, and minimally favored

with cGMP, consistent with ligands' roles as full and partial agonists, respectively. This measured free energy change is the maximum energetic contribution that might be imparted to induce channel opening.

It remained unclear how the distance distributions and energetics observed in $SthK_{Cterm}$ would translate to the full-length channel ($SthK_{Full}$) and thus we turned to measuring the same conformational change in $SthK_{Full}$ in Chapter 4. Recognizing the potential issue of intersubunit FRET in the tetrameric $SthK_{Full}$ where all subunits are labeled with donor and acceptor pairs, we quantified the extent of this intersubunit FRET and refined our lifetime distance distribution model to account for it. Using the same donor-acceptor pair, we obtained distance distributions for both homotetrameric $SthK_{Cterm}$ and detergent purified $SthK_{Full}$. Comparisons of their energetics revealed that while their structural states remained largely the same, the presence of the pore domain enhanced the favorability of the CNBD C-helix transition from resting to active states. This highlights the effect of interdomain coupling on the conformational dynamics within the CNBD domain, as the modular gating scheme suggests.

Based on our findings, we propose a hypothesis for the allosteric mechanism in SthK that combines some of our findings and may also apply to other CNBD channels. In the absence of ligand, monomeric $SthK_{Cterm}$ strongly favors the active conformational state, whereas tetramerization significantly reduces the favorability of this transition. This suggests that C-linker tetramerization opposes the conformational transition of the CNBD and effectively keeps the CNBD mostly in the resting state in $SthK_{Cterm}$. Additionally, distance distribution data from $SthK_{Full}$ indicate that the presence of the pore domain enhances the favorability of the CNBD's transition to the active state, removing some of the C-linkers inhibition on the CNBD. This implies that the pore counteracts the inhibitory effect of the C-linker on the CNBD transition in agreement with previous results from HCN channels (1, 2). Therefore, in this hypothetical model, the C-linker functions as an inhibitory module, acting as a switch between the conformational transition of the CNBD and the structural changes required for opening of the pore. Lastly, the relatively high activation of the CNBD in the absence of ligand compared to the nearly permanently closed pore domain recorded with electrophysiology implies that there is likely very inefficient coupling between the CNBD domain and pore.

Future research may explore this model further, especially by making tmFRET distance distribution measurements in other domains of SthK upon ligand binding. Ideally, distance distributions measured in two different domains of $SthK_{Full}$ across multiple different agonists would give the most comparable coupling values to the arrows between modules depicted in the modular gating scheme. Additionally, given recent research highlighting the role of lipids in channel gating, it would be valuable to investigate how tmFRET derived distance distributions may appear in more native conditions, such as lipid nanodisks or liposomes.

Conclusions for Time-Resolved tmFRET Technique:

In addition to increasing our understanding of the allosteric mechanism of ligand binding in SthK, we have also greatly advanced the use of time-resolved tmFRET as a tool for measuring conformational dynamics and energetics. We first applied our tmFRET experimental technique to fluorescence lifetimes measured in the frequency domain and then adapted our lifetime model to analyze time domain TCSPC lifetime data. By comparing lifetime results obtained with both our frequency-domain and our time-domain approaches in the same construct of $SthK_{Cterm}$, we were able to identify some pros and cons across these techniques. For example, our frequency domain lifetime microscope approach, which utilized just an 11ul droplet of sample on a coverslip, required high concentrations of protein due to its short path-length compared to a standard cuvette setup in the TCSPC instrument. Additionally, TCSPC data has a more clearly defined Poisson noise model of single photon arrivals, which allowed for more meaningful comparisons of reduced χ^2 values across model fits (3, 4). The more clearly defined statistics also allows for the use of more sophisticated statistical analysis methods in the future, like Bayesian probabilistic methods. In contrast, our frequency domain lifetime microscope measurements allowed for spatial analysis of lifetimes throughout a protein sample, which was useful in indicating if protein became aggregated in solution or had non-homogenous properties. It also provided a model-free method of analyzing lifetimes through phasor plots, which visually justified our use of a sum of two Gaussian states in subsaturating cAMP concentrations and partial agonist cGMP conditions. While some small differences were observed across fluorescence lifetime methods, in SthK the average distances of resting and active states as well as the significant energetic change associated with saturating cAMP remained consistent, providing confidence in both approaches. Furthermore, in both MBP and in SthK, the obtained

distance distributions from both methods were remarkably close to computationally predicted distance distributions provided by chiLife and published structures.

By generating reduced χ^2 plots of individual parameters and χ^2 surface plots between parameters of the models from each lifetime method, we have begun to identify the most and least resolvable elements of each model. While most parameters were consistently resolvable and uncorrelated, we note that the fraction donor only (f_D) and σ parameters in particular are not always well resolved. This seems especially true when labeling efficiency is low, resulting in a large f_D, and in experimental conditions where the amount of FRET is low. We found that methods for independently identifying f_D, as well as globally fitting different lifetime data sets together, such as with different R_0s or across ligand conditions, helped improve resolvability of parameters in our model. Lastly, we expanded our lifetime model to accommodate cases with more than one acceptor for each donor, which we applied to account for intersubunit FRET in homotetrameric $SthK_{Cterm}$ and $SthK_{Full}$. This extended model is useful for incorporating additional FRET sources and can serve as a foundation for three-color FRET experiments.

Ultimately, obtaining distributions of distances from FRET lifetime data is complex and depends on the FRET model as well as the statistical methods used to fit the model to the lifetime data (3–5). We chose to parameterize our distance distributions as a sum of just two Gaussians. Two states were justified in context of our known protein conformational change being in either a resting or active conformational state, however we cannot fully discount the possibility of a third or more conformational states in our data. As our computational derived distance distributions through chiLife were mostly Gaussian in nature, this further supported our assumption to use Gaussian distributions, although parabolic and Lorentzian distributions have also been applied to distance distributions with similar success (6–10). We employed a non-linear least squares (NLLS) method to globally fit our FRET model to our data, which is probably the most common and easily implemented approach for lifetime analyses (3). However, there are several other methods that have been utilized to analyze FRET data from fluorescence lifetimes including method of moments, Maximum Entropy Method (MEM), Tikhonov Regularization and Bayesian inference (3–5). MEM and Tikhonov Regularization methods have been successfully used to obtain model-independent lifetime distributions, but their implementation is complex, require much longer analysis run-times, and the resulting

interpretation of the lifetime distributions is more complicated (5, 11–15). Unfortunately, these methods have been mostly used to obtain distributions of lifetimes rather than distance distributions between donor and acceptor and only two literature examples have been found with full distance distributions utilizing these methods (11, 15). These techniques are dependent on both the noise level of the sample and the regularization method selected empirically, which may require additional validation with model-dependent methods for confirmation of low-population conformational states. As a results, we believe that the Gaussian-parameterized NLLS fit method allows for easily adoptable, robust, and versatile analysis of conformational states in well-defined energetic models, such as the modular gating scheme, while acquiring insights into protein heterogeneity both within and between conformational states.

Our time-resolved tmFRET approach can nonetheless be improved in a number of ways moving forward. In terms of the lifetime FRET model for determining distance distributions, different distribution shapes or numbers of distributions (such as one to three Gaussians) may be better fit for some protein situations, and it is worth exploring how different distributions may compare quantitatively in different protein contexts. Furthermore, giving defined confidence ranges for parameters derived from χ^2 plots would help in provide uncertainty ranges on the conformational states and energetics that were determined (3, 11). Ultimately, employing Bayesian analysis could better determine which parameters have the most confidence, the range of uncertainty of various parameters, and is the method most suitable for comparing models in which different numbers of distributions or distribution shapes are used (3–5). We saw some success in improving parameter resolvability when we globally fit datasets from multiple different acceptors with different R_0s. This has theoretical foundation and should be explored further, especially by expanding the available acceptor metal ions that can be paired with Acd to give a range of R_0 values (16). It is also worth exploring how other donor and acceptor labeling techniques such as dual encoding of both donor fluorophore and acceptor metal-binding compounds into the protein structure as unnatural amino acids may work for tmFRET (17, 18). Even with the great potential for developing this methodology further, we strongly believe that the current approaches to time-resolved tmFRET described here can untangle the complexities of allosteric mechanisms across many protein systems and has been valuable so far in unraveling the ligand-mediated allosteric mechanism of CNBD ion channels.

References

1. B. J. Wainger, M. DeGennaro, B. Santoro, S. A. Siegelbaum, G. R. Tibbs, Molecular mechanism of cAMP modulation of HCN pacemaker channels. *Nature* **411**, 805–810 (2001).
2. G. Pulser, *et al.*, 2001 Nature 411 805 HCN truncation. **411**, 805–810 (2001).
3. J. R. Lakowicz, *Principles of fluorescence spectroscopy* (2006).
4. D. V O'Connor, W. R. Ware, J. C. Andre, Deconvolution of fluorescence decay curves. A critical comparison of techniques. *J Phys Chem* **83**, 1333–1343 (1979).
5. F. de Jong, C. Martín, J. Hofkens, M. Van der Auweraer, Data Analysis Methods in Time-Resolved Fluorescence Spectroscopy: A Tutorial Review. *Chemistry - A European Journal* **202401799** (2025).
6. D. Amir, S. Krausz, E. Haas, Detection of local structures in reduced unfolded bovine pancreatic trypsin inhibitor. *Proteins: Structure, Function, and Bioinformatics* **13**, 162–173 (1992).
7. D. Amir, E. Haas, Determination of intramolecular distance distributions in a globular protein by nonradiative excitation energy transfer measurements. *Biopolymers: Original Research on Biomolecules* **25**, 235–240 (1986).
8. P. Wu, L. Brand, Conformational flexibility in a staphylococcal nuclease mutant K45C from time-resolved resonance energy transfer measurements. *Biochemistry* **33**, 10457–10462 (1994).
9. A. Grinvald, E. Haas, I. Z. Steinberg, Evaluation of the Distribution of Distances Between Energy Donors and Acceptors by Fluorescence Decay. *Proceedings of the National Academy of Sciences* **69**, 2273–2277 (1972).
10. E. Haas, M. Wilchek, E. Katchalski-Katzir, I. Z. Steinberg, Distribution of end-to-end distances of oligopeptides in solution as estimated by energy transfer. *Proc Natl Acad Sci U S A* **72**, 1807–1811 (1975).
11. T. Vöpel, *et al.*, Triphosphate induced dimerization of human guanylate binding protein 1 involves association of the C-terminal helices: A joint double electron-electron resonance and FRET Study. *Biochemistry* **53**, 4590–4600 (2014).
12. V. A. Lórenz-Fonfría, H. Kandori, Transformation of time-resolved spectra to lifetime-resolved spectra by maximum entropy inversion of the laplace transform. *Appl Spectrosc* **60**, 407–417 (2006).
13. J. C. Brochon, Maximum entropy method of data analysis in time-resolved spectroscopy. *Methods Enzymol* **240**, 262–311 (1994).
14. A. K. Livesey, J. C. Brochon, Analyzing the Distribution of Decay Constants in Pulse-Fluorimetry Using the Maximum Entropy Method. *Biophys J* **52**, 693–706 (1987).
15. R. E. Dalbey, J. Weiel, W. J. Perkins, R. G. Yount, Resolution of multiple fluorescence lifetimes in heterogeneous systems by phase-modulation fluorometry. *J Biochem Biophys Methods* **9**, 251–266 (1984).
16. C. R. Cantor, P. Pechukas, Determination of Distance Distribution Functions by Singlet-Singlet Energy Transfer. *Proceedings of the National Academy of Sciences* **68**, 2099–2101 (1971).
17. K. Wang, *et al.*, Optimized orthogonal translation of unnatural amino acids enables spontaneous protein double-labelling and FRET. *Nat Chem* **6**, 393–403 (2014).

18. R. M. Bednar, P. A. Karplus, R. A. Mehl, Site-specific dual encoding and labeling of proteins via genetic code expansion. *Cell Chem Biol* **30**, 343–361 (2023).